DETECTING AND MODELING SUBSURFACE FRACTURE SYSTEMS IN GEOTHERMAL FIELDS USING SHEAR-WAVE SPLITTING

Chuanhai Tang

A dissertation submitted to the faculty of the University of North Carolina at Chapel Hill in partial fulfillment of the requirements for the degree of Doctor of Philosophy in the Department of Geological Sciences (Geophysics).

Chapel Hill
2009

Approved by:

Dr. Jose A. Rial

Dr. Jonathan M. Lees

Dr. Kevin G. Stewart

Dr. Lara S. Wagner

ABSTRACT

CHUANHAI TANG: Detecting and Modeling Subsurface Fracture Systems in Geothermal Fields Using Shear-wave Splitting
(Under the direction of Jose A. Rial)

Shear wave splitting (SWS) is emerging as a useful exploration tool for geothermal fields as it can detect the geometry of the fracture system and the intensity of cracking within the geothermal reservoir. The method is based on the analyses of polarizations (φ) and time delays (δt) of split shear-waves that have been distorted by the anisotropy of the medium through which the seismic waves have propagated. Two experiments were conducted in Krafla and Hengill geothermal fields in Iceland in the summers of 2004 and 2005 respectively. Clear evidences of SWS were observed in both sites. In Krafla, in addition to the observed prevalence of a crack system oriented in approximately N–S direction which is consistent with the direction of regional rift zone, fast shear-wave polarization directions along a general E–W direction are also persistent. In Hengill, the measurements and consequent inversions of the shear-wave splitting parameters have provided evidence for a predominant fracture system oriented approximately NNE-SSW which is consistent with the regional tectonics in SW Iceland.

Based on our previous research we have developed and consolidated a number of algorithms that can in principle make possible the automatic monitoring of subsurface

fracture systems in geothermal fields. Seismic data are collected from an array of three-component seismic sensors. When a seismic event is detected it will be readily located provided that the record is available at no less than four seismometers. If shear-wave splitting is determined to be present for an event, both parameters (φ and δt) will be automatically measured using a newly developed method based on the analysis of multiple time windows. An automated SWS algorithm is performed for a series of time windows to yield a series of estimated pairs of φ and δt, followed by a cluster analysis to finally determine the best estimate of polarization and time delay. Then, if the event is within the shear-wave window of any recording station, the measured parameters will be combined with all available measurements and used to invert for the orientation and intensity of cracks in the vicinity of that station.

ACKNOWLEDGEMENTS

I wish to thank Dr. Jose Rial, my advisor, for his continuous guidance and great support in the past four years. I also wish to thank my committee, Dr. Lees, Dr. Stewart, and Dr. Wagner, for their time, comments, and questions, which greatly improved the quality of this dissertation. Thanks to Ming Yang and Yang Zhao for their support, help, and friendship. Thank you Patricia, Deborah, Jo, and all the administrative staff for the great help you provided every day. Thanks to Darrell, whose technical assistance is most appreciated. Financial support was provided by the U.S. Department of Energy through grant DE-FG36-04GO14290, National Power Company of Iceland, Iceland GeoSurvey, and UNC Department of Geological Sciences (Martin-MacCarthy Graduate Research Fellowship). Finally my special thanks to my dear wife Li Liu, my parents and my parents-in-law for their selfless support.

TABLE OF CONTENTS

LIST OF TABLES

Table

LIST OF FIGURES

Figures

CHAPTER I

INTRODUCTION

Shear-wave splitting (SWS) occurs when a seismic wave travels through stress aligned fluid-filled fractures or other inclusions in the upper part of the earth's crust. It is becoming recognized as a powerful exploration tool for geothermal reservoirs as it can detect the geometry of the fracture system, the intensity of cracking and possibly, changes in fluid pressure within the reservoir. The method is based on the observation that a shear-wave propagating through rocks with stress-aligned microcracks (also known as extensive dilatancy anisotropy or EDA-cracks) will split into two waves, a fast one polarized parallel to the predominant crack direction, and a slow one, polarized perpendicular to it (Crampin, 1981, 1984; Babuska and Cara, 1991). The phenomenon is very similar to optical birefringence, whereby light transmitted through an anisotropic crystal undergoes analogous splitting and polarization parallel and perpendicular to the alignment of atoms in the crystal lattice. In the seismic case, the polarization direction of the fast split shear-wave parallels the strike of the predominant cracks regardless of its initial polarization at the source (Crampin et al., 1986; Peacock et al., 1988). The differential time delay between the arrivals of fast and the slow shear-waves (typically a few tens of milliseconds) is usually proportional to crack density, or number of cracks per unit volume within the rock body traversed by the seismic wave (Hudson, 1981; Crampin, 1987; Crampin and Lovell, 1991). Measuring the fast shear-wave polarization (φ) and time delay (δt) from local microearthquakes has thus become a valuable technique to detect the orientation and intensity of fracturing in the subsurface of fracture-controlled geothermal fields (e.g. Lou and Rial, 1997; Vlahovic et al., 2002a,b; Elkibbi and Rial, 2003, 2005; Elkibbi et al., 2004, 2005; Yang et al.,2003, 2005; Rial et al., 2005).

Two experiments were conducted in Krafla and Hengill geothermal fields in Iceland in the summers of 2004 and 2005 respectively to study shear-wave splitting in the areas of interest. Clear evidences of SWS were observed in both sites. In Krafla experiment, temporal variation of delay times along with the starting and stopping of well injection was observed. This suggested that shear-wave splitting can be a useful proxy to closely monitor transient changes in fluid pressure and possible fluid migrations in fractured reservoirs. In addition to the observed prevalence of a crack system oriented in approximately N–S direction which is consistent with the direction of regional rift zone, fast shear-wave polarization directions along a general E–W direction are also persistent. This unexpected direction is however consistent with results from a simultaneous MT (magnetotelluric) survey (Onacha et al., 2005). In Hengill, the measurements and consequent inversions of the shear-wave splitting parameters have provided evidence for a predominant fracture system oriented approximately NNE-SSW which is consistent with the regional tectonics in SW Iceland.

Taking into vision all our research group's previous efforts, we aim to develop a processing procedure towards the automatic detection of subsurface fractures in geothermal fields using shear-wave splitting. The approach rests on the integration of techniques recently developed by our research group to process and interpret shear-wave splitting measurements from natural (and injection-induced if available) microearthquakes. Traditional techniques to extract polarization and delay time information from split seismograms essentially include the visual analysis of two horizontal components and the standard cross-correlation method both of which require the manual selection of an appropriate time window by the operator which is time consuming and may introduce subjectivity. In the later part of this thesis we will propose a novel method of automatic detection of shear wave splitting parameters which actually extends the idea of automated time window selection and integrates a different measuring technique based on AIC function and a cluster analysis algorithm. This method inherits the advantage of high data processing speed of automated cluster analysis algorithms, meanwhile the integrated measuring technique avoids the subjectivity of window selection and manual quality control, consequently improving the accuracy of splitting parameter estimates and providing a convenient approach to process huge seismic datasets automatically and objectively. Finally we run several tests with the new method and according to the test results, the percentage of successful measurements can be higher than 70% for a surface station that records seismic data of various quality levels. With very good quality shear-wave splitting data (e.g. recorded by a downhole seismometer) the percentage of success can reach 80-90%.

References

Babuska, V. and Cara, M., 1991. *Seismic Anisotropy in the Earth*, Modern Approaches in Geophysics. Vol. 10, pp. 217, Kluwer Academic Publishers, The Netherlands.

Crampin, S., 1981. A review of wave motion in anisotropic and cracked elastic media. *Wave Motion*, **3**, 343-391.

Crampin, S., 1984. An introduction to wave propagation in anisotropic media. *Geophys. J. Roy. Astr. Soc.,* **76**, 17-28.

Crampin, S., Booth, D.C., Krasnova, M.A., Chesnokov, E.M., Maximov, A.B., and Tarasov, N.T., 1986. Shear-wave polarizations in the Peter the First range indicating crack-induced anisotropy in a thrust-fault regime. *Geophys. J. Roy. Astr. Soc.,* **84**, 401-412.

Crampin, S., 1987. Geological and industrial implications of extensive dilatancy anisotropy. *Nature,* **328**, 491-496.

Crampin, S. and Lovell, J.H., 1991. A decade of shear-wave splitting in the Earth's crust: What does it mean? What use can we make of it? And what should we do next? *Geophys. J. Int.,* **107**, 387-407.

Elkibbi, M. and Rial, J.A., 2003. Shear-wave splitting: an efficient tool to detect 3D fracture patterns at The Geysers, California. *Proc. Geothermal Reservoir Engineering*, Stanford, **28**, 143-149.

Elkibbi, M., Yang, M., and Rial, J.A., 2004. Imaging crack systems in The Geysers with shear-wave splitting. *Geothermal Resources Council (GRC) Transactions*, **28**, 789-800.

Elkibbi, M., Yang, M., and Rial, J.A., 2005. Crack-induced anisotropy models in The Geysers geothermal field. *Geophys. J. Int.*, **162**, 1036-1048.

Elkibbi, M. and Rial, J.A., 2005. The Geysers geothermal field: Results from shear-wave splitting analysis in a fractured reservoir. *Geophys. J. Int.*, **162**, 1024-1035.

Hudson, J.A., 1981. Wave speeds and attenuation of elastic waves in materials containing cracks. *Geophys. J. Roy. Astr. Soc.,* **64**, 133-150.

Lou, M. and Rial, J.A., 1997. Characterization of geothermal reservoir crack patterns using shear-wave splitting. *Geophysics*, **62**, 487-495.

Onacha, S., Kahn, D., Malin, P., and Shalev, E., 2005. Resistivity and microearthquake imaging of Krafla geothermal field, NE Iceland. *Transactions – Geothermal Resources Council*, **29**, 497-502.

Peacock, S., Crampin, S., Booth, D.C., and Fletcher, J.B., 1988. Shear-wave splitting in the Anza seismic gap, southern California: temporal variations as possible precursors. *J. Geophys. Res.,* **193**, 3339-3356.

Rial, J.A., Elkibbi, M., and Yang, M., 2005. Shear-wave splitting as a tool for the characterization of geothermal fractured reservoirs: Lessons learned. *Geothermics*, **34**, 365-385.

Vlahovic, G., Elkibbi, M., and Rial, J.A., 2002a. Shear-wave splitting and reservoir crack characterization: the Coso geothermal field. *J. Volcanol. Geothermal Res.*, **120**, 123-140.

Vlahovic, G., Elkibbi, M., and Rial, J.A., 2002b. Temporal variations of fracture directions and fracture densities in the Coso geothermal field from analyses of shear-wave splitting. *Proc. Geothermal Reservoir Engineering*, Stanford, **27**, 415-421.

Yang, M., Elkibbi, M., and Rial, J.A., 2003. Modeling of 3D crack attributes and crack densities in geothermal reservoirs. *Proc. Geothermal Reservoir Engineering*, Stanford, **28**, 321-327.

Yang, M., Elkibbi, M., and Rial, J.A., 2005. An inversion scheme to model subsurface fracture systems using shear wave splitting polarization and delay time observations simultaneously. *Geophys. J. Int.*, **160**, 939-947.

CHAPTER II

SHEAR-WAVE SPLITTING: A DIAGNOSTIC TOOL TO MONITOR FLUID PRESSURE IN GEOTHERMAL FIELDS

(Chuanhai Tang, Jose A. Rial, and Jonathan M. Lees)

Published in *Geophysical Research Letters (2005).*

Introduction

The Krafla volcanic system in northeastern Iceland is made up of the Krafla central volcano and an approximately 100 km long, transecting fissure swarm, with two high-temperature geothermal areas within it. One is located 5 km south of the Krafla caldera and the other, the NW-SE aligned Krafla-Leirhnúkur geothermal field, where this study was performed, is located inside the Krafla caldera. There is a shallow crustal magma reservoir with an upper boundary at a depth of approximately 3 km, near the center of inflation in the caldera (Einarsson, 1978).

During the months of July and August 2004, a twenty-station three-component seismic array with L-28 MARK4 4.5-Hz seismic sensors was deployed around the Krafla geothermal field, covering an area approximately 5 km in N-S by 4 km in E-W. Between 5 July and 11 August the array continuously recorded the seismic activity in the region surrounding the injection well K-26. The data were collected at a rate of 500 samples per second.

One objective of the deployment is to use various seismic data processing techniques such as high precision earthquake location, shear-wave splitting, and tomographic inversion to detect the orientation, density and fluid content of the main subsurface fracture systems in Krafla. In addition, an experiment was designed with the collaboration of Landsvirkjun, the power company that runs the Krafla field, to stop and start injection into well K-26 with the objective of determining any change in shear-wave splitting parameters (polarization of the fast wave, time delay between the fast and slow waves) that may accompany a scheduled stopping and resumption of injection. Injection was stopped on 15 July and resumed 11 days later on 26 July. It turns out that the response of the subsurface crack systems to these transient changes in water pressure can in fact be detected with seismic waves, which can potentially provide invaluable information on the preferred directions of fluid migration in the reservoir. The results obtained at Krafla are totally consistent with those of a similar experiment carried out in 2001 in the Coso geothermal field in California. The immediate inference is that the delay time of split shear waves may be a proxy for reservoir fluid pressure, as shall be discussed in what follows.

Shear-wave Splitting Observations at Krafla

Shear-wave splitting is an exploration method of proven reliability and unique imaging power. The method is based on the fact that a shear-wave propagating through rocks with stress-aligned micro-cracks will split into two waves, a fast one polarized parallel to the predominant crack direction, and a slow one polarized perpendicular to it (Crampin, 1981, 1984; Babuska and Cara, 1991). The polarization direction of the fast shear wave (φ) parallels the strike of the predominant cracks regardless of its initial polarization at the source in a single fracture set (Crampin et al., 1986; Peacock et al., 1988). The differential time delay between the arrivals of the fast and slow shear waves (δt) is closely related to crack density, or number of cracks per unit volume within the rock, and crack aspect ratio (Hudson, 1981; Crampin, 1987; Crampin and Lovell, 1991). Thus measuring the fast-shear wave polarization and time delay from local microearthquakes has become a valuable technique to detect the orientation and intensity of fracturing in the subsurface of fracture-controlled geothermal fields (e.g. Lou and Rial, 1997; Vlahovic et al., 2002a, 2002b; Elkibbi and Rial, 2003, 2005; Elkibbi et al., 2004, 2005; Yang et al., 2003, 2005; Rial et al., 2005).

Figure 2.1(a) shows the epicenters of microearthquakes located during the period 5 July to 11 August, 2001. Figure 2.1(b) shows the depth distribution of these events along N-S and E-W cross-sections respectively. The velocity model used is from Brandsdóttir et al. (1997). It can be seen that the epicenters roughly align along the E-W direction, while focal depths are shallow around the injection well, mostly shallower than 4 km. Seismicity at Krafla is not very high, and during the operation the array detected an average of four well-recorded events per day (observed at five or more stations).

Shear-wave splitting is clearly recorded at Krafla at most stations and shows the prevalence of at least two major crack systems oriented approximately N-S and E-W. We have measured the fast shear-wave polarization and time delay of shear-wave splitting events recorded at ten selected stations (P03, P04, P06, P10, P11, P13, P14, P15, P16, and P23). These stations are selected because they either recorded the data of best quality (P13, P14, P23) or have a relatively good coverage of ray paths coming from different azimuths (P03, P04). Stations P06, P10, P11, P15, and P16 are chosen because they are the nearest to the injection well K-26.

Fast shear-wave polarization angle φ is measured by interactive rotation of the seismogram until the horizontal particle motion plot shows that fast and slow shear-waves are oriented along the instrument's horizontal components. Angle of rotation from the original polarization direction determines φ. Meanwhile the two shear-wave arrivals, which are often coupled in the original recording, separate out in time domain and δt can then be directly measured. In this study δt is normalized by dividing it by the length of the ray path in order to correctly compare delays from different paths. Figure 2.2 shows the rose diagrams (polar histograms) of fast shear-wave polarization directions observed within the shear-wave window of the ten stations. The predominant polarization directions observed at stations P13, P15, P16 and P23 are close to E-W or NW-SE, and those at P04, P10 and P11 are generally close to N-S, while P03, P06 and P14 display two major sets of polarizations nearly perpendicular to each other, striking close to N-S and E-W respectively.

Time Delay Variations with Fluid Injection at Krafla and Coso

Normalized time delays observed at Krafla are mostly less than 20 ms/km, whereas there are still some cases with very large normalized δt (> 30 ms/km). Our focus is on stations P06, P10, P11, P15 and P16 since they are the closest to the injection well K-26 and are expected to provide additional information about the relationship, if any, between the shear-wave splitting events and the ongoing injection. The normalized time delays observed at these five stations throughout the experiment are shown in Figure 2.3(b). Time delays drop significantly after the injection stops and maintain at a lower level until increasing again right after the injection resumes. The *t*-test results show that the time delays during the first injection period are different from those during the absence of injection at 99% confidence level (t value = 3.16), and the time delays before and after the injection resumes are different at 68% confidence level (t value = 0.995).

In March 2001 a similar injection experiment was conducted, but in an opposite way, at the Coso geothermal field in central California (Vlahovic et al., 2002c; Rial et al., 2005). Injection into the well was initiated briefly for one day on 13 March, and was restarted on 20 March and maintained on for one week before being stopped on 27 March. The normalized time delays observed in this experiment are shown in Figure 2.3(a). Compared with the observations from Krafla, it can be seen that in both experiments the crack systems are responding promptly in the same way to the transient changes in fluid pressure, i.e. large time delays occur only during the injection phases and drop to a lower level without the injection.

In addition, it should also be noticed that in both experiments large normalized time delays take place only at depths around and shallower than the injection as shown in the bottom panel in Figure 2.3, which strongly implies that the observed large normalized time delays are mostly due to the injection. Therefore, all of these observational facts indicate that the injection has either opened new fractures or increased the aspect ratio. In both Coso and Krafla, however, we have not found significant changes in the polarization angles during the experiments. Further study on the time pattern of φ is already underway.

Thus, normalized time delay may be used as a proxy of changes in fluid pressure and possible fluid migrations. Explaining these changes in terms of crack mechanics and the action of fluids in hot rock is not simple, and we are still far from fully understanding what these observations mean. Nevertheless, the significant changes in time delays strongly suggest that detection of time delays of split shear waves can be a useful diagnostic tool for monitoring crack intensities and fluid behaviors in a producing geothermal field.

Conclusions

There is clear evidence of shear-wave splitting in Krafla's seismic data. In addition to the observed prevalence of a crack system oriented approximately in N-S which is consistent with the anticipated direction of major fractures in the area, fast shear-wave polarizations along a general E-W direction are also persistent as observed at stations P13, P15, P16 and P23. The influence of fluid injection on fracture systems can be clearly illustrated by the observation of changes in the normalized time delays. Therefore, normalized time delays measured from well recorded shear-wave splitting events can provide a useful tool to closely monitor transient changes in fluid pressure and possible fluid migrations in fractured reservoirs.

References

Babuska, V., and Cara, M., 1991. *Seismic Anisotropy in the Earth*, Modern Approaches in Geophysics, Vol. 10, pp. 217, Kluwer Academic Publishers, The Netherlands.

Brandsdóttir, B., Menke, W., Einarsson, P., White, R.S., and Staples, R.K., 1997. Faroe-Iceland Ridge Experiment 2. Crustal structure of the Krafla central volcano, *J. Geophys. Res.,* **102***,* 7867-7886.

Crampin, S., 1981. A review of wave motion in anisotropic and cracked elastic media, *Wave Motion*, **3***,* 343-391.

Crampin, S., 1984. An introduction to wave propagation in anisotropic media, *Geophys. J. Roy. Astr. Soc.,* **76***,* 17-28.

Crampin, S., Booth, D.C., Krasnova, M.A., Chesnokov, E.M., Maximov, A.B., and Tarasov, N.T., 1986. Shear-wave polarizations in the Peter the First range indicating crack-induced anisotropy in a thrust-fault regime, *Geophys. J. Roy. Astr. Soc.,* **84***,* 401-412.

Crampin, S., 1987. Geological and industrial implications of extensive dilatancy anisotropy, *Nature,* **328**, 491-496.

Crampin, S., and Lovell, J.H., 1991. A decade of shear-wave splitting in the Earth's crust: What does it mean? What use can we make of it? And what should we do next? *Geophys. J. Int.,* **107***,* 387-407.

Einarsson, P., 1978. S-wave shadows in the Krafla caldera in NE-Iceland, evidence for a magma chamber in the crust, *Bull. Volcanol.,* **41***,* 1-9.

Elkibbi, M., and Rial, J.A., 2003. Shear-wave splitting: an efficient tool to detect 3D fracture patterns at The Geysers, California, *Proc. Geothermal Reservoir Engineering*, Stanford, **28***,* 143-149.

Elkibbi, M., Yang, M., and Rial, J.A., 2004. Imaging crack systems in The Geysers with shear-wave splitting, *Geothermal Resources Council (GRC) Transactions*, **28**, 789-800.

Elkibbi, M., Yang, M., and Rial, J.A., 2005. Crack-induced anisotropy models in The Geysers geothermal field, *Geophys. J. Int.*, **162**, 1036-1048.

Elkibbi, M., and Rial, J.A., 2005. The Geysers geothermal field: results from shear-wave splitting analysis in a fractured reservoir, *Geophys. J. Int.*, **162**, 1024-1035.

Hudson, J.A., 1981. Wave speeds and attenuation of elastic waves in materials containing cracks, *Geophys. J. Roy. Astr. Soc.,* **64**, 133-150.

Lou, M., and Rial, J.A., 1997. Characterization of geothermal reservoir crack patterns using shear-wave splitting, *Geophysics*, **62***,* 487-495.

Peacock, S., Crampin, S., Booth, D.C., and Fletcher, J.B., 1988. Shear-wave splitting in the Anza seismic gap, southern California: temporal variations as possible precursors, *J. Geophys. Res.,* **193**, 3339-3356.

Rial, J.A., Elkibbi, M., and Yang, M., 2005. Shear-wave splitting as a tool for the characterization of geothermal fractured reservoirs: lessons learned, *Geothermics*, **34**, 365-385.

Vlahovic, G., Elkibbi, M., and Rial, J.A., 2002a. Shear-wave splitting and reservoir crack characterization: the Coso geothermal field, *J. Volcanol. Geothermal Res.*, **120**, 123-140.

Vlahovic, G., Elkibbi, M., and Rial, J.A., 2002b. Temporal variations of fracture directions and fracture densities in the Coso geothermal field from analyses of shear-wave splitting, *Proc. Geothermal Reservoir Engineering*, Stanford, **27**, 415-421.

Vlahovic, G., Yang, M., and Rial, J.A., 2002c. Fracture characterization using shear-wave splitting: results from a high density temporary array in the Coso geothermal field, *Eos. Trans. AGU*, **83***(19)*, Spring Meet. Suppl., Abstract S51A-07.

Yang, M., Elkibbi, M., and Rial, J.A., 2003. Modeling of 3D crack attributes and crack densities in geothermal reservoirs, *Proc. Geothermal Reservoir Engineering*, Stanford, **28**, 321-327.

Yang, M., Elkibbi, M., and Rial, J.A., 2005. An inversion scheme to model subsurface fracture systems using shear wave splitting polarization and delay time observations simultaneously, *Geophys. J. Int.*, **160**, 939-947.

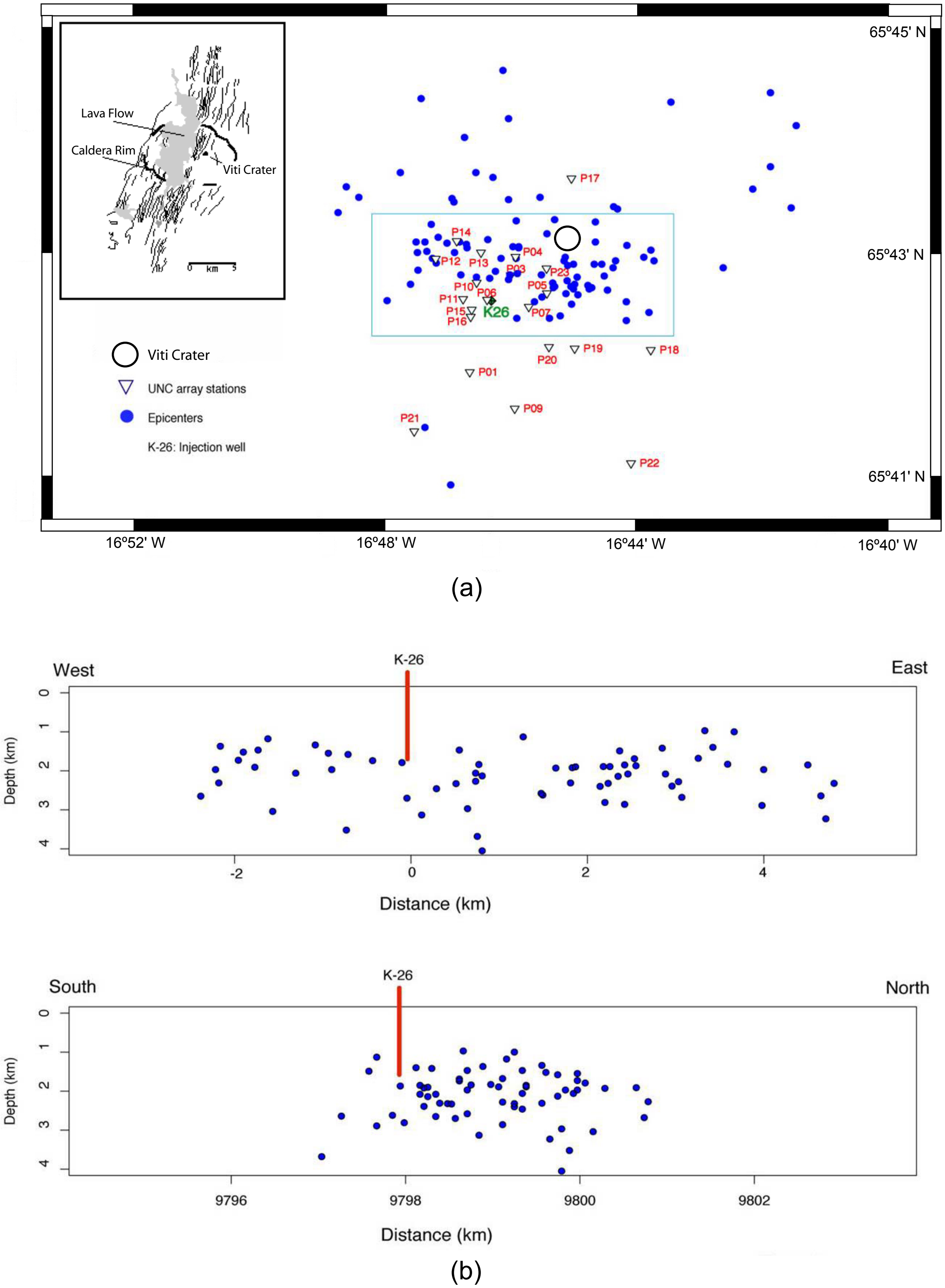

Figure 2.1. The seismicity recorded by UNC array from 5 July to 11 August is shown in (a). Totally 129 earthquakes are located. The focal depth distribution of the events located around the injection well K-26 (inside the rectangle) is shown in (b).

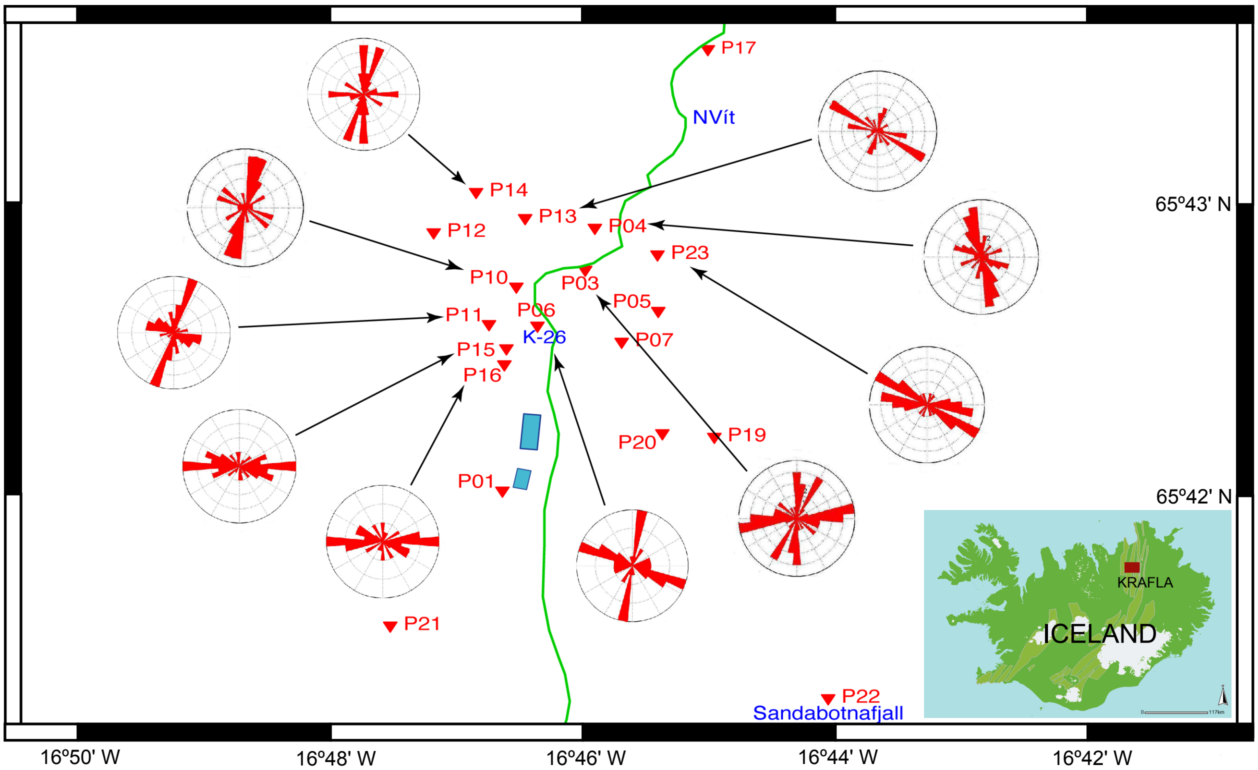

Figure 2.2. Rose diagrams (polar histograms) of the fast shear-wave polarization directions observed at the ten selected stations. See details in the text.

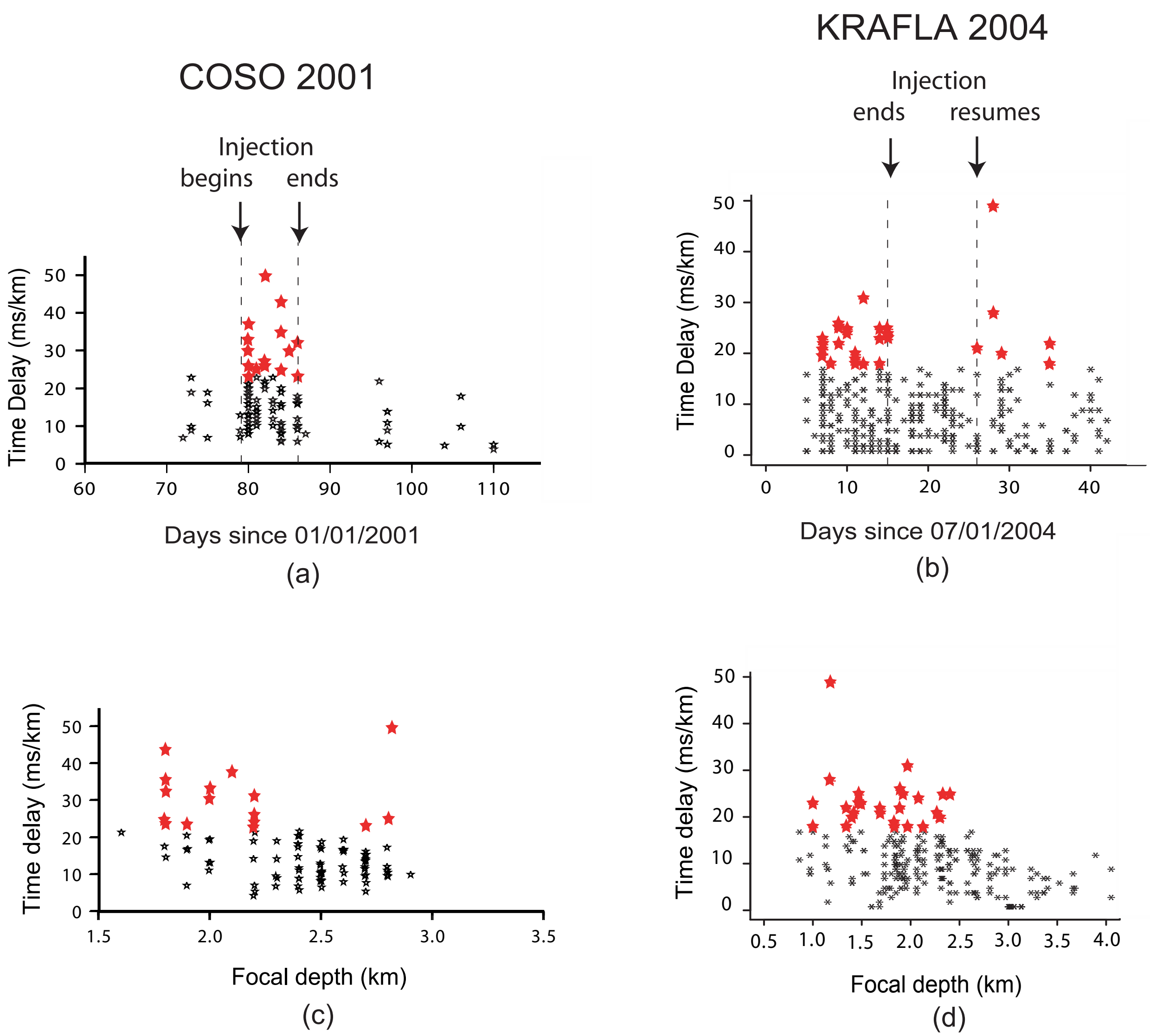

Figure 2.3. (a) Delay times strongly increase during injection and drop back to normal values right after injection ends. Time delays greater or equal to ~25 ms/km occur only during the injection and are marked in red. (b) Time delays significantly drop after the injection stops and increase again right after the injection resumes. Time delays greater than or equal to ~18 ms/km occur only during the injection and are marked in red. (c)(d) Large normalized time delays appear to occur only at depths shallower than and around the injection. For both cases, data selected are those from stations closest to the injection wells.

CHAPTER III

SEISMIC IMAGING OF THE GEOTHERMAL FIELD AT KRAFLA, ICELAND USING SHEAR-WAVE SPLITTING

(Chuanhai Tang, Jose A. Rial, and Jonathan M. Lees)

Published in *Journal of Volcanology and Geothermal Research (2008).*

Introduction

The Krafla volcanic system, located within the Northern Volcanic Zone of Iceland, is made up of the Krafla central volcano and an approximately 100 km long, transecting fissure swarm. The central volcano is a major eruptive center less than 500,000 years old, approximately 21 km long by 17 km wide and enclosing a 10 km by 7 km caldera formed 100,000 years ago during the last interglacial period. Two high-temperature geothermal areas occur within the Krafla volcanic system. The NW-SE aligned Krafla-Leirhnúkur geothermal field, where this study was performed, is located inside the Krafla caldera. The other is located within the fissure swarm, 5 km south of the Krafla caldera. The eastern part of the Krafla-Leirhnúkur geothermal field is utilized by the Krafla power plant which started operation in 1978. There is a shallow crustal magma reservoir with an upper boundary at a depth of approximately 3 km, near the center of the caldera (Einarsson, 1978). This magma chamber is smaller than the caldera, about 2-3 km in N-S and 8-10 km in E-W, with a thickness of 0.75-1.8 km (Brandsdóttir et al., 1997). Geodetic measurements support the existence of a shallow magma chamber at a depth of 3 km within the caldera and have been used to argue for the existence of multiple magma reservoirs at depth (Tryggvason, 1986).

During the months of July and August 2004, a twenty-station, three-component seismic array was deployed around the Krafla geothermal field, covering an area approximately 5 km N-S by 4 km E-W. Between July 5th and August 11th the array continuously recorded the seismic activity in the region surrounding the injection well K-26 located 1 km north of the Krafla power plant. Each station in the seismic array consisted of a three-component short-period MARK4 L-28 (4.5 Hz) seismic sensor, a data-logger or DAS (Data Acquisition System), a GPS antenna, and a 12V car battery. The data were collected continuously at a rate of 500 samples per second.

The main objective of this experiment was to use shear-wave splitting (SWS) as a tool to detect the orientation, density and fluid content of the main subsurface fracture systems within the Krafla-Leirhnúkur geothermal field. Besides the passive seismic survey an experiment was conducted whereby injection in well K-26 was stopped on July 15th and subsequently resumed on July 26th. We hoped that the response of the subsurface crack system to these transient changes in water pressure could be detected with seismic waves and provide useful information about the preferred directions of fluid migration in the reservoir.

Figure 3.1(a) shows the epicenters of seismic events located from July 5th to August 11th along with the distribution of the stations in the array, and Figure 3.1(b) shows the depth distribution of the events along N-S and E-W cross-sections respectively. The locating program (“lquake”) employs a standard non-linear inverting algorithm based on Geiger’s Method (e.g. Lee and Stewart, 1981) to determine the origin time and hypocenter of earthquakes using a 1-D velocity model. The velocity model used in this study is from Brandsdóttir et al. (1997). It is apparent that the epicenters are roughly aligned along the E-W direction of the Krafla-Leirhnúkur geothermal field. Hypocenters are shallow around the injection well with most focal depths being shallower than 2 km.

Seismicity at Krafla was low during the experiment. During its operation the array detected an average of four well-recorded events per day recorded at five or more stations. These are very small earthquakes with magnitudes mostly no greater than 2. Microseismicity within the Krafla region is somewhat obscured by the high level of seismic noise from vibrations of the steam pipes, routine plant operations, tourists, local traffic, etc. To avoid strong sources of noise, several stations were relocated to quieter sites. Some stations deployed in abandoned well cellars had a mixed performance, some noisy and some not. In spite of occasional and instrumental interruptions the array performed well, recording over 300 GB of data.

Shear-wave Splitting Analysis of Krafla Seismic Data

Shear-wave Splitting

Shear-wave splitting (SWS) is a valuable technique of exploration. The method is based on the observation that a shear-wave propagating through rocks with stress-aligned micro-cracks (also known as extensive dilatancy anisotropy or EDA-cracks) will split into two waves, a fast one polarized parallel to the predominant crack direction, and a slow one, polarized perpendicular to it (Crampin, 1981, 1984; Babuska and Cara, 1991). The phenomenon is very similar to optical birefringence, whereby light transmitted through an anisotropic crystal undergoes analogous splitting and polarization parallel and perpendicular to the alignment of atoms in the crystal lattice. In the seismic case, the polarization direction of the fast split shear wave parallels the strike of the predominant cracks regardless of its initial polarization at the source (Crampin et al., 1986; Peacock et al., 1988). The differential time delay between the arrival of the fast and the slow shear waves (typically a few tens of milliseconds) is proportional to crack density, or number of cracks per unit volume within the rock body traversed by the seismic wave (Hudson, 1981; Crampin, 1987; Crampin and Lovell, 1991). Measuring the fast-shear wave polarization and time delay from local microearthquakes has thus become a valuable technique to detect the orientation and intensity of fracturing in the subsurface of fracture-controlled geothermal field (e.g. Lou and Rial, 1997; Vlahovic et al., 2002a, b; Elkibbi and Rial, 2003, 2005; Elkibbi et al., 2004, 2005; Yang et al., 2003; Rial et al., 2005; Tang et al., 2005).

In cracked geothermal reservoirs such as Krafla the anisotropy is likely to have been caused by aligned systems of open, fluid-filled micro-fractures. Fortunately, the anisotropy effects on seismic waves induced by small, aligned open cracks in an otherwise isotropic rock are indistinguishable from those produced by an unfractured, but transversely isotropic medium. Seismic anisotropy characterizes the Neovolcanic zones of Iceland where shear-wave splitting of 0.1-0.3 s have been observed (Menke et al., 1994). Shear-wave splitting was clearly recorded at most of the Krafla stations. In fact, we have recorded unusually well developed splitting, in which the fast and slow shear waves are naturally separated in time, that strongly points to the prevalence of at least two fracture systems oriented approximately in N-S and E-W. Figure 3.2(a) shows evidence for a strong, nearly E-W fast shear-wave polarization that suggests the presence of E-W oriented, probably vertical cracks in the neighborhood of the station. Figure 3.2(b) shows evidence of a N8°E fast shear-wave polarization, close to the overall N15°E strike of the normal faults of the Krafla rift zone. Indeed, SWS has detected not only the predominant N-S fabric related to the rift zone, but also provides strong evidence for an equally pervasive E-W oriented lineament of subsurface fractures.

Measuring Polarization and Time Delay

The polarization direction of the fast split shear-wave is usually parallel to the strike of the predominant cracks, regardless of its initial polarization at the source, and the time delay between the fast and the slow waves is proportional to the crack density, assuming constant crustal velocities. These split shear-wave parameters (fast shear-wave polarization direction φ and differential time delay δt) constitute a valuable data set to invert for the subsurface fracture geometry and to estimate the crack density and permeability within fractured geothermal reservoirs. An important limitation to shear-wave splitting analysis is that seismic rays must be within the shear-wave window of the seismic stations. This window can be visualized as a right circular cone with vertex at the station and vertex angle $i_c = \sin^{-1}(\beta/\alpha)$, where α and β are the P- and S-wave surface velocities, respectively. For angles of incidence greater than i_c, shear waves interactive strongly with the free surface, distorting the incoming waveform (Crampin, 1981; Booth and Crampin, 1985). For a half space with a typical Poisson's ratio of 0.25, the window's vertex angle, as measured from the vertical, is equal to 35.2°. All earthquakes used for the study in this paper are restricted within this window.

For the purpose of this study, we use those φ and δt measurements from the Krafla array that correspond to high signal-to-noise ratio seismograms displaying linear horizontal particle motion and a clear well-defined shear-wave splitting event. Polarization diagrams (also known as particle motion plots) are used to accurately detect the switch in polarity of the two orthogonally polarized fast and slow shear-waves and to measure the split parameters φ and δt. Fast shear-wave polarization angle φ is measured by interactive rotation of the seismogram until the horizontal particle motion plot shows that fast and slow shear-waves are oriented along the instrument's horizontal components. Angle of rotation from the original polarization direction determines φ. At the same time, the two shear-wave arrivals, which are often coupled in the original recording, separate out in time domain (see examples in Figure 3.2) and δt can then be directly measured.

So far the seismic data from ten selected stations (P03, P04, P06, P10, P11, P13, P14, P15, P16, and P23) have been investigated to measure the fast shear-wave polarization and time delay. These stations are selected because they either recorded the data of best quality (P13, P14, P23) or have a relatively good coverage of ray paths coming from different azimuths (P03, P04). Stations P06, P10, P11, P15, and P16 are chosen because they are the nearest to the injection well K-26 thus are expected to provide additional information about the relationship, if any, between the shear-wave splitting events and the ongoing injection. Figure 3.3 shows the equal-area rose diagrams (polar histograms) of fast shear-wave polarization directions observed within the shear-wave window of the ten stations. The bin size in the rose diagrams is 10° and the length of each bin is proportional to the number of polarizations within it. It can be seen from Figure 3.3 that the predominant polarization directions observed for stations P13, P15, P16 and P23 are close to E-W and those for stations P04, P10 and P11 are close to N-S direction, while stations P03, P06 and P14 display two major subsets of polarizations nearly perpendicular to each other, striking close to N-S and E-W directions respectively. Of all the stations in the array station P13 has recorded the best data with highest signal-to-noise ratio. On the contrary, station P03 is very close to the road while P06 is close to the injection well (see Figure 3.3), thus the data recorded at these two stations are worst stained by noise. This might have been one reason, among others as discussed later, to cause the more complicated polar diagrams at these two stations than others. Generally speaking, the quality of data recorded at these ten stations can be ranked between medium and high.

It should be noted that except stations P13 and P14, which are located in a relatively flat environment, most of the other analyzed stations are put on hills or cliffs. Crampin (1993; personal communication) suggested that rugged topography around the surface station may have severe effects and in very irregular topographies the polarizations can easily show 90°-flips. Observationally, rose diagrams with consistent and robust polarizations for all azimuths occur in areas of gentle to flat topography, while scattered polarizations may indicate the proximity of cliffs or stations on small hills (Volti and Crampin, 2003a). The wide range of rose-diagram directions we have observed may well be caused by the interaction with irregularities in surface topography. This may also explain why the polarization patterns at some stations are exceptionally complicated.

To inspect the azimuthal distribution of polarization angles, equal-area projection plot of the observed polarizations at station P13, as an example, is shown in Figure 3.4(a). For all the ten stations most shear-wave splitting events within the shear-wave window actually come from the NE and/or SE quadrants and fewest from the SW quadrant, which can be compared with the distribution of located epicenters in Figure 3.1. Plotted in

Figure 3.4(b) are the time delays observed at P13 which are showing the typical ±80% scatter always associated with measurements above microearthquakes (Crampin et al., 2004).

Inversion Method and Results

The pairs of anisotropy-related parameters, fast shear-wave polarization direction φ and differential time delay δt, read from the seismograms recorded at the ten selected seismic stations at Krafla provide a preliminary means of detecting the key subsurface fracture characteristics in the reservoir. Polarization orientations help delineate stress-aligned crack directions that represent potential conduits for subsurface fluid flow, while crack densities inferred from differential time delays may offer good prospects of depicting target-zones of increased cracking density and rock permeability within the reservoir rocks.

Methodology

The SWS method relies on the observation that in a mechanically anisotropic medium such as a fractured reservoir, fast shear-wave polarization orientations are independent of the initial polarization of the shear-wave at the source and are mainly caused by the medium's anisotropy (e.g. Crampin et al., 1986; Peacock et al., 1988; Crampin and Lovell, 1991). Station-by-station inversion for subsurface crack strike, dip and density is performed through successive trial-and-error comparisons of observed and theoretical fast shear-wave polarizations and associated time delays plotted in equal-area projections as functions of ray azimuth and angle of incidence (Yang, 2003). The elastic stiffness proposed by MacBeth (1999) was used for Transverse Isotropic (TI) conditions to simulate the general 3-D mechanical properties of the fractured solid.

In addition to the time consuming trial-and-error process, a self-consistent algorithm was developed for inverting the measurements of polarizations and time delays of split shear waves for the crack strike, dip and density (Yang et al., 2005). Since we are going to estimate the crack properties from two separate datasets, we are facing a double-response regression problem (Draper and Smith, 1998). In general, it is unlikely that both datasets give us the same regressed results. For this reason, Yang's inversion scheme divides the original double-response inversion problem into two connected single-response ones by taking advantage of the inherent characteristics of the observed φ and δt. Please refer to Yang et al. (2005) for more details of this approach.

Inversion Results

Essentially, the inversion procedure is expected to identify regions of different crack densities in the Krafla geothermal field and invert for 3-D fracture geometry in the subsurface. Based on seismic ray coverage and depending on the spatial patterns and azimuthal distributions of observed polarizations and time delays in the equal-area projection plots, crack-induced anisotropy is modeled by 1) a single system of vertical cracks, 2) a single system of non-vertically dipping cracks, or 3) two intersecting sets of vertically and/or non-vertically dipping cracks. Most of the stations we have analyzed showed just one chief polarization direction (Figure 3.3). The recording of a single prevalent polarization may in general be accounted for by anisotropic effects due to parallel vertical cracks. In such case, the chief polarization orientation is parallel to the strike of the main crack system in the neighborhood of the station.

Considering the presence of irregular surface topography surrounding most of the ten stations, only the events with shear-wave splitting that are strictly inside the 35.2°-cone shear-wave window are selected for the inversion of each station, although this will reduce the number of events used in the inversion procedure. The inversion results for crack strike, crack dip, and crack density using the measured fast shear-wave polarization directions and differential time delays from the ten selected seismic stations at the Krafla geothermal field are briefly listed in Table 1 and graphically illustrated in Figure 3.5. Also listed in the table is the goodness-of-fit of the model computed for each station inverted. For more than half of the stations the goodness-of-fit is greater than 60%. Compared to the results of other stations, the shallow dip angle and high crack density obtained for stations P03, P06 and P11 may indicate that the fracture model of a single set of vertical or non-vertically dipping cracks is probably not appropriate in these cases, and a double-set model of cracks might be necessary. Although it is possible that this implies the existence of a set of densely packed, shallow dipping cracks indeed, which still needs to be justified with other geological and/or geophysical evidence, we notice that for these three stations the shear-wave splitting events are coming mostly (over 80%) from the NW and NE quadrants on the equal-area projection (see Figure 3.3), which may have been the reason to cause this. All the other inversion results are generally consistent with the assumption of the single-set crack model in terms of their relatively steep dip angles and low crack densities. The crack strikes inverted for stations P04, P13, P15, P16 and P23 are close to E-W direction while for stations P10 and P14 the strikes are close to N-S direction. These results indicate again that there may exist two different major systems of fractures in Krafla. As an example, the fitting between the observed and theoretical fast shear-wave polarizations for station P13 is plotted in the equal-area projection as shown in Figure 3.4(c). The fit is generally good although there are still some cases in which the observed and theoretical polarizations are nearly perpendicular to each other.

Shown in Figure 3.6 are the residual contours computed for stations P13 and P23 for the purpose of determining the crack strike, crack dip and crack density corresponding to the minimum of residuals in fast shear-wave polarizations and/or time delays. It is anticipated that the resulting pairs of crack strike and crack dip inferred from the global RMSRF (Root-mean-square Residue Function) minima in both residual contours are the same or very close to each other as in the case for station P23, although actually the results from the two contours may be quite different from each other, probably because, as stated before, the measurement of time delays technically involves much more uncertainties than that of polarizations. For this reason we have listed in Table 1 only the inversion results obtained from the residual contour computed using fast shear-wave polarizations for each analyzed station.

Conclusions

There is clear evidence of shear-wave splitting within the Krafla-Leirhnúkur geothermal area. In addition to the observed prevalence of a crack system oriented in approximately N-S direction which is consistent with the direction of the Krafla rift zone, fast shear-wave polarization directions along a general E-W direction are also persistent as indicated at stations P13, P15, P16 and P23. Onacha et al. (2005) also found an approximately E-W oriented high anisotropy zone which is highly correlated with the location of microearthquakes in their magnetotelluric study above exactly the same area as in this study. In the four-year study of shear-wave splitting in Iceland conducted by Volti and Crampin (2003a, 2003b) there was no station right above the Krafla field recording shear-wave splitting, and even the one closest to Krafla (REN in Figure 3.4 of 2003a) also showed a high scatter of fast shear-wave polarizations.

Inversion results show that most cracks have a relatively steep dip; however, the results for stations P06 and P11 indicate that the shallow dip of the cracks (<40°) may indeed be related to fractures associated with the overall shape of the Krafla-Leirhnúkur geothermal field, which stretches between the two regions of shear wave attenuation imaged by Einarsson (1978). As the source volume of most of our events lies between 1-2 km depth, fractures at this depth are likely to be formed by deformation within the near-surface, extrusive part of the crust, dike injections, or the strike-slip across the divergent plate boundary. Figure 3.7 shows some of the major geological lineament structures to the north of Iceland. It seems that the NW-SE oriented fracture systems detected by this study could also be interpreted as the subsurface continuation of Dalvik Lineament. The magnitude of splitting delays is similar to what has been observed elsewhere within the Neovolcanic Zone of Iceland (Menke et al., 1994). The high scatter of time delays are also observed by Volti and Crampin (2003a, 2003b) and should be accounted for by similar explanations thereof.

Finally, it has to be noted that the number of microearthquakes located and used in the analysis and inversion is really limited (approximately 35 for each station on average). Also because of the high noise level in some seismic recordings, for some stations one has had to be very careful in determining the presence of shear-wave splitting and measuring the two SWS parameters.

References

Babuska, V. and Cara, M., 1991. *Seismic Anisotropy in the Earth*, Modern Approaches in Geophysics. Vol. 10, pp. 217, Kluwer Academic Publishers, The Netherlands.

Booth, D.C. and Crampin, S., 1985. Shear-wave polarizations on a curved wavefront at an isotropic free-surface, *Geophys. J. Roy. Astr. Soc.,* **83**, 31-45.

Brandsdóttir, B., Menke, W., Einarsson, P., White, R.S., and Staples, R.K., 1997. Faroe-Iceland Ridge Experiment 2. Crustal structure of the Krafla central volcano. *J. Geophys. Res.,* **102**, 7867-7886.

Crampin, S., 1981. A review of wave motion in anisotropic and cracked elastic media. *Wave Motion*, **3**, 343-391.

Crampin, S., 1984. An introduction to wave propagation in anisotropic media. *Geophys. J. Roy. Astr. Soc.,* **76**, 17-28.

Crampin, S., Booth, D.C., Krasnova, M.A., Chesnokov, E.M., Maximov, A.B., and Tarasov, N.T., 1986. Shear-wave polarizations in the Peter the First range indicating crack-induced anisotropy in a thrust-fault regime. *Geophys. J. Roy. Astr. Soc.,* **84**, 401-412.

Crampin, S., 1987. Geological and industrial implications of extensive dilatancy anisotropy. *Nature,* **328**, 491-496.

Crampin, S. and Lovell, J.H., 1991. A decade of shear-wave splitting in the Earth's crust: What does it mean? What use can we make of it? And what should we do next? *Geophys. J. Int.,* **107**, 387-407.

Crampin, S., 1993. A review of the effects of crack geometry on wave propagation through aligned cracks. *Can. J. Expl. Geophys.*, **29**, 3-17.

Crampin, S., Peacock, S., Gao, Y., and Chastin, S., 2004. The scatter of time-delays in shear-wave splitting above small earthquakes. *Geophys. J. Int.*, **156**, 39-44.

Draper, N. and Smith, H., 1998. *Applied regression analysis*, 3rd Edition. A Wiley Interscience Publication, New York.

Einarsson, P., 1978. S-wave shadows in the Krafla caldera in NE-Iceland, evidence for a magma chamber in the crust. *Bull. Volcanol,,* **41**, 1-9.

Elkibbi, M. and Rial, J.A., 2003. Shear-wave splitting: an efficient tool to detect 3D fracture patterns at The Geysers, California. *Proc. Geothermal Reservoir Engineering*, Stanford, **28**, 143-149.

Elkibbi, M., Yang, M., and Rial, J.A., 2004. Imaging crack systems in The Geysers with shear-wave splitting. *Geothermal Resources Council (GRC) Transactions*, **28**, 789-800.

Elkibbi, M., Yang, M., and Rial, J.A., 2005. Crack-induced anisotropy models in The Geysers geothermal field. *Geophys. J. Int.*, **162**, 1036-1048.

Elkibbi, M. and Rial, J.A., 2005. The Geysers geothermal field: Results from shear-wave splitting analysis in a fractured reservoir. *Geophys. J. Int.*, **162**, 1024-1035.

Hudson, J.A., 1981. Wave speeds and attenuation of elastic waves in materials containing cracks. *Geophys. J. Roy. Astr. Soc.,* **64**, 133-150.

Lee, W. H. K. and Stewart, S.W., 1981. *Principles and applications of microearthquake networks*, Advances in Geophysics supplement 2. Academic Press, New York.

Lou, M. and Rial, J.A., 1997. Characterization of geothermal reservoir crack patterns using shear-wave splitting. *Geophysics*, **62**, 487-495.

MacBeth, C., 1999. Azimuthal variation in P-wave signatures due to fluid flow. *Geophysics*, **64**, 1181-1192.

Menke, W., Brandsdóttir, B., Jakobsdóttir, S., and Stefánsson R., 1994. Seismic anisotropy in the crust at the mid-Atlantic plate boundary in south-west Iceland. *Geophys. J. Int.*, **119**, 783-790.

Onacha, S., Kahn, D., Malin, P., and Shalev, E., 2005. Resistivity and microearthquake imaging of Krafla geothermal field, NE Iceland. *Transactions – Geothermal Resources Council*, **29**, 497-502.

Peacock, S., Crampin, S., Booth, D.C., and Fletcher, J.B., 1988. Shear-wave splitting in the Anza seismic gap, southern California: temporal variations as possible precursors. *J. Geophys. Res.,* **193**, 3339-3356.

Rial, J.A., Elkibbi, M., and Yang, M., 2005. Shear-wave splitting as a tool for the characterization of geothermal fractured reservoirs: Lessons learned. *Geothermics*, **34**, 365-385.

Tang, C., Rial, J. A., and Lees, J. M., 2005. Shear-wave splitting: A diagnostic tool to monitor fluid pressure in geothermal fields. *Geophys. Res. Lett.*, **32**, L21317, doi:10.1029/2005GL023551.

Tryggvason, E., 1986. Multiple magma reservoirs in a rift zone volcano: Ground deformation and magma transport during the September 1984 eruption of Krafla, Iceland. *J. Volcanol. Geothermal Res.,* **28**, 1-44.

Vlahovic, G., Elkibbi, M., and Rial, J.A., 2002a. Shear-wave splitting and reservoir crack characterization: the Coso geothermal field. *J. Volcanol. Geothermal Res.*, **120**, 123-140.

Vlahovic, G., Elkibbi, M., and Rial, J.A., 2002b. Temporal variations of fracture directions and fracture densities in the Coso geothermal field from analyses of shear-wave splitting. *Proc. Geothermal Reservoir Engineering*, Stanford, **27**, 415-421.

Volti, T. and Crampin, S., 2003a. A four-year study of shear-wave splitting in Iceland: 1. Background and preliminary analysis. In *New insights into structural interpretation and modeling*, ed. Nieuwland, D. A., Geol. Soc. Lond., Spec. Publ., **212**, 117-133.

Volti, T. and Crampin, S., 2003b. A four-year study of shear-wave splitting in Iceland: 2. Temporal changes before earthquakes and volcanic eruptions. In *New insights into structural interpretation and modeling*, ed. Nieuwland, D. A., Geol. Soc. Lond., Spec. Publ., **212**, 135-149.

Yang, M., 2003. *Inversion of shear-wave splitting data in geothermal reservoirs*, Master's thesis. University of North Carolina, Chapel Hill, NC.

Yang, M., Elkibbi, M., and Rial, J.A., 2003. Modeling of 3D crack attributes and crack densities in geothermal reservoirs. *Proc. Geothermal Reservoir Engineering*, Stanford, **28**, 321-327.

Yang, M., Elkibbi, M., and Rial, J.A., 2005. An inversion scheme to model subsurface fracture systems using shear wave splitting polarization and delay time observations simultaneously. *Geophys. J. Int.*, **160**, 939-947.

Table 3.1. Inversion results of crack parameters from Krafla SWS measurements.

Station ID	Crack Strike (Degree)	Crack Dip (Degree)	Crack Density	Goodness of Fit (%)
P03	-36	27	0.057	57.32
P04	-54	65	0.028	66.22
P06	-73	-22	0.084	62.73
P10	5	-73	0.027	60.87
P11	-60	33	0.083	65.64
P13	-55	80	0.024	64.12
P14	36	-68	0.030	61.46
P15	-88	61	0.030	74.01
P16	79	58	0.045	67.61
P23	-73	-74	0.027	85.31

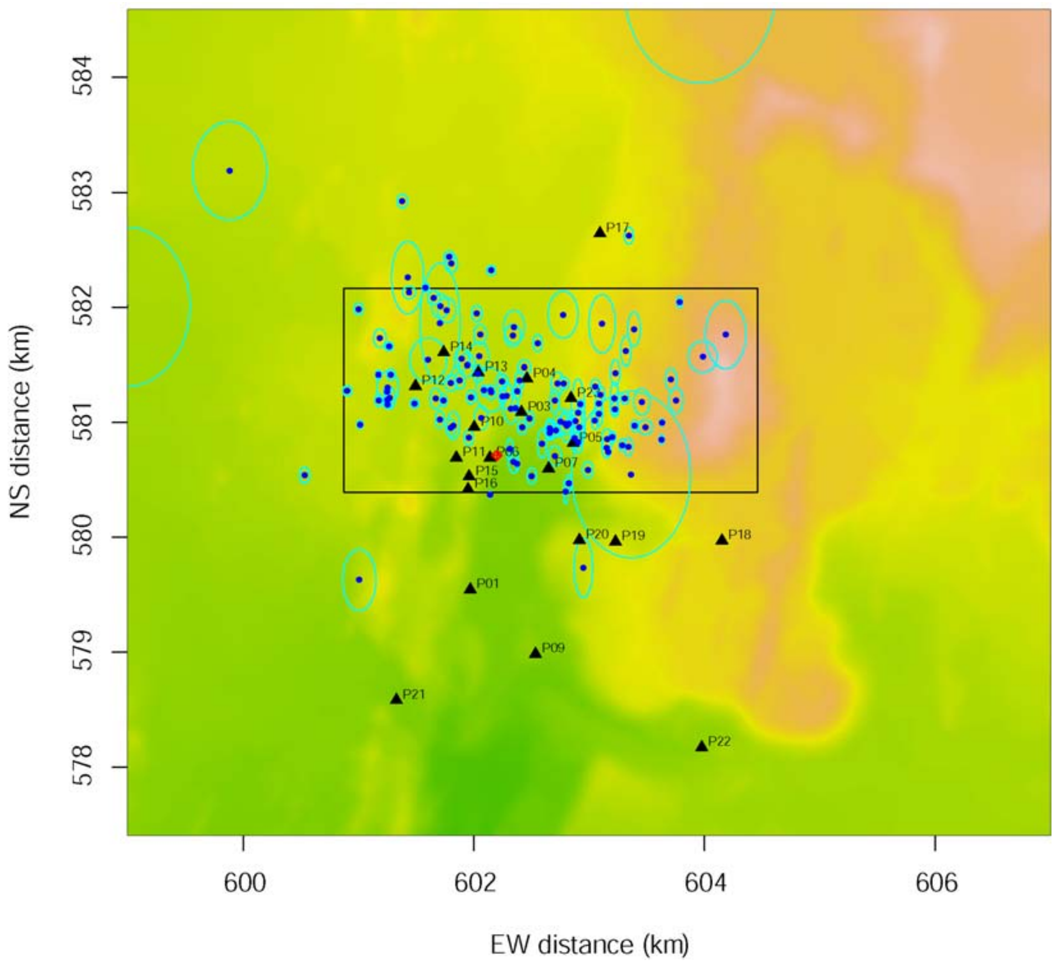

(a)

Figure 3.1. Microseismicity recorded by the UNC array at Krafla. A total of 129 earthquakes were located during the period from July 5th to August 11th. The seismic stations are represented by solid triangles and the red diamond shows the location of injection well K-26. The ellipses indicate the location error associated with each epicenter. The error in the E-W direction is generally smaller than the N-S direction. The focal depth distribution of the earthquakes located around the injection well K-26 (inside the rectangle in (a)) is shown in (b). Vertical line segments indicate calculated error in focal depth.

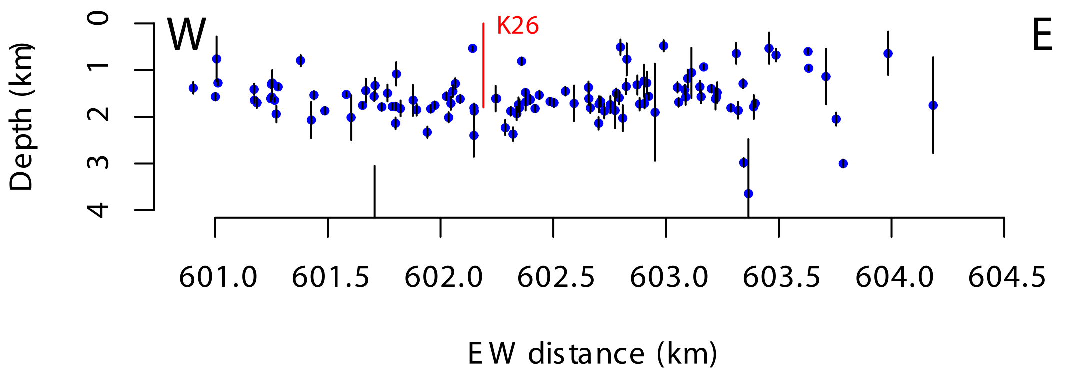
W
E
K26
Depth (km)
0
1
2
3
4
601.0
601.5
602.0
602.5
603.0
603.5
604.0
604.5
EW distance (km)

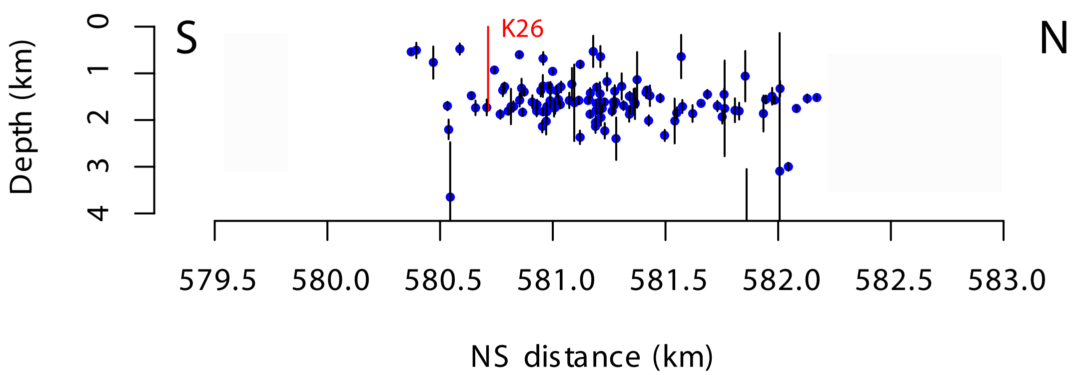
S
N
K26
Depth (km)
0
1
2
3
4
579.5
580.0
580.5
581.0
581.5
582.0
582.5
583.0
NS distance (km)

Figure 3.1(b).

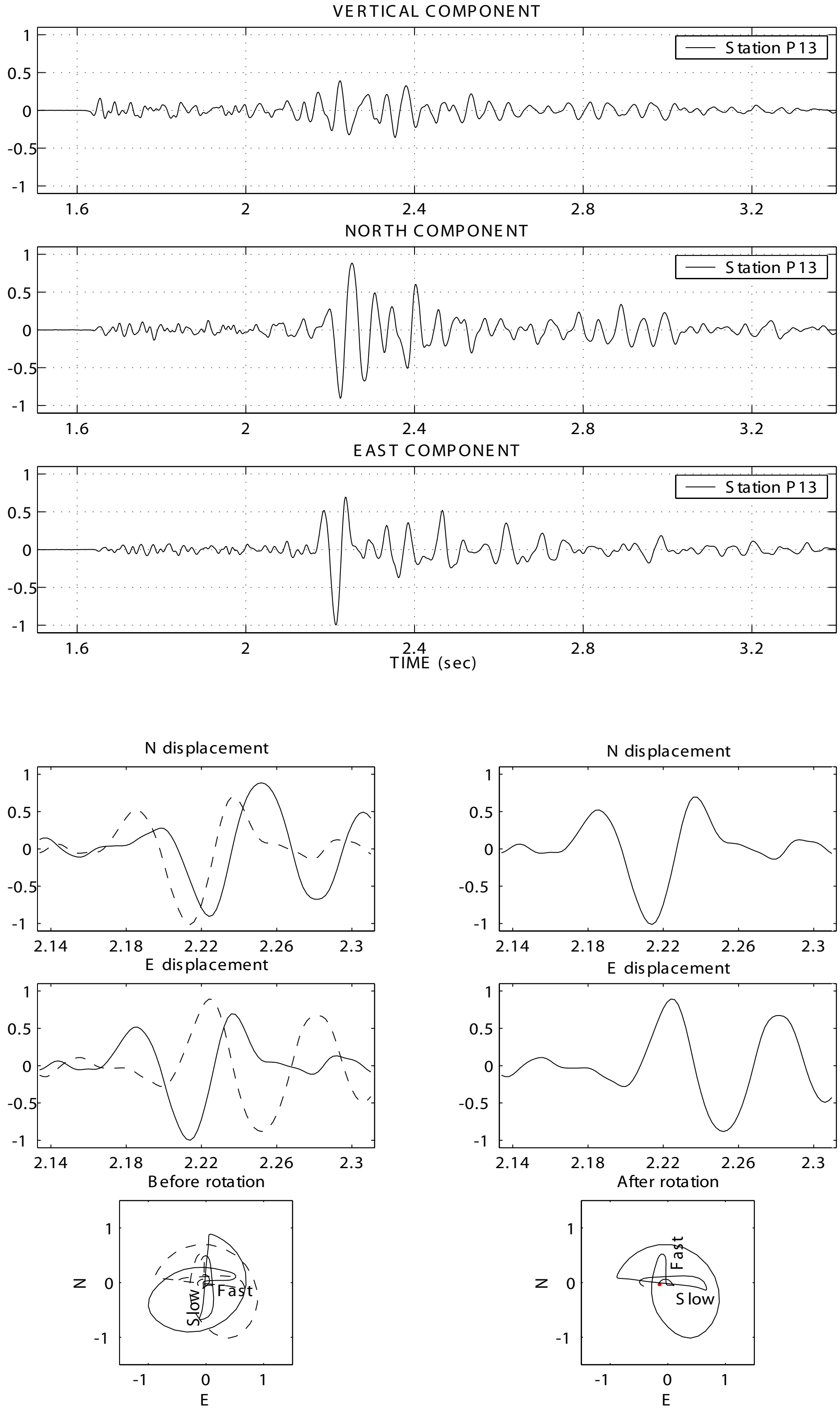
VERTICAL COMPONENT
Station P13
NORTH COMPONENT
Station P13
EAST COMPONENT
Station P13
TIME (sec)
N displacement
E displacement
Before rotation
Slow
Fast
N
E
N displacement
E displacement
After rotation
Fast
Slow
N
E

Figure 3.2(a).

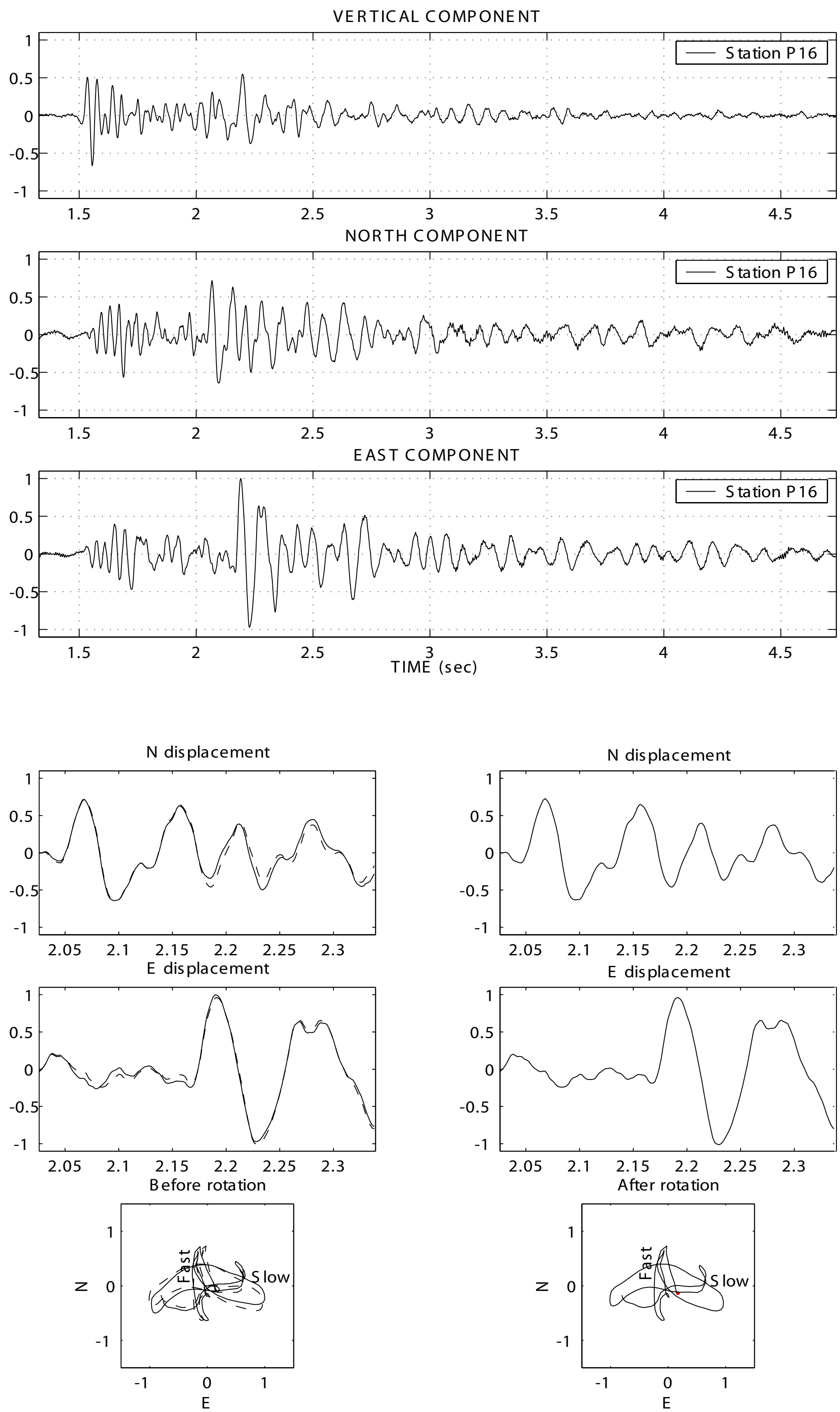
VERTICAL COMPONENT
Station P16
NORTH COMPONENT
Station P16
EAST COMPONENT
Station P16
TIME (sec)
N displacement
E displacement
Before rotation
N displacement
E displacement
After rotation
Fast
Slow
N
E

Figure 3.2(b).

Figure 3.2. Two examples of shear-wave splitting recorded at Krafla. (a) Seismograms of the event 20040707221140, recorded at station P13. The seismograms are rotated 88° counterclockwise from the apparent eastern direction so that the horizontal particle motion plot shows that fast and slow shear-waves are oriented along the instrument's horizontal components. After rotation the direction of fast shear-wave is toward the north. Rotated seismograms and particle motion are represented by a dashed line in the left panel and plotted again in the right panel with solid line. The time delay is 86 ms in this example. (b) Seismograms of the event 20040707101006, recorded at station P16. The seismograms are rotated 8° clockwise from the apparent eastern direction. The time delay is 130 ms in this example.

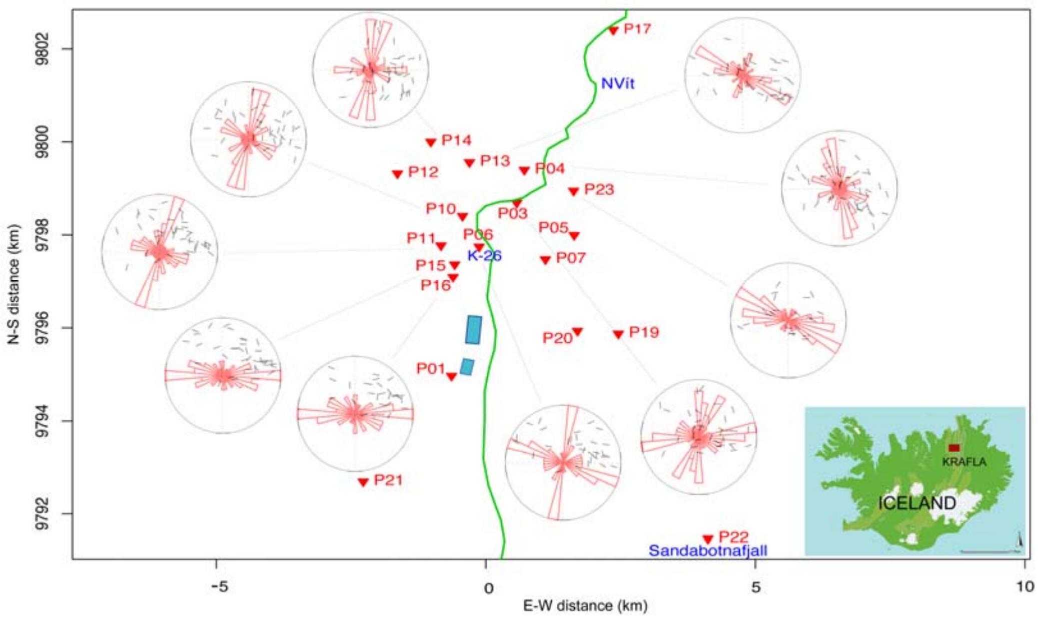

Figure 3.3. Equal-area rose diagrams (polar histograms) of the fast shear-wave polarization directions observed at ten seismic stations. The green curve represents the road and the blue squares indicate the location of the Krafla power plant. NVit is a crater nearby. See details in the text.

Figure 3.4. Fast shear-wave polarizations (a) and time delays (b) observed at station P13 and plotted in equal-area projection. The biggest circle corresponds to a time delay of 34 ms/km and the smallest to 1 ms/km. The shear-wave window is 35.2°. (c) The fitting between the observed and theoretical fast shear-wave polarizations for station P13. The red line segments are observed and blue ones are theoretical.

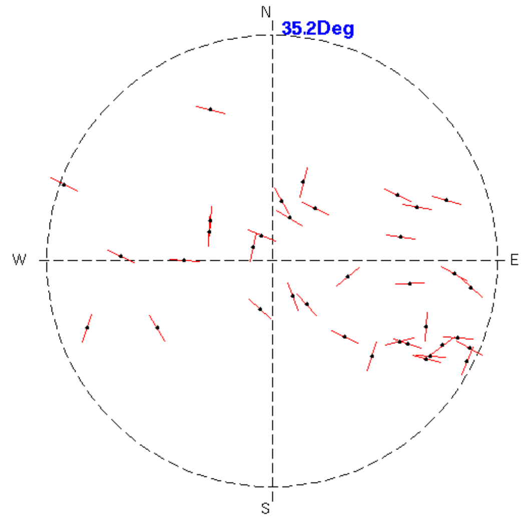

(a)

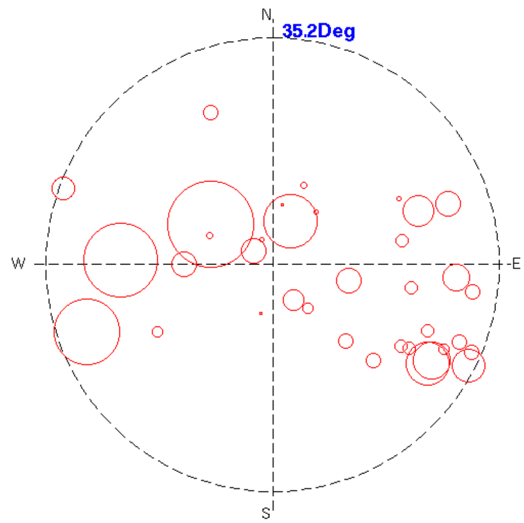

(b)

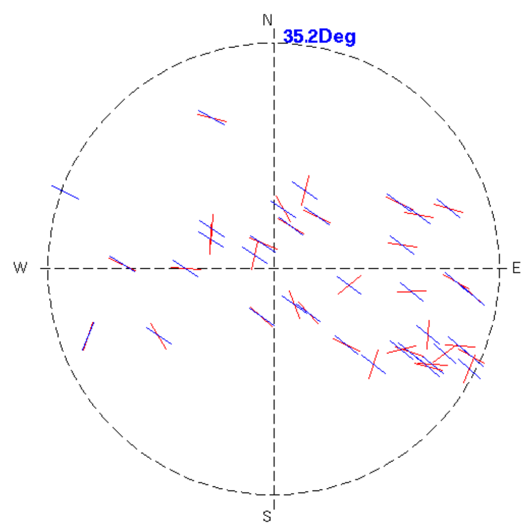

(c)

Figure 3.4.

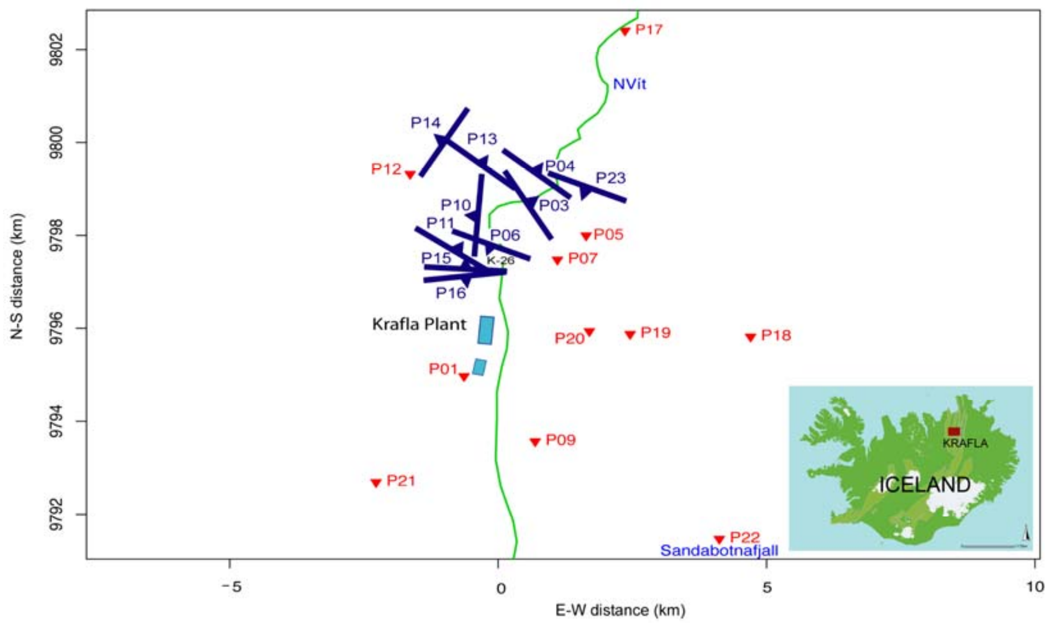

Figure 3.5. Illustration of inversion results for crack strikes and dipping directions at the ten stations. Crack strikes are represented by solid line segments and dipping directions by solid arrows.

Figure 3.6. Residual contours computed for stations P13 and P23 to invert for the crack strike, dip and density. (a) The global minimum of polarization residual for P13 (40.46) is located at strike = -55° and dip = 80° (actually shown on the plot is the complement dip = -10°). (b) The corresponding time delay residual for P13 is 8.95, while the global minimum of time delay residual (7.98) is located somewhere else. (c) The global minimum of polarization residual for station P23 (28.15) is located at strike = -73° and dip = -74°. (d) The global minimum of time delay residual for P23 (5.95) is located at the same pair of strike and dip as in (c).

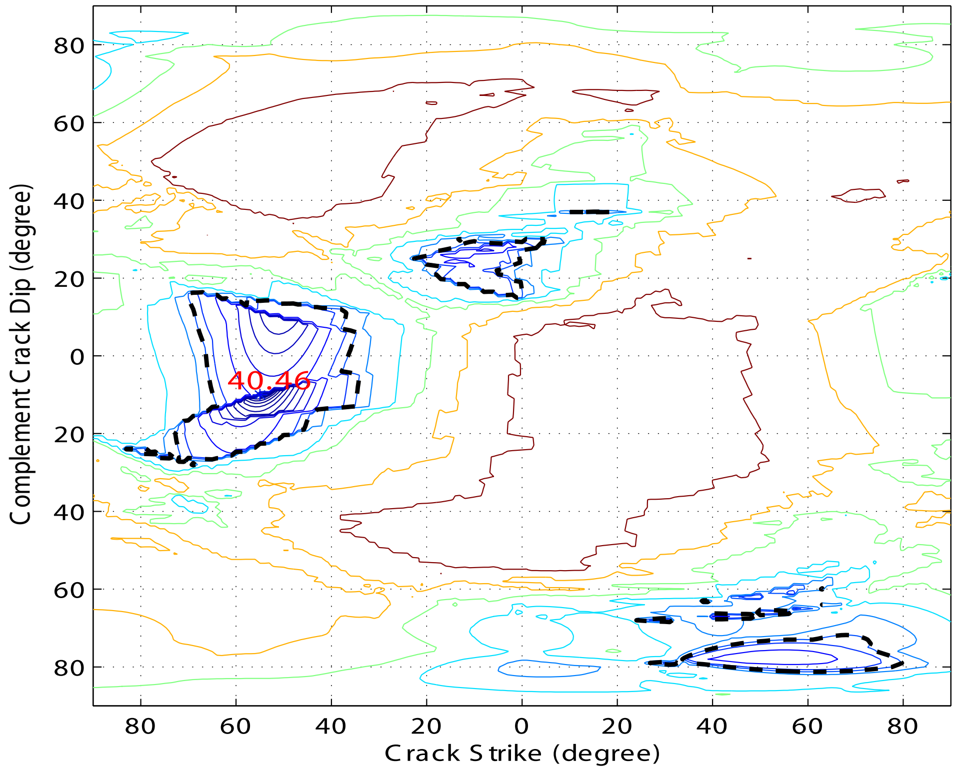

(a)

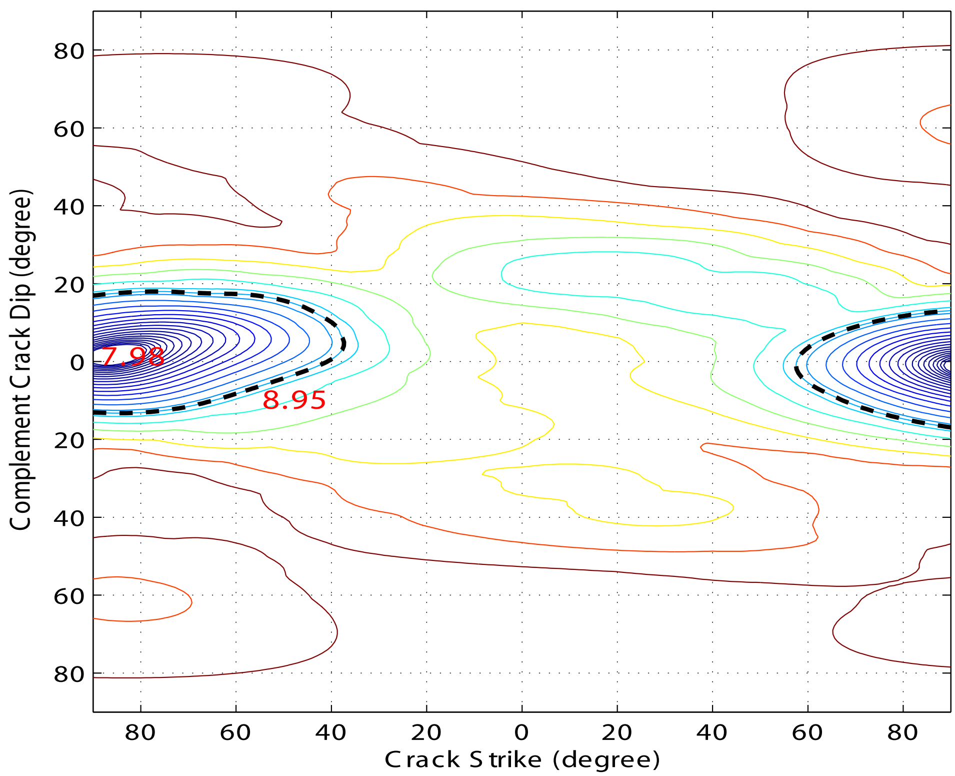

(b)

Figure 3.6(a)(b).

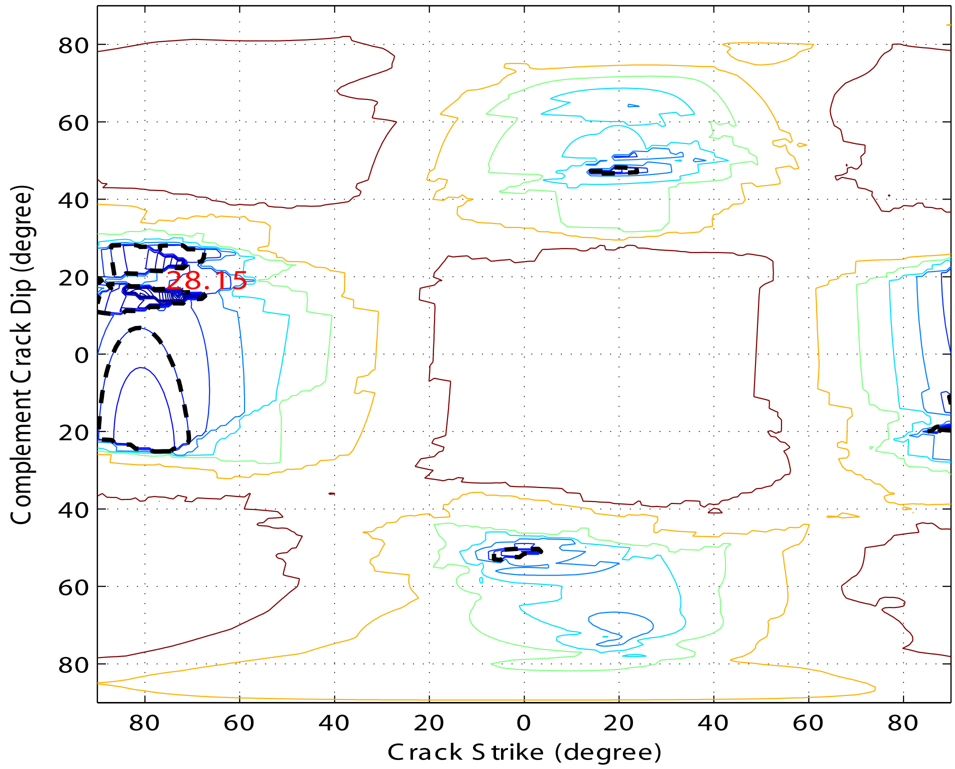

(c)

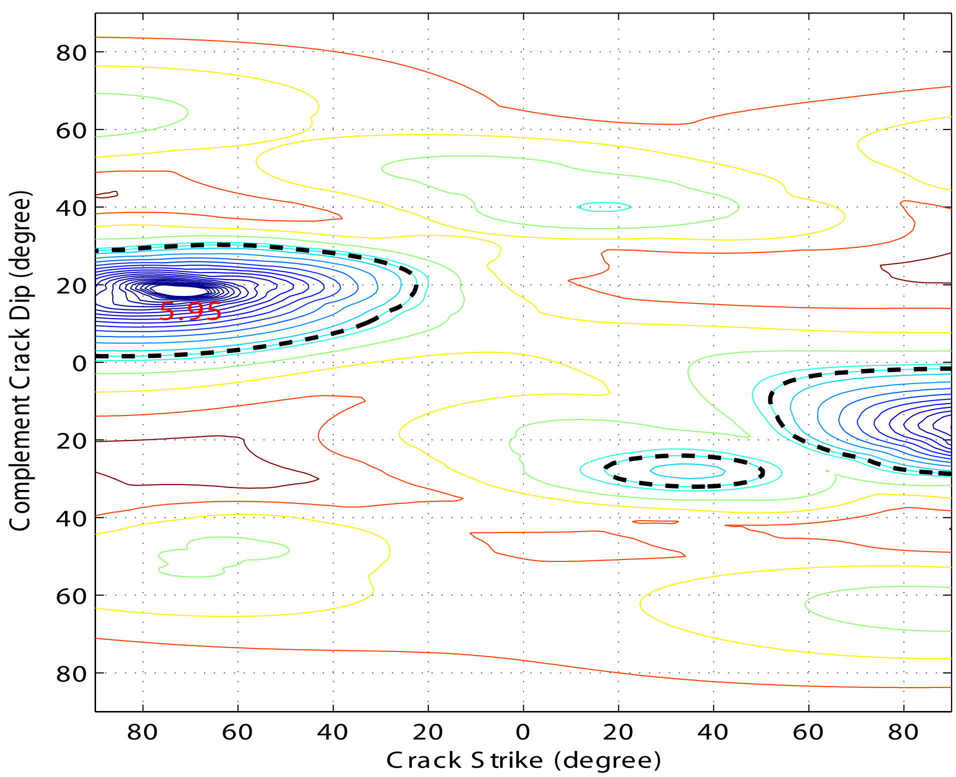

(d)

Figure 3.6(c)(d).

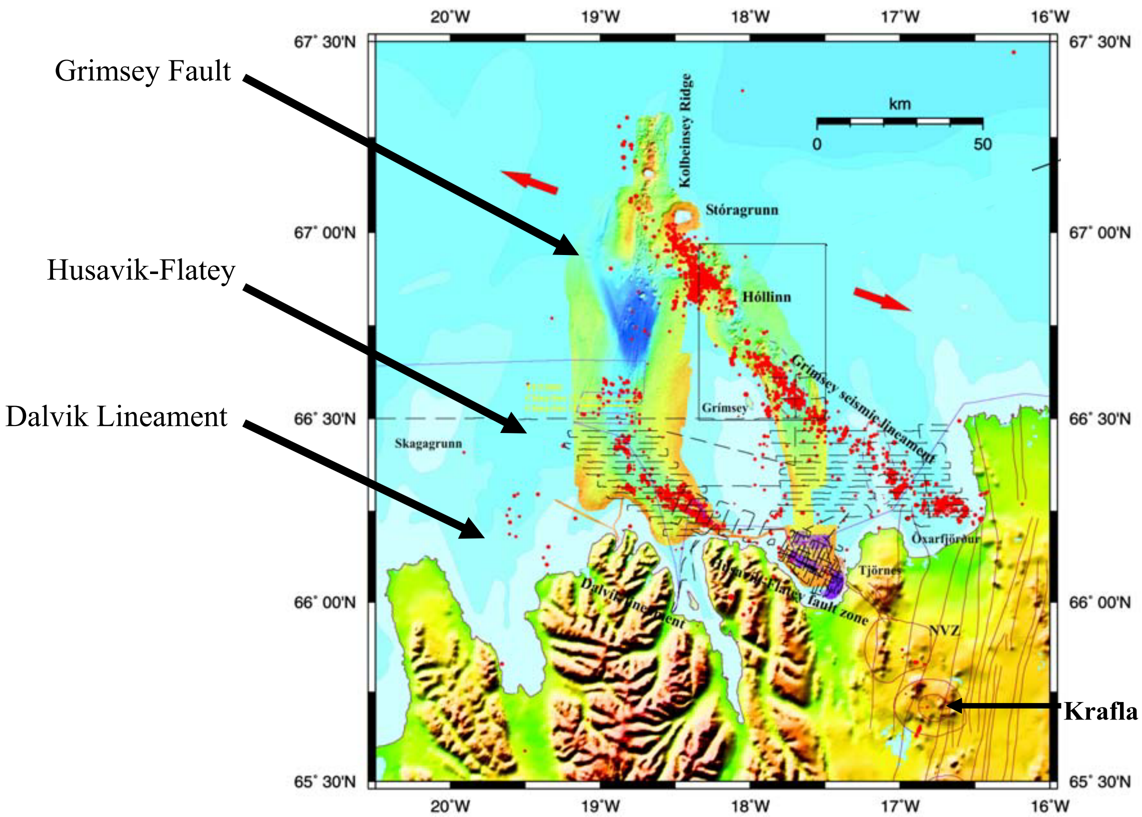

Figure 3.7. Topographic view of the northernmost part of Iceland and major NW-SE oriented geological lineaments to the north. Red dots represent epicenters of historical earthquakes and solid red arrows show the moving direction of divergent plates. (source: http://hraun.vedur.is/ja/)

CHAPTER IV

OBSERVATIONS AND ANALYSES OF SHEAR-WAVE SPLITTING IN THE GEOTHERMAL FIELD AT HENGILL, ICELAND

Shear-wave splitting Observations and Inversion for Fracture Parameters

Introduction

Iceland is situated on top of the Mid-Atlantic Ridge where the ridge interacts with the Iceland Hot Spot. Several volcanic centers, active and extinct, are located within the island. One of them is the Hengill volcanic center which lies on the plate boundary between the North America and the European crustal plates in Southwestern Iceland. The rifting of the two plates has opened a NNE trending system of normal faults with frequent magma intrusions. The Hengill central volcano and its transecting fissure swarm, extending 70 — 80 km long from the coast south of Hengill to north of Lake Thingvallavatn with an associated graben structure, form the Hengill volcanic system. The Hengill central volcano is currently active and is the main volcanic production focus of the area associated with a high-temperature geothermal field. In Nesjavellir, in the northern part of the Hengill area, a 400 MW geothermal power plant has been in operation since 1987. Another active but less pronounced volcanic system, the Hrómundartindur volcanic system, lies at the eastern edge of the Hengill system, outside the Hengill fissure swarm. The area near Mount Hrómun-dartindur can be classified as the central volcano of this system; it is a separate focus of volcanic production with high geothermal activity.

During the months of July and August in 2005, a 21-station, 3-component seismic array was deployed to the south of the Hengill central volcano, covering an area of approximately 5 km in N-S and 10 km in E-W. The array was divided into two parts: the Western part including twelve stations numbering from H30 to H41, and the Eastern part with nine stations numbering from H70 to H78. The distribution of these stations is depicted in Figure 4.1. Also shown in Figure 4.1 are the epicenters of historical earthquakes occurring in this area between January 1995 and May 2005 which are retrieved from the online earthquake catalogues provided by the Icelandic Meteorological Office on a weekly basis in their web site (http://hraun.vedur.is/ja/viku/****/vika_#/hen.gif where **** are years and # are week numbers). Between July 2nd and August 12th the array continuously recorded the seismic activity in the study area for forty-two days. Each station in the seismic array consisted of a three-component short-period MARK4 L28 (4 Hz) seismic sensor, a data-logger or DAS (Data Acquisition System), a GPS antenna, and a 12V car battery. The data were collected continuously at a sampling rate of 500 samples per second. The data recorded have been processed and analyzed to locate microearthquakes occurring in this area during the deployment and detailed analysis of shear-wave splitting have been performed as will be presented in the following sections.

Seismicity and Shear-wave Splitting Measurements

The variations in the daily number of seismic events detected by the array are showed in Figure 4.2. During the forty-two days of operation the array detected an average of 3 to 4 well-recorded events per day (observed at 5 or more stations). These are very small earthquakes with magnitudes probably no greater than 2. Figure 4.3(a) shows the epicenters of the earthquakes located inside and in the vicinity of the array from July 5th to August 12th along with the location errors plotted, and Figure 4.3(b) shows the depth distribution of a little more earthquakes along E-W and N-S cross-sections respectively. The velocity model used in the location program is from adopted from Tryggvason et al. (2002) and both P- and S-arrivals are used to provide sufficient constraints on the earthquake locations. It is apparent that most events occurred in the eastern part and were somewhat clustered around stations H71, H72 and H73. Over 90 percent of the focal depths are shallower than 6 km, which is consistent with the estimate of the depth to the base of the brittle crust in this area (Tryggvason et al., 2002). Also note the gap of earthquakes between the depth range 6-10 km beneath the center of the Hrómundartindur volcanic system which agrees with the probable presence of a still-molten part of a mostly solidified magma chamber (Sigmundsson et al., 1997).

Shear-wave splitting is an exploration method of proven reliability and unique imaging power. The method is based on the fact that a shear-wave propagating through rocks with stress-aligned micro-cracks will split into two waves, a fast one polarized parallel to the predominant crack direction, and a slow one polarized perpendicular to it (Crampin, 1981, 1984; Babuska and Cara, 1991). Two important parameters are associated with a shear-wave splitting event: the polarization direction of the fast shear wave (φ), and the differential time delay between the arrivals of the fast and slow shear waves (δt). Measuring the fast-shear wave polarization and time delay from local microearthquakes has become a valuable technique to detect the orientation and intensity of fracturing in the subsurface of fracture-controlled geothermal fields (e.g. Lou and Rial, 1997; Vlahovic et al., 2002a, 2002b; Elkibbi and Rial, 2003, 2005; Elkibbi et al., 2004, 2005; Yang et al., 2003, 2005; Rial et al., 2005; Tang et al., 2005a, 2005b, 2008).

Shear-wave splitting is clearly recorded in the seismic data from Hengill geothermal area. In fact, we have recorded well developed splitting that clearly shows the prevalence of a dominate crack system oriented NNE-SSW in perfect agreement with the orientation of local fissure systems. An example of shear-wave splitting in the data set is showed in Figure 4.5. Fast shear-wave polarization angle φ is measured by interactive rotation of the seismogram until the horizontal particle motion plot shows that fast and slow shear-waves are oriented along the instrument's horizontal components (refer to the bottom half in Figure 4.5). The angle of rotation from the original polarization direction determines φ. Meanwhile the two shear-wave arrivals, which are often coupled in the original recording, separate out in time domain and δt can then be directly measured. In this study δt is normalized by dividing it by the length of the ray path in order to correctly compare delays from different paths.

So far the data from seven selected stations in the eastern part of the array (H70—H76) have been investigated to measure the fast shear-wave polarization and delay time. These stations are selected to ensure that most of the earthquakes fall into the shear-wave window, typically a right circular cone with vertex at the station and vertex angle equal to 35°, of the stations. Figure 4.5 is showing the equal-area rose diagrams (polar histograms) of fast shear-wave polarization directions observed within the shear-wave window of the seven stations. It can be clearly seen from Figure 4.5 that the predominant polarization directions observed at stations H71, H72 and H75 are consistently pointing to a NNE-SSW orientation. H74 and H76 also display a major polarization in NNE-SSW, although there are still some cases showing an additional polarization nearly perpendicular to the major direction, which is possibly due to the rough topography around these stations. H70 shows a similar but even worse pattern with two perpendicular polarization directions of almost equal strength, most probably accounted for by the fact that almost all the events within the shear-wave window of station H70 are far to the north (see also this station in Figure 4.6). Finally, H73 shows a completely different dominant direction of polarization in NWW-SEE which is perpendicular to the ones displayed at H71, H72 and H75. This might suggest the existence of a conjugate fault system associated with the main NNE-SSW fissure system.

To inspect the azimuthal distribution of polarization angles, equal-area projection plots of the observed polarizations at all the seven selected stations are shown in Figure 4.6. For most of the stations, the shear-wave splitting events within the shear-wave window come basically from all of the four quadrants which can also be compared with the distribution of located epicenters in Figure 4.3(a). The only exception is H70 where all associated earthquakes are projected onto the northern hemisphere since it is far to the south of most earthquake epicenters. Also note that at H72 the observed polarizations projected on the western hemisphere are generally slightly different from those on the eastern hemisphere although sharing the common NNE-SSW orientations, suggesting two unique systems of cracks with slightly different strikes near to the west and to the east of station H72 respectively.

Inversion for Crack Geometry and Intensity

We use an inversion scheme employing both shear-wave splitting parameters φ and

δt (Yang et al., 2003, 2005). As has been extensively discussed in many previous studies, φ mainly depends on the angle between the crack normal and the seismic ray while δt is proportional to the crack density along the ray path. Essentially, inversion efforts are expected to identify regions of different crack densities in Hengill geothermal field and to invert for 3-D fracture geometry in the subsurface. Based on seismic ray coverage and depending on the spatial patterns and azimuthal distributions of observed polarizations and time delays in the equal-area projection plots, crack-induced anisotropy in Hengill geothermal area is mainly modeled by a single system of vertical cracks, since most of the stations we have analyzed have showed just one chief polarization direction (see Figure 4.5). The recording of a single prevalent polarization may in general be accounted for by anisotropic effects due to parallel vertical cracks. In this case, the chief polarization orientation is parallel to the strike of the dominating crack system in the neighborhood of the station.

The inversion results for crack strike, crack dip, and crack density using the measured fast shear-wave polarization directions and differential time delays from the seven selected seismic stations in Hengill geothermal field are briefly listed in Table 1 and graphically illustrated in Figure 4.7. The data from stations H71, H72, H75 and H76 are overall of better quality than the other stations and hence the higher goodness of fit statistics in the estimate of inverted fracture properties. The results at H71, H72, H75 and H76 are generally consistent with the assumption of the single set model in terms of their nearly vertical dipping angles and relatively low crack densities. The results of crack strikes are also in good agreement with the general NNE-SSW orientation of the local fissure system. The crack strikes at H70 and H74 are more close to NEE-SWW and the dipping angles are more biased from vertical with a much higher crack density compared with the previous four stations. The results at H70 are even worse probably due to its far distance from the epicenters of the earthquakes. The inverted crack strike at H73 is nearly perpendicular to the dominant strikes of all other stations while the dipping angle is also somewhat biased from vertical.

Conclusions

A 21-station, 3-component digital seismic array was deployed near the Hengill geothermal field in Southwestern Iceland in July and August of 2005. The seismic data set we have collected there is sampled at 500 sps which is high enough to allow detection of even the smallest variations in crack geometry and density. The seismicity in Hengill during the period of deployment of the array was not very high (3-4 usable events per day on average), with most epicenters clustered within the eastern part of the array. Over 90 percent of the focal depths are shallower than 6 km suggesting an approximate depth of 6 km to the base of brittle crust.

There is clear evidence of shear-wave splitting in the seismic data set. The observed prevalence of a crack system oriented in NNE-SSW is consistent with the anticipated direction of major fractures in the area. Shear-wave splitting parameters are measured and inverted for fracture properties in the vicinity of each recording station. For most stations the inversion results for fracture direction (strike) are in good agreement with the general NNE-SSW orientation of the local fissure system and with results from other previous investigations in the Hengill area. The inversion results for fracture inclination (dip) are consistent with nearly vertical dipping angles and of relatively low crack densities. The only exception occurs at H73 where the observed main polarization direction and the inverted crack strike are approximately perpendicular to those of all other stations, which may indicate the orientation of local fractures formed by the shear faulting across the divergent plate boundary within the near-surface part of the crust.

Focal Mechanism Solutions and Waveform Simulation

Focal Mechanism Solutions

In previous sections we have described the results of shear wave splitting measurements on microearthquakes recorded at Hengill geothermal field during the 2005 deployment and the inverted fracture attributes using these measurements. However, it has to be noted that the combination of low station density, low seismicity and short time of deployment limited the description of the wave field and its anisotropic characteristics at Hengill. Another possible way is to look at the focal mechanism solution of each earthquake in terms of fault plane parameters (strike, dip, rake) and compare with the measured fast wave polarization as well as inverted crack geometries (strike and dip). For this purpose forty seismic events of good recording quality from the Hengill dataset were selected for study and their epicenters are plotted in Figure 4.8(a).

Focal mechanism solutions were calculated for all selected earthquakes based on the distribution of polarity of P arrivals at all available stations using an R-based code provided by Dr. Jonathan Lees of UNC-Chapel Hill. The best focal mechanism solution of each selected earthquake is listed in Table 2 and graphically illustrated in Figure 4.8(b).

Out of the forty best focal mechanism solutions of the selected earthquakes about three fourths (31) of the strikes are oriented closer to N-S which is consistent with the shear-wave splitting inversion results at stations H71, H72, H75 and H76 where best quality data were recorded. The remaining one fourth of the strikes (closer to E-W orientation) also agrees with the inversion results at stations H70 and H73. Thus, the orientation of the crack systems in Hengill obtained from both the shear-wave splitting analysis and focal mechanism solutions are in fairly good agreement with a predominant fracture system oriented approximately NNE-SSW that is also consistent with the regional tectonic structure in the Southwestern Iceland as well as the results from other previous investigations in this area (e.g. Arnason, personal communication). As for the dip angle, most fault planes (29 out of 40) are steep (≥45º) which is also consistent with the inversion results as described in previous sections of this chapter. This also further validates the assumption of inversion that the cracks are nearly vertical. It should still be noted however that many of the focal mechanism solutions are not well constrained, but it is possible to further adjust the fault plane parameters of these earthquakes using the full-wave synthetic seismograms.

Waveform Simulation Using an Isotropic Solver

Due to the scarcity of seismic data and low station density a standard P-wave polarization approach may produce highly unconstrained focal mechanism solutions. To better constrain the solutions we can use a 3-D seismic wave propagation solver that constructs full-wave synthetic seismograms for a given focal mechanism.

Three-component synthetic seismograms of the forty selected mircoearthquakes were computed at the location of six stations (H71 to H76) using the seismic source descriptions equivalent to the estimated fault plane solutions by a 3-D isotropic elastic wave propagation solver freely distributed by the Laurence Berkeley National Laboratory. In the synthetic seismograms we obtained P-wave arrival times and polarities that are satisfactorily matched with real data, and also a generally good agreement between S-wave arrival times. Since the computation assumes an isotropic medium the comparison between the observed and computed seismograms may provide a qualitative measure of the intensity of anisotropy in the vicinity of each station. Comparison plots of real data and synthetic seismograms for ten selected earthquakes at selected stations are shown in Figure 4.9. As a summary the location and detailed fault plane mechanism of all forty selected earthquakes are included in Figure 4.10.

The three-component waveform simulation was used not only to confirm the P-wave focal mechanism for each earthquake but also to possibly assess 3-D variations in seismic wave velocity and the effect of seismic anisotropy on the S-wave polarization. The study may be continued through working on the simulation of these selected earthquakes by incorporating the effect of crack-induced anisotropy determined in previous sections into the wave propagation solver. One can attempt the full-wave simulation of some of the best-recorded events, which may allow to further refine the direction and density of cracks in the area.

References

Babuska, V., and Cara, M., 1991. *Seismic Anisotropy in the Earth*, Modern Approaches in Geophysics, Vol. 10, pp. 217, Kluwer Academic Publishers, The Netherlands.

Crampin, S., 1981. A review of wave motion in anisotropic and cracked elastic media, *Wave Motion*, **3***,* 343-391.

Crampin, S., 1984. An introduction to wave propagation in anisotropic media, *Geophys. J. Roy. Astr. Soc.,* **76***,* 17-28.

Elkibbi, M., and Rial, J.A., 2003. Shear-wave splitting: an efficient tool to detect 3D fracture patterns at The Geysers, California, *Proc. Geothermal Reservoir Engineering*, Stanford, **28***,* 143-149.

Elkibbi, M., Yang, M., and Rial, J.A., 2004. Imaging crack systems in The Geysers with shear-wave splitting, *Geothermal Resources Council (GRC) Transactions*, **28**, 789-800.

Elkibbi, M., Yang, M., and Rial, J.A., 2005. Crack-induced anisotropy models in The Geysers geothermal field, *Geophys. J. Int.*, **162**, 1036-1048.

Elkibbi, M., and Rial, J.A., 2005. The Geysers geothermal field: results from shear-wave splitting analysis in a fractured reservoir, *Geophys. J. Int.*, **162**, 1024-1035.

Lou, M., and Rial, J.A., 1997. Characterization of geothermal reservoir crack patterns using shear-wave splitting, *Geophysics*, **62***,* 487-495.

Rial, J.A., Elkibbi, M., and Yang, M., 2005. Shear-wave splitting as a tool for the characterization of geothermal fractured reservoirs: lessons learned, *Geothermics*, **34**, 365-385.

Sigmundsson, F., Einarsson, P., Rognvaldsson, Th.S., Foulger, G.R., Hodgkinson, K.M., and Thorbergsson, G., 1997. The 1994-1995 seismicity and deformation at the Hengill triple junction, Iceland: Triggering of earthquakes by minor magma injection in a zone of horizontal shear stress, *J. Geophys. Res.,* **102***:B7*, 15151-15161.

Tang, C., Rial, J.A., Lees, J. M., and Thompson, E., 2005a. Seismic Imaging of the Geothermal Field at Krafla, Iceland, *Proc. Geothermal Reservoir Engineering*, Stanford, **30***,* 464-471.

Tang, C., Rial, J. A., and Lees, J. M., 2005b. Shear-wave splitting: A diagnostic tool to monitor fluid pressure in geothermal fields, *Geophys. Res. Lett.*, **32**, L21317, doi:10.1029/2005GL023551.

Tang, C., Rial, J. A., and Lees, J. M., 2008. Seismic Imaging of the Geothermal Field at

Krafla, Iceland Using Shear-wave Splitting, *J. Volcanol. Geothermal Res.,* **176(2)**, 315-324, doi:10.1016/j.jvolgeores.2008.04.017.

Tryggvason, A., Rognvaldsson, Th.S., and Flovenz, O.G., 2002. Three-dimensional imaging of the P- and S-wave velocity structure and earthquake locations beneath Southwest Iceland, *Geophys. J. Int.*, **151**, 848-866.

Vlahovic, G., Elkibbi, M., and Rial, J.A., 2002a. Shear-wave splitting and reservoir crack characterization: the Coso geothermal field, *J. Volcanol. Geothermal Res.*, **120**, 123-140.

Vlahovic, G., Elkibbi, M., and Rial, J.A., 2002b. Temporal variations of fracture directions and fracture densities in the Coso geothermal field from analyses of shear-wave splitting, *Proc. Geothermal Reservoir Engineering*, Stanford, **27**, 415-421.

Yang, M., Elkibbi, M., and Rial, J.A., 2003. Modeling of 3D crack attributes and crack densities in geothermal reservoirs, *Proc. Geothermal Reservoir Engineering*, Stanford, **28**, 321-327.

Yang, M., Elkibbi, M., and Rial, J.A., 2005. An inversion scheme to model subsurface fracture systems using shear wave splitting polarization and delay time observations simultaneously, *Geophys. J. Int.*, **160**, 939-947.

Table 4.1. Inversion results of crack parameters from Hengill SWS measurements.

Station ID	Crack Strike (Degree)	Crack Dip (Degree)	Crack Density	Goodness of Fit (%)
H70	72	-18	0.084	79.22
H71	27	89	0.048	93.79
H72	40	89	0.047	91.71
H73	-61	60	0.071	67.09
H74	54	63	0.077	65.19
H75	31	-87	0.043	81.34
H76	8	-89	0.033	84.33

Table 4.2. Computed focal mechanism of selected earthquakes in terms of fault parameters.

Earthquake ID	Strike (Degree)	Dip angle (Degree)	Slip angle (Degree)
2005070823394	145	70	99.8
2005071123574	-25	15	-110.3
2005071123583	200	80	-140.3
2005071707275	180	75	119.8
2005071809241	50	40	-140
2005071809492	35	70	-120.3
2005071811342	-20	75	90
2005071823083	-15	25	-149.7
2005072004592	15	65	-100.2
2005072109321	180	85	99.9
2005072109322	-10	5	90
2005072109410	45	25	149.7
2005072202262	-15	90	-110.0
2005072202272	15	65	119.9
2005072202355	170	5	70.1
2005072210201	145	85	40.2
2005072210254	-15	15	90
2005072219164	85	55	29.7
2005072222034	10	65	-170.2
2005072223145	150	45	-130.0
2005072300272	10	70	-99.8
2005072322380	-10	85	-99.9
2005072323340	10	75	129.8
2005072323480	65	55	40.3
2005072402130	195	5	90
2005072721395	45	55	19.9
2005072722584	150	75	-140.4
2005072802222	155	50	-39.4
2005072811593	80	55	80.1
2005072819422	-35	10	70.3
2005073020185	90	35	109.9
2005073100565	140	70	-39.8
2005073104014	-40	80	-150.4
2005080300011	115	50	119.8
2005080405095	145	90	168.0
2005080406044	155	65	-79.8
2005080516173	125	15	-130.1
2005080602574	155	75	-140.4
2005080602591	35	75	99.9
2005080808525	-5	90	-120.0

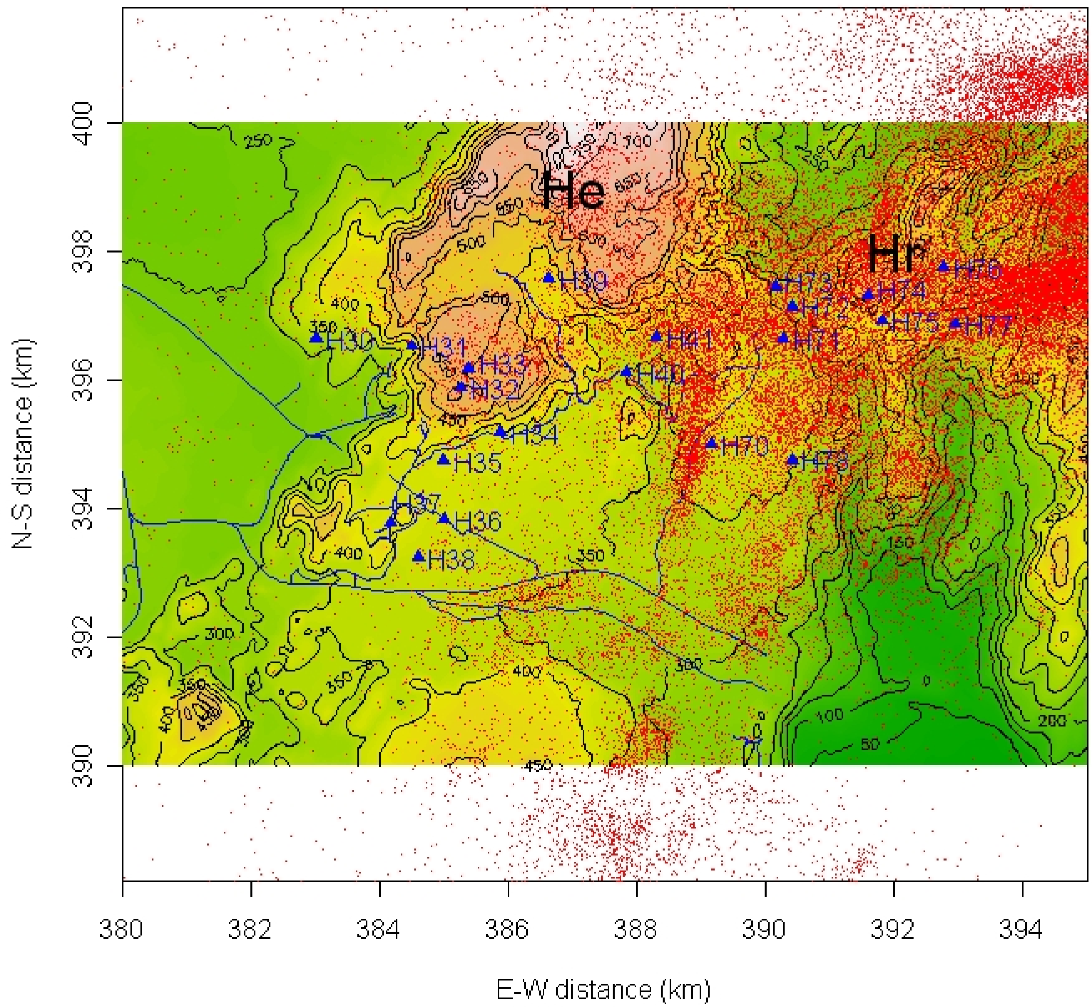

Figure 4.1.

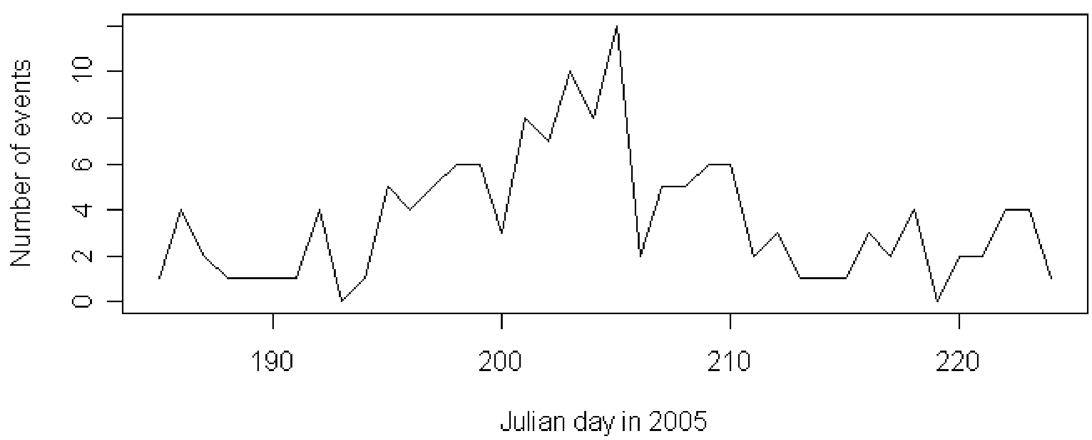

Figure 4.2.

Figure 4.1. Distribution of the stations of UNC-PASSCAL seismic array in Hengill geothermal field, Iceland. The red dots represent the locations of historical earthquakes from January 1995 to May 2005. 'He' indicates the Hengill central volcano and 'Hr' is the Mount Hrómundartindur.

Figure 4.2. Variation of daily number of seismic events detected by the array throughout the deployment.

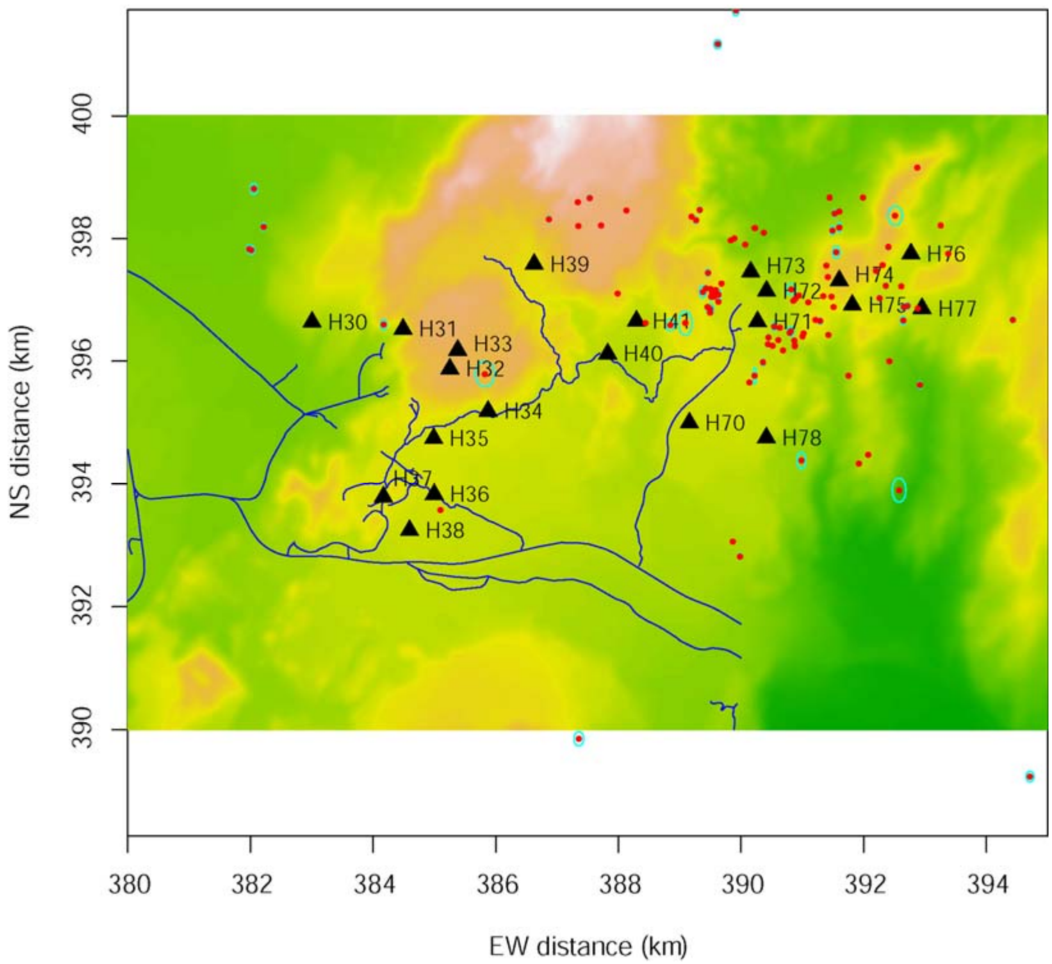

(a)

Figure 4.3. The seismicity recorded by the array from July 5th to August 12th, 2005 is shown in (a). Totally 146 events are detected and 130 events successfully located. The seismic stations are represented by solid triangles. The ellipses indicate the location error associated with each epicenter in NS and EW directions respectively. The errors in both EW and NS directions are generally small. The focal depth distribution of these seismic events is shown in (b). Vertical line segments indicate location error in focal depth.

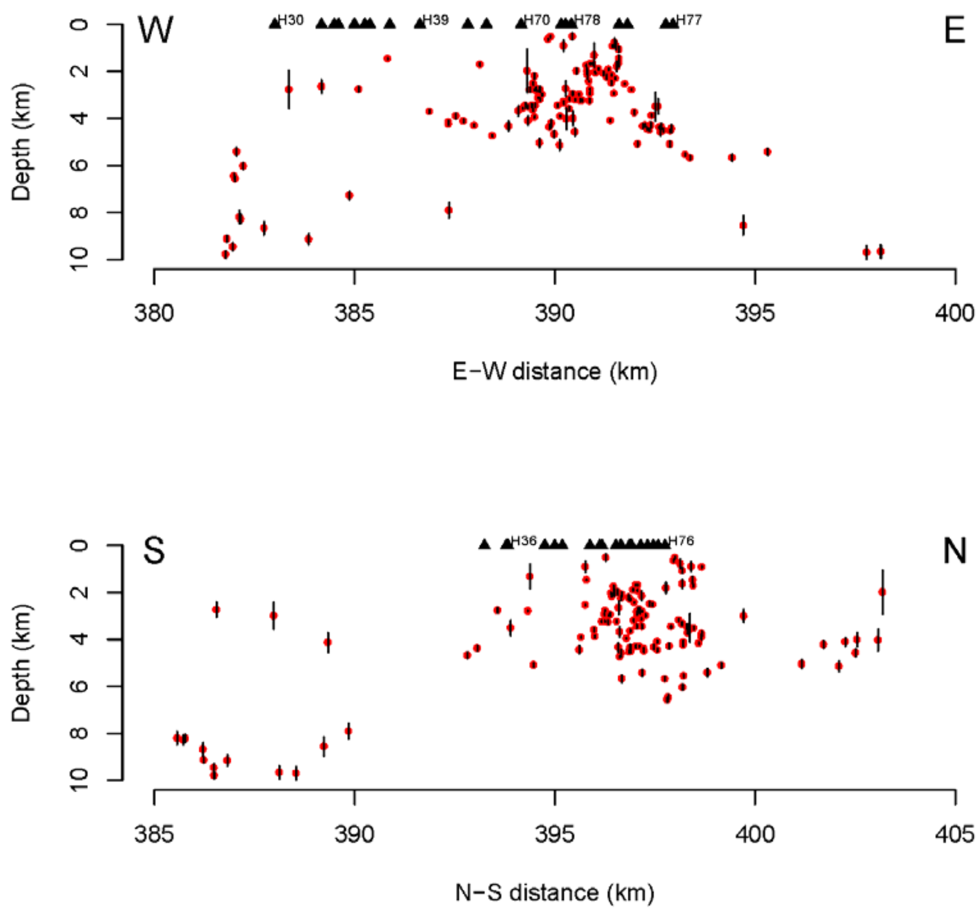
W
E
H30
H39
H70
H78
H77
Depth (km)
E−W distance (km)
S
N
H36
H76
Depth (km)
N−S distance (km)

Figure 4.3(b).

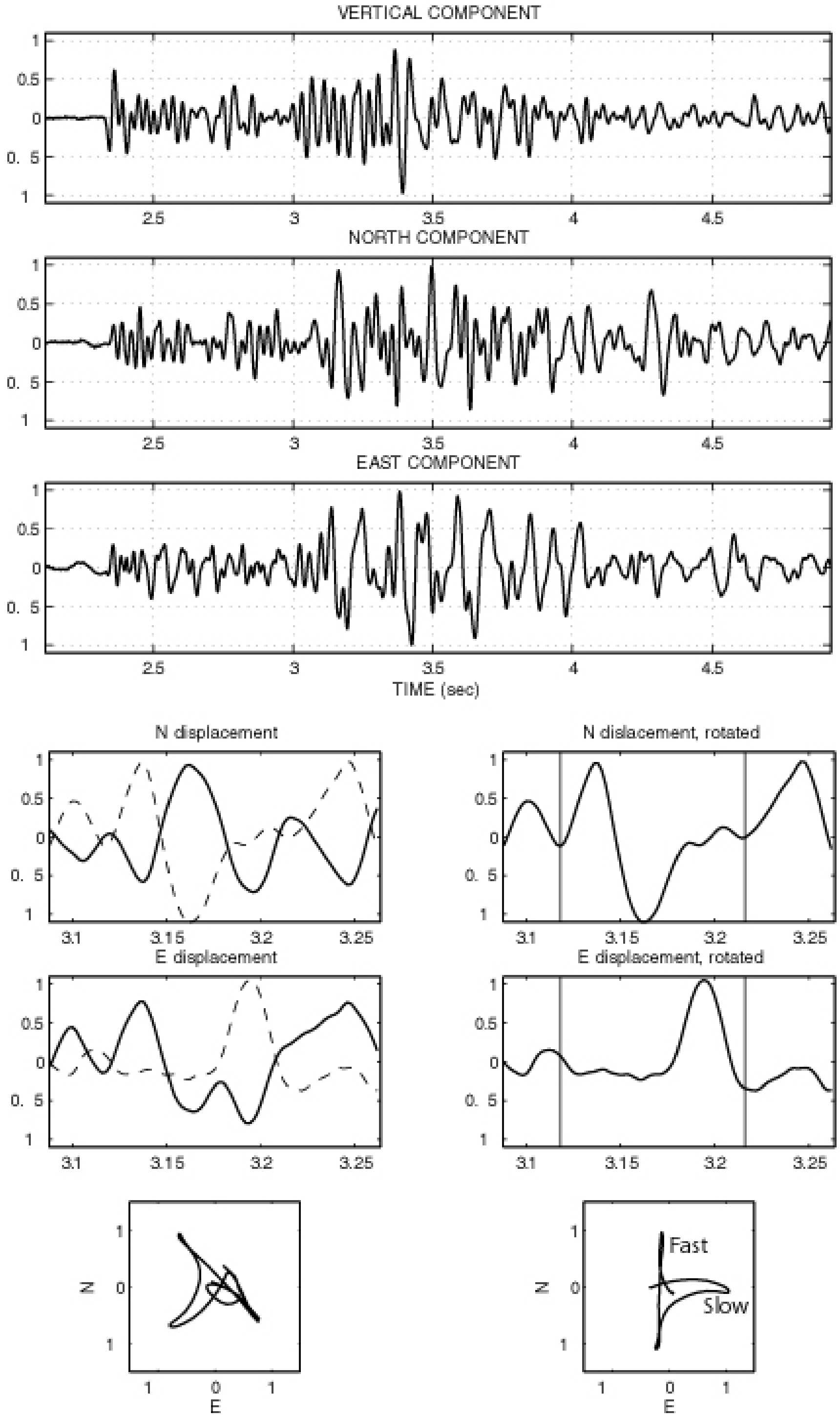
VERTICAL COMPONENT
NORTH COMPONENT
EAST COMPONENT
TIME (sec)
N displacement
N dislacement, rotated
E displacement
E displacement, rotated
N
E
Fast
Slow

Figure 4.4.

Figure 4.4. An example of shear-wave splitting in real seismogram. The event is identified as 200508060259 and recorded at H76. The seismograms are rotated 134° counterclockwise from the apparent eastern direction so that the horizontal particle motion plot shows that fast and slow shear-waves are oriented along the instrument's horizontal components. After rotation the direction of fast shear-wave is toward the north. Rotated seismogram is represented by a dashed line in the left panel and plotted again in the right panel with solid line. The time delay is 56 ms in this example.

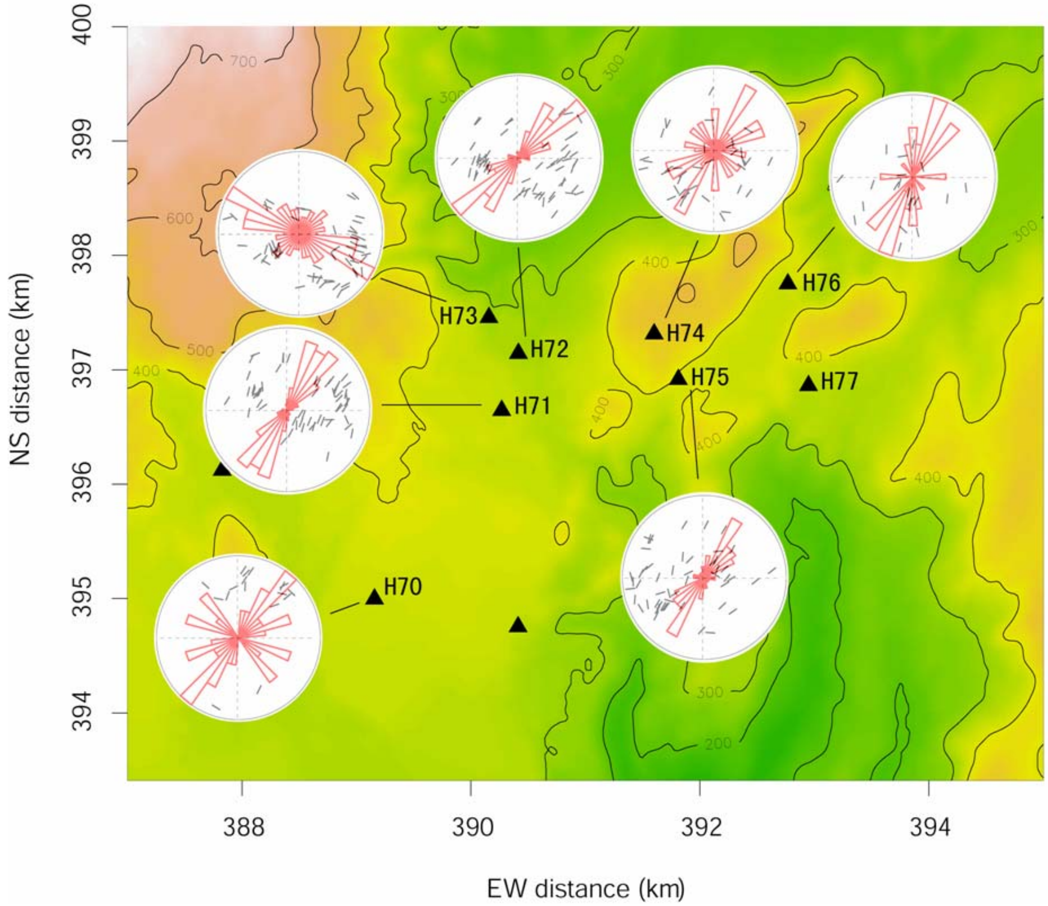

Figure 4.5. Equal-area rose diagrams (polar histograms) of the fast shear-wave polarization directions observed at seven seismic stations in the eastern part of the seismic array. Refer to details in the text.

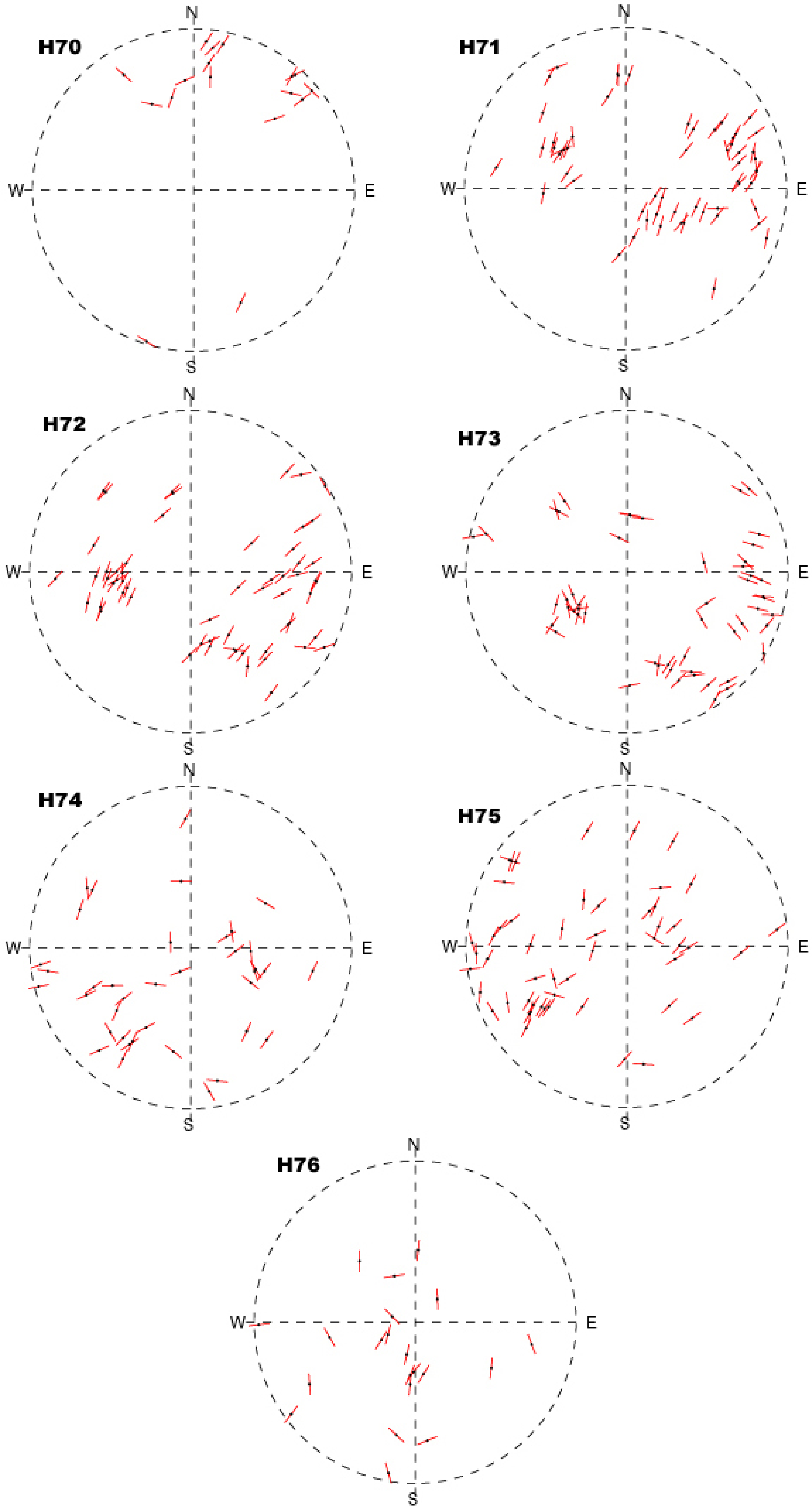

Figure 4.6.

Figure 4.6. Observed fast shear-wave polarization directions at the seven stations plotted on the equal-area projections.

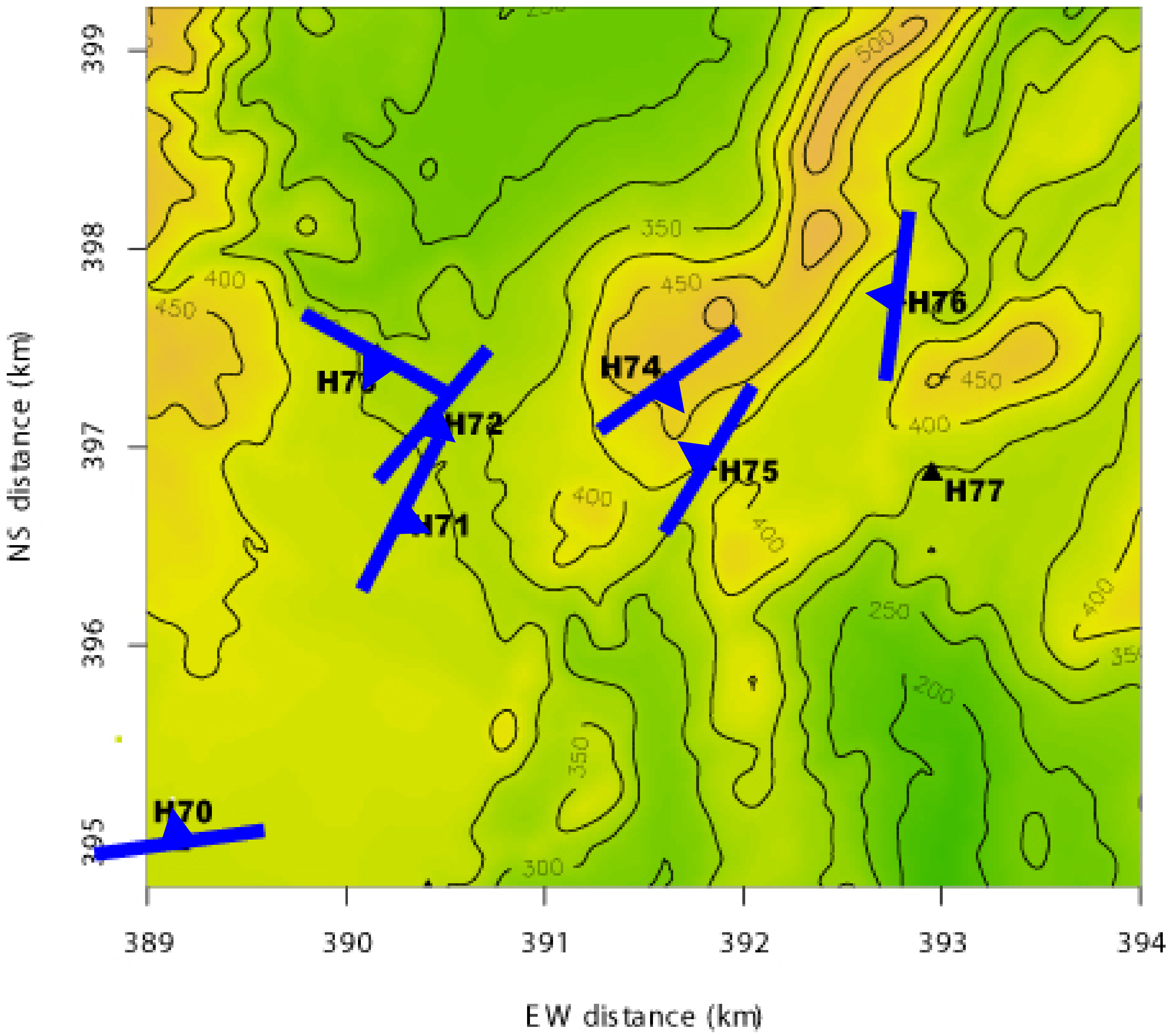

Figure 4.7. Illustration of inversion results for crack strikes and dipping directions at the seven stations. Crack strikes are represented by solid line segments and dipping directions by solid arrows.

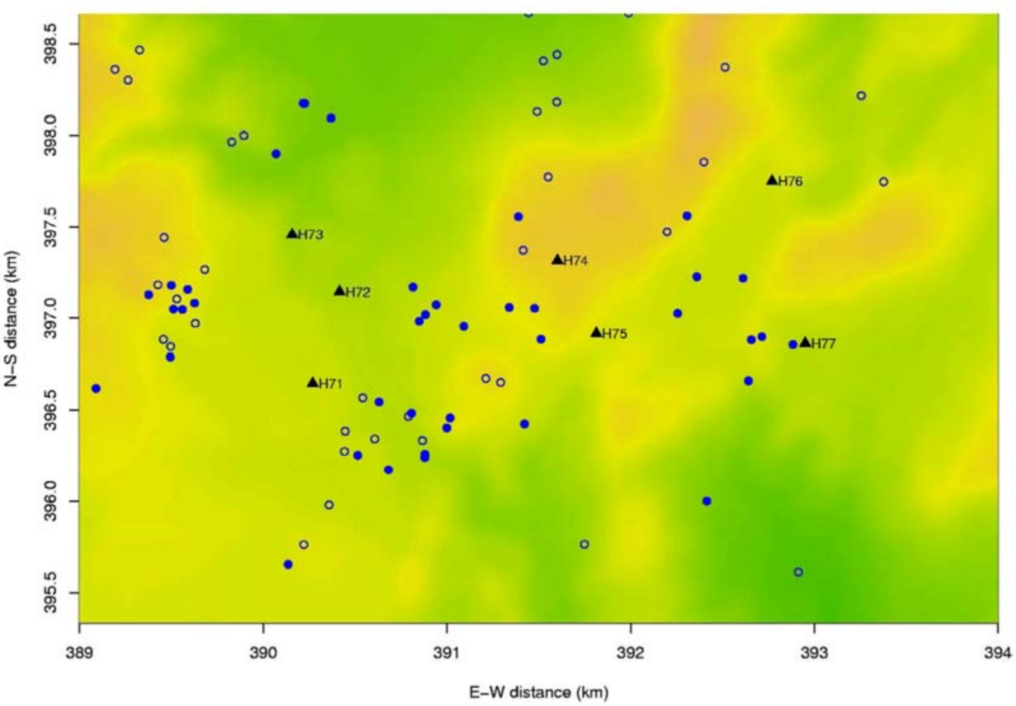

(a)

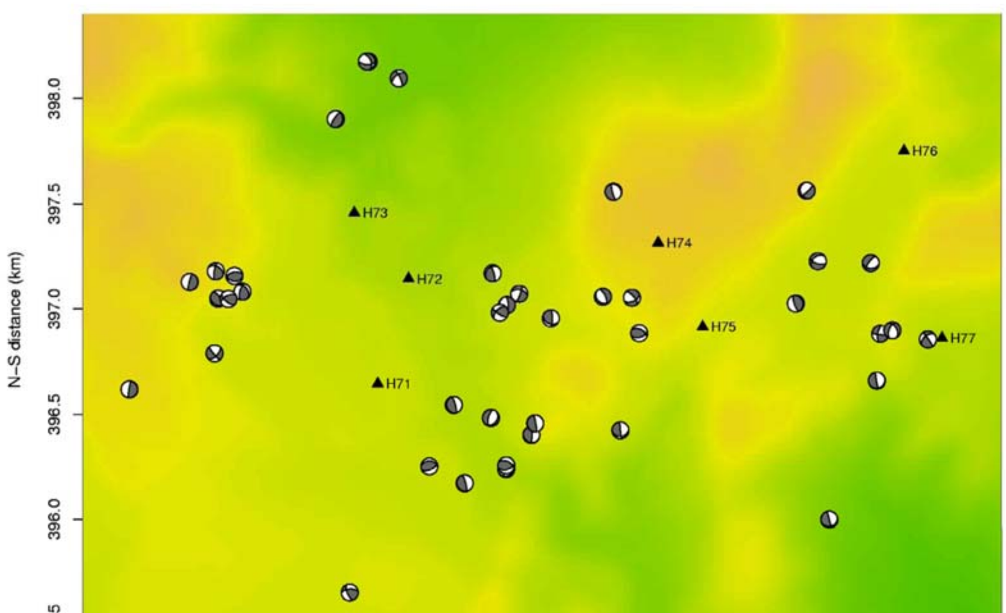

(b)

Figure 4.8. (a) Epicenter of the forty earthquakes selected for the focal mechanism and waveform simulation study that are marked with solid dots. (b) Focal mechanism solution of the forty selected earthquakes plotted at corresponding epicenter.

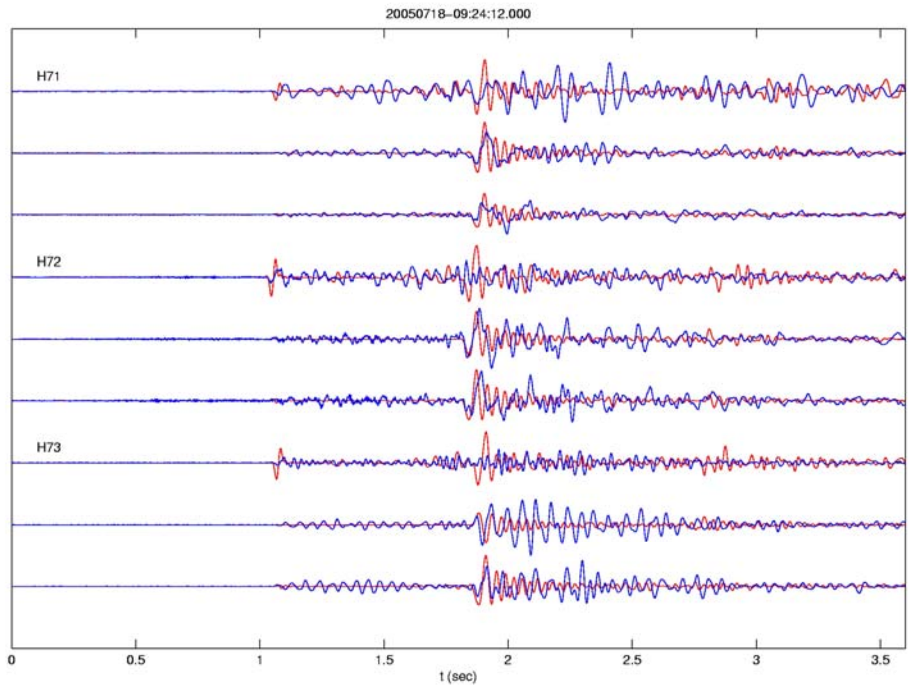

2005071809241

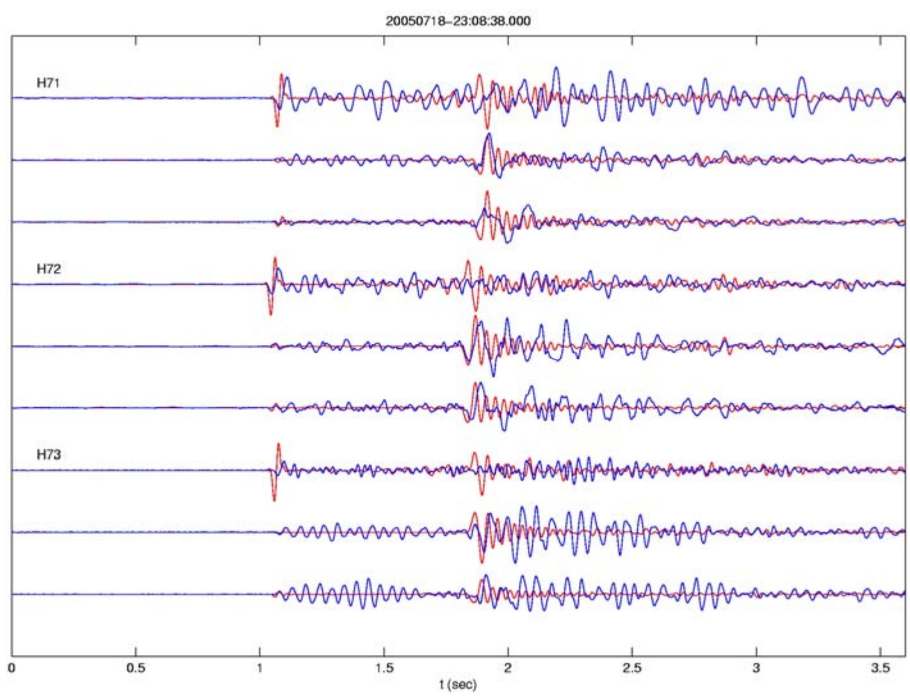

2005071823083

Figure 4.9(1)(2).

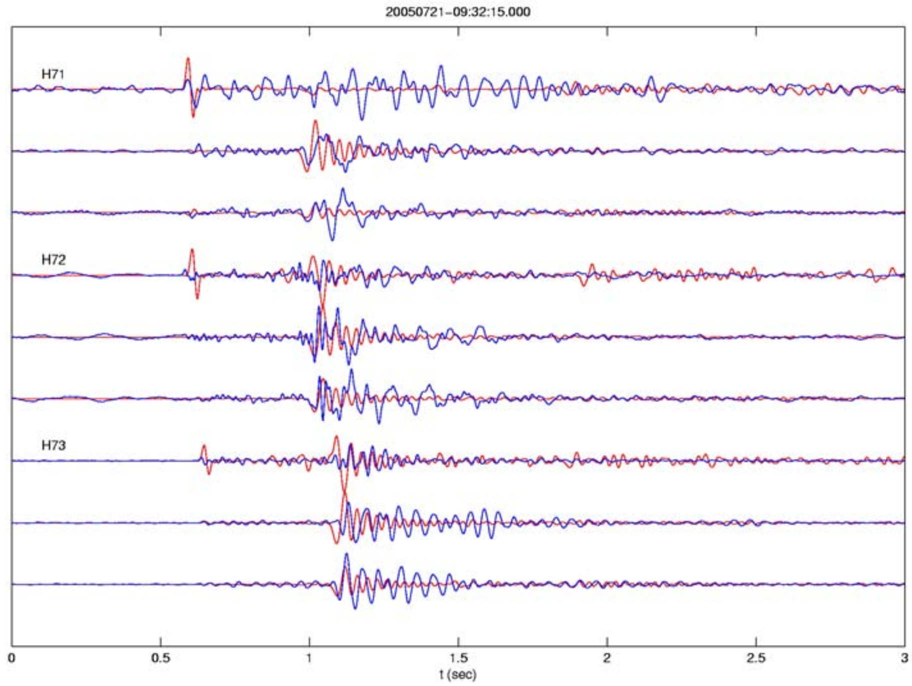

2005072109321

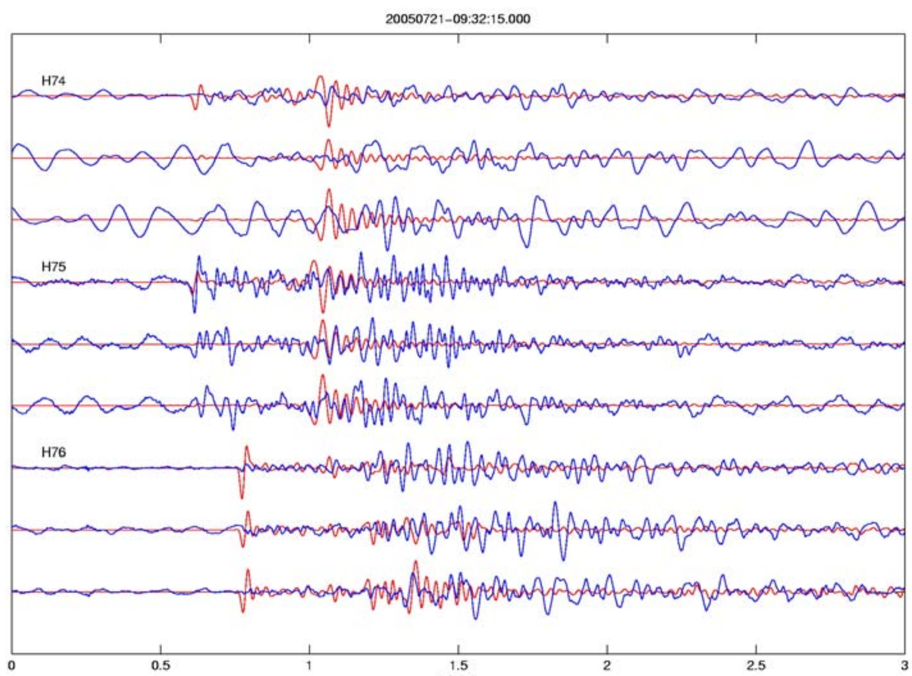

2005072109321

Figure 4.9(3)(4).

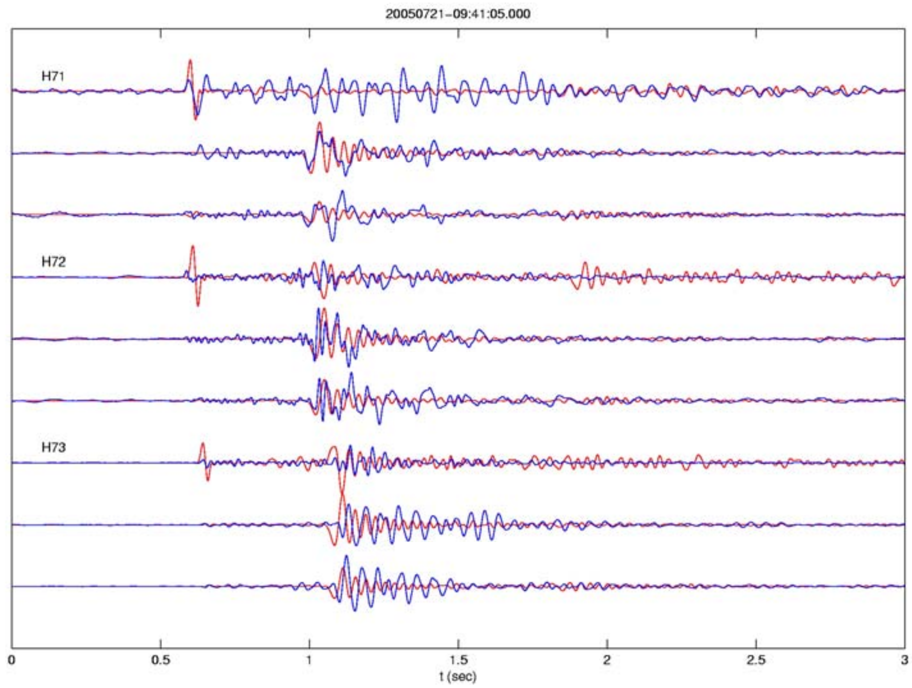

2005072109410

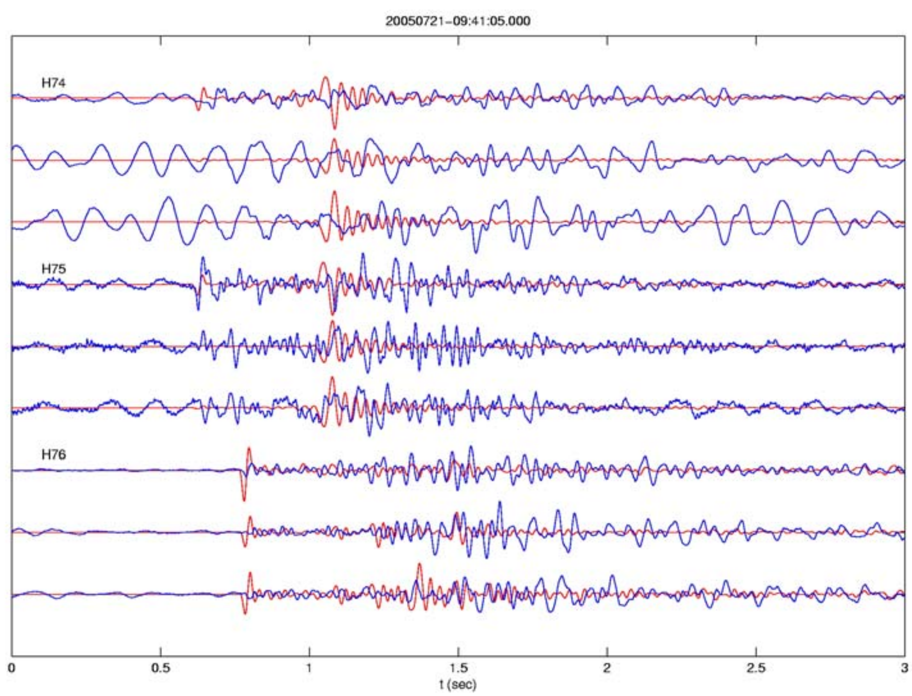

2005072109410

Figure 4.9(5)(6).

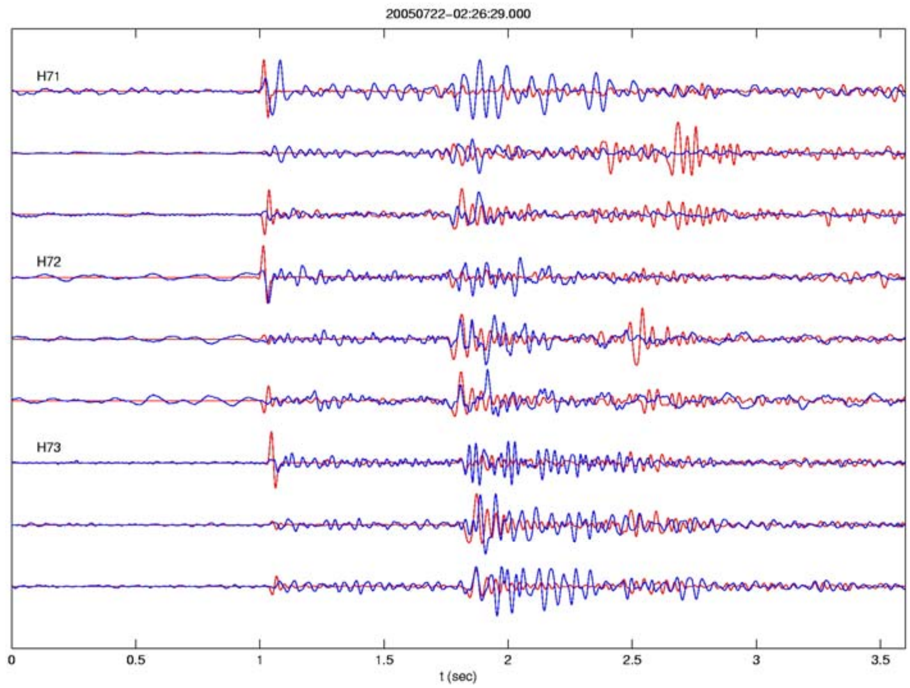

2005072202262

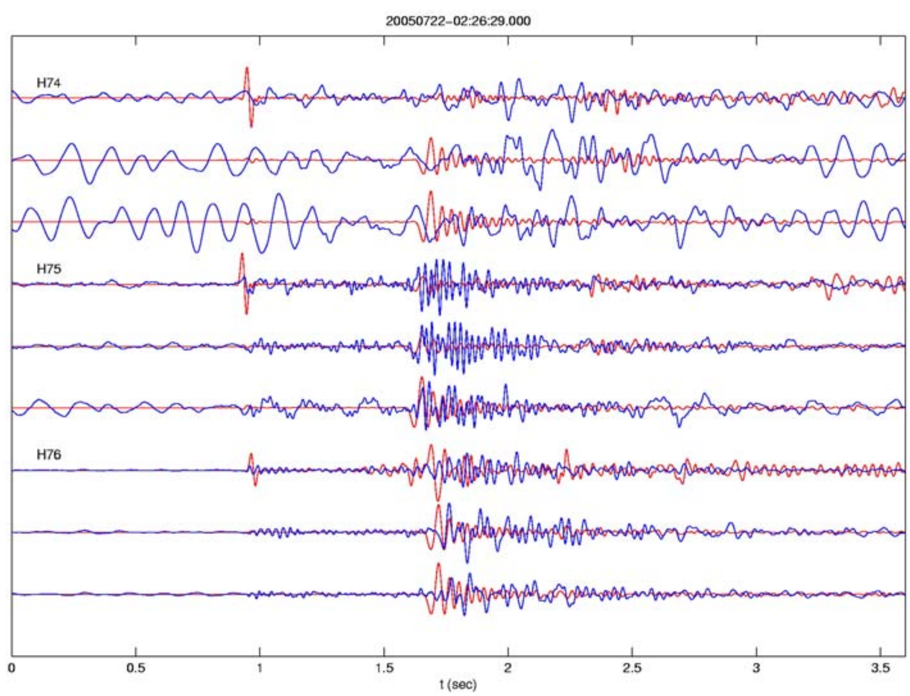

2005072202262

Figure 4.9(7)(8).

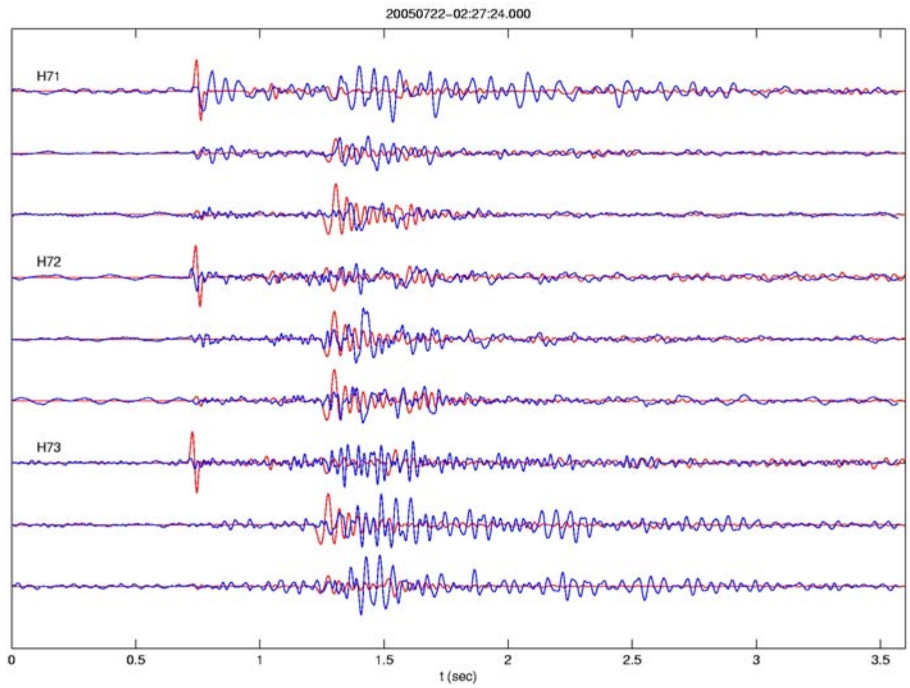

2005072202272

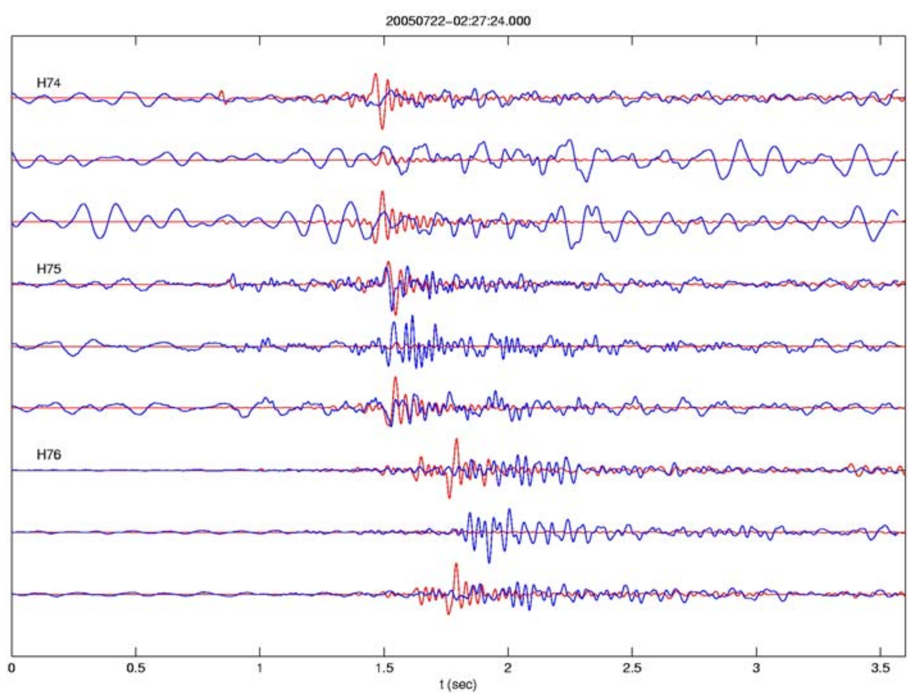

2005072202272

Figure 4.9(9)(10).

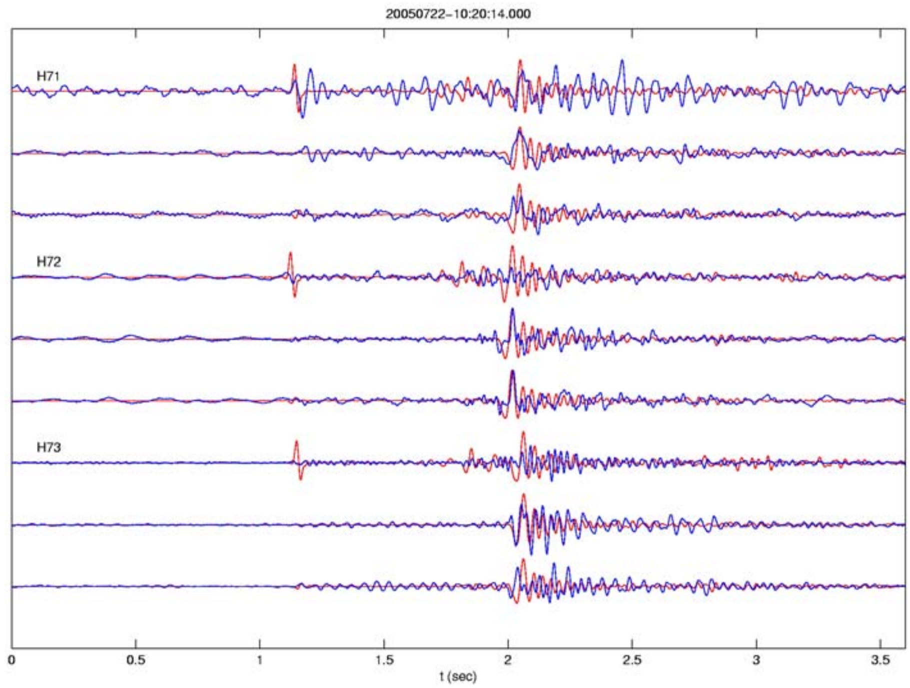

2005072210201

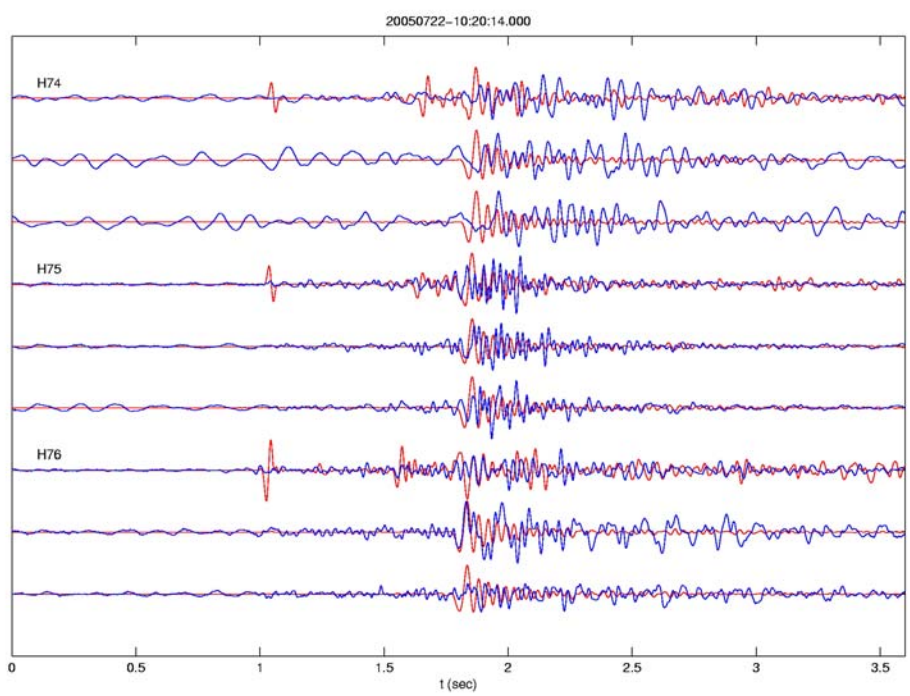

2005072210201

Figure 4.9(11)(12).

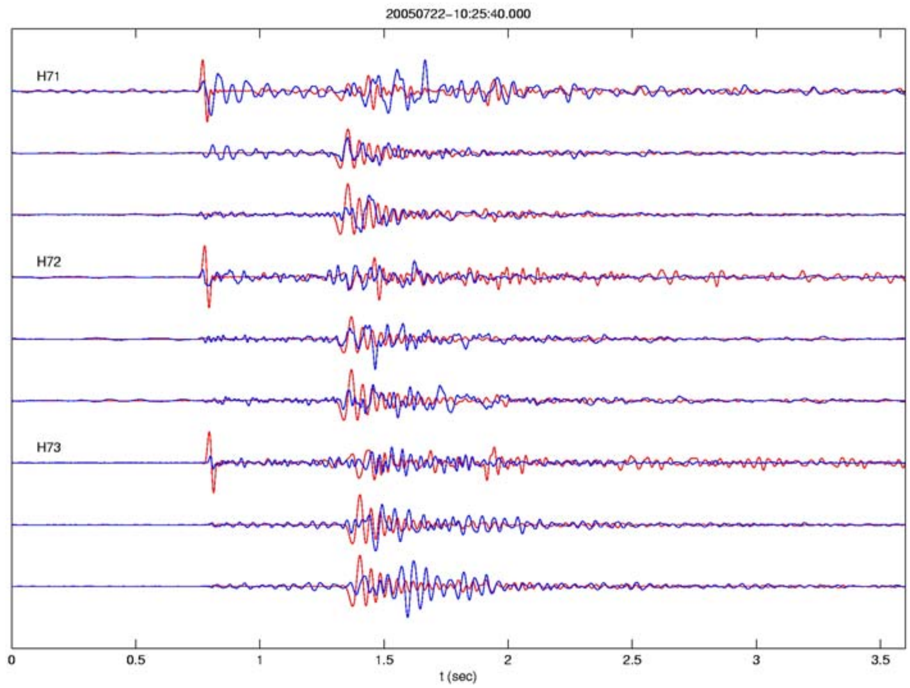

2005072210254

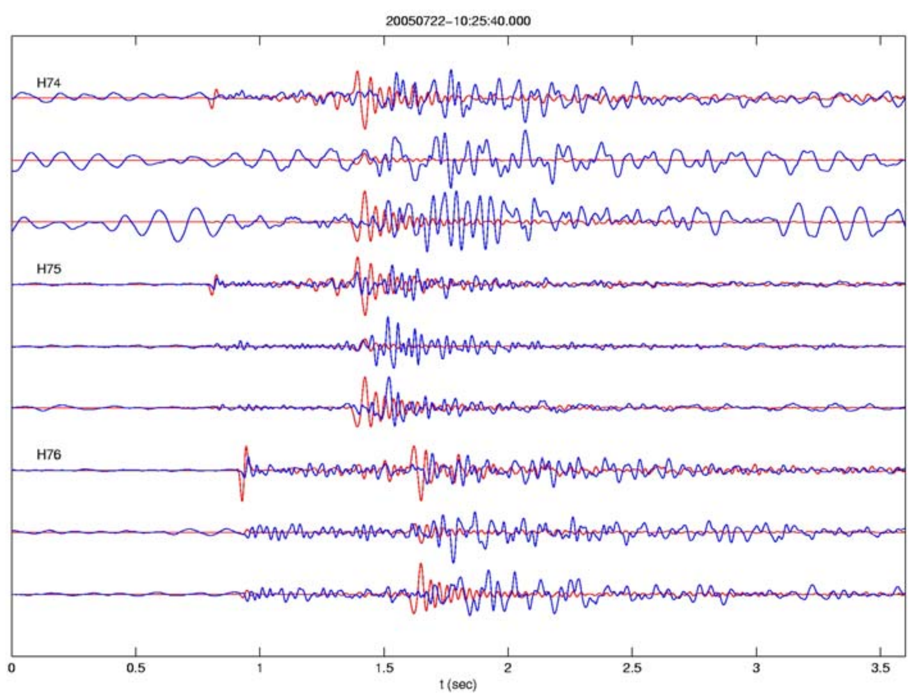

2005072210254

Figure 4.9(13)(14).

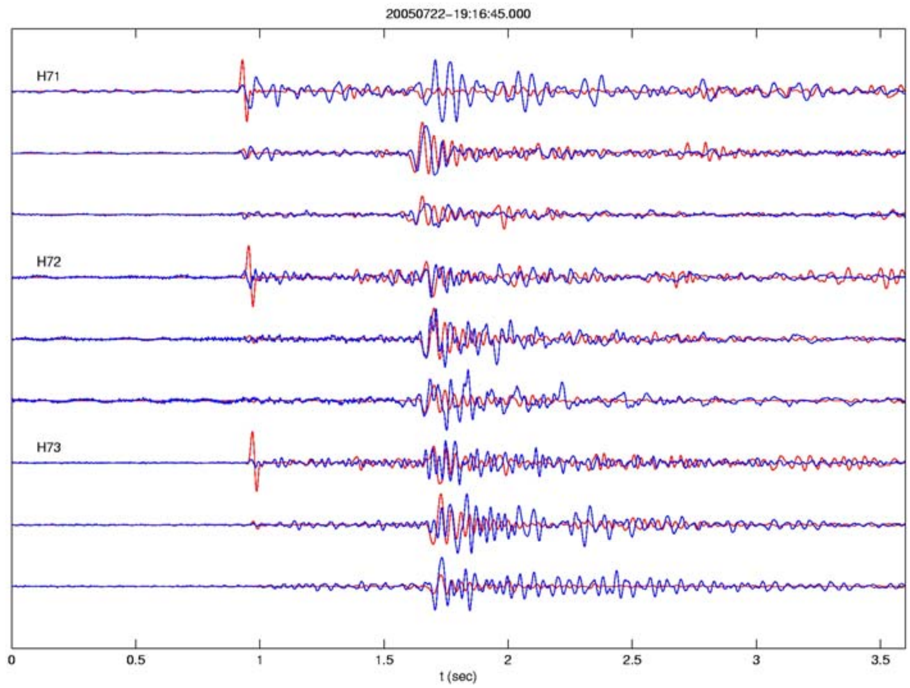

2005072219164

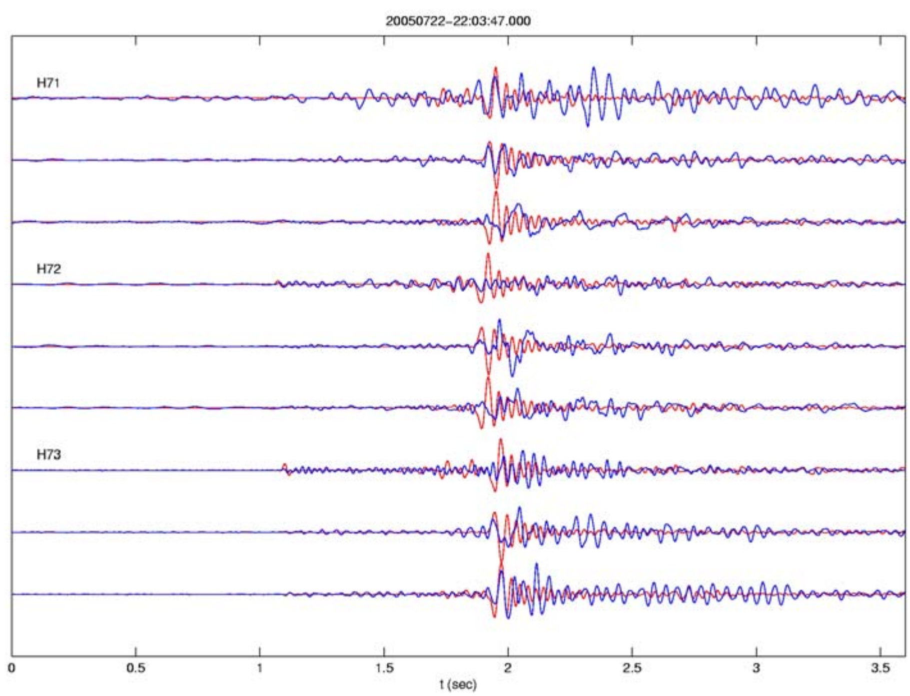

2005072222034

Figure 4.9(15)(16).

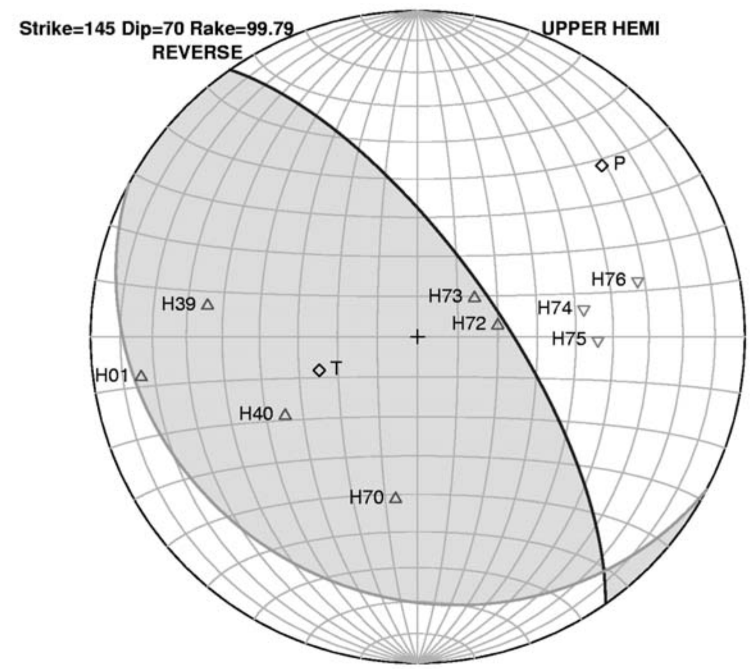

Lat: 64.0573, Lon: -21.2692; Projected: 389.5107, 397.0491

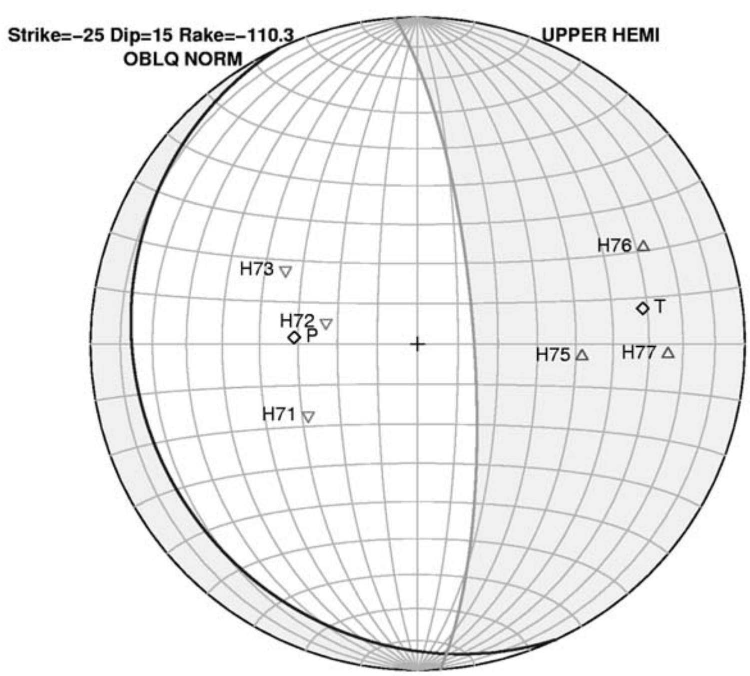

Lat: 64.0575, Lon: -21.2410; Projected: 390.8823, 397.0188

Figure 4.10(1)(2).

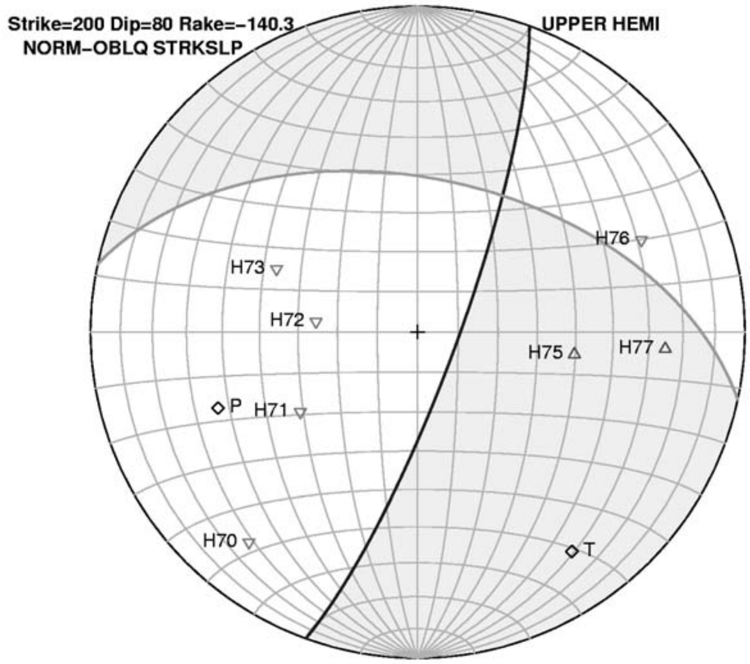

Lat: 64.0580, Lon: -21.2398; Projected: 390.9410, 397.0724

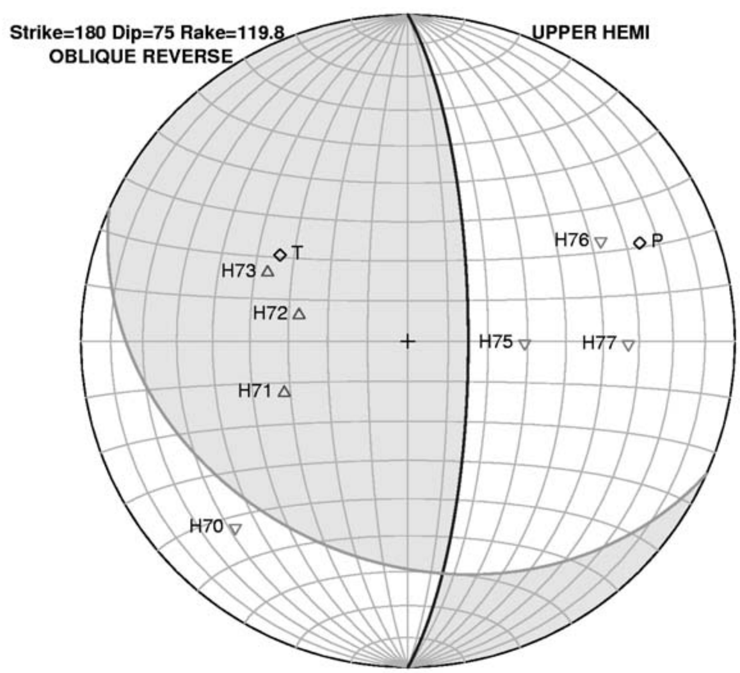

Lat: 64.0570, Lon: -21.2367; Projected: 391.0912, 396.9557

Figure 4.10(3)(4).

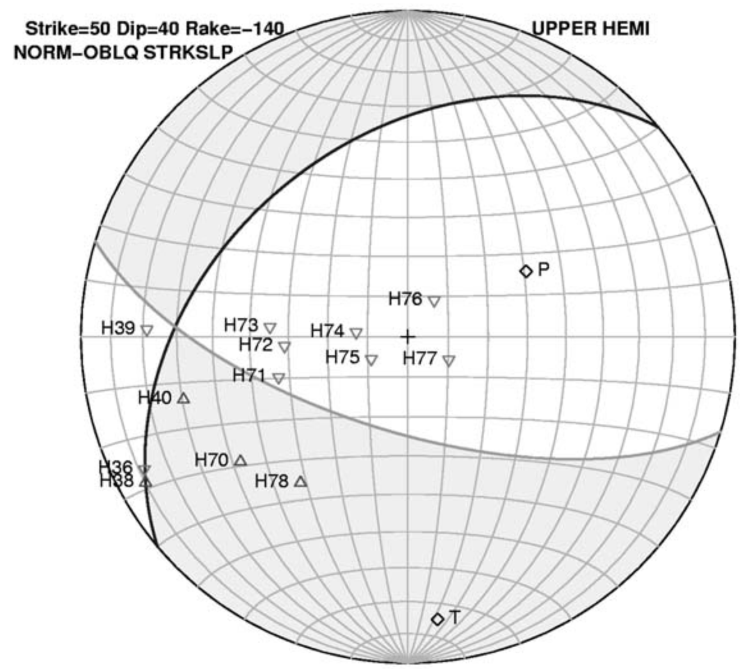

Lat: 64.0598, Lon: -21.2108; Projected: 392.3596, 397.2266

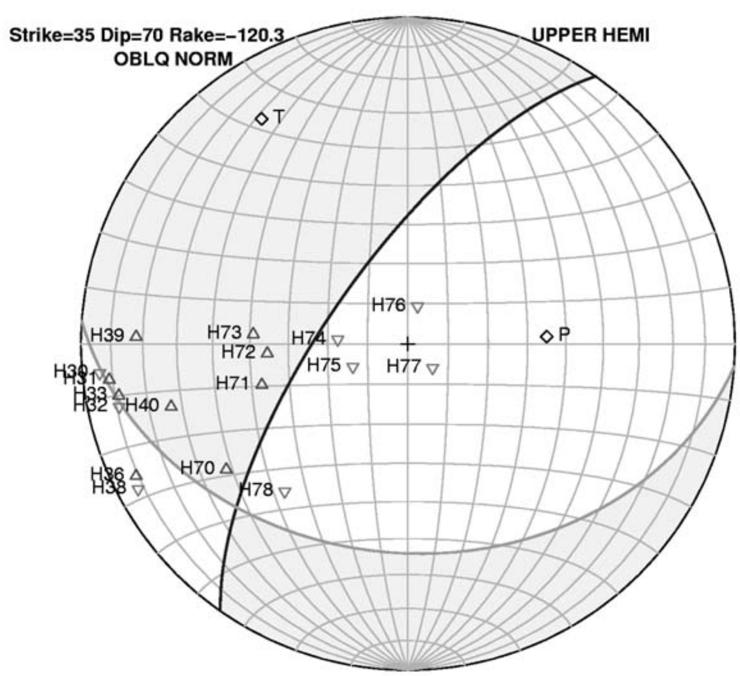

Lat: 64.0598, Lon: -21.2057; Projected: 392.6111, 397.2179

Figure 4.10(5)(6).

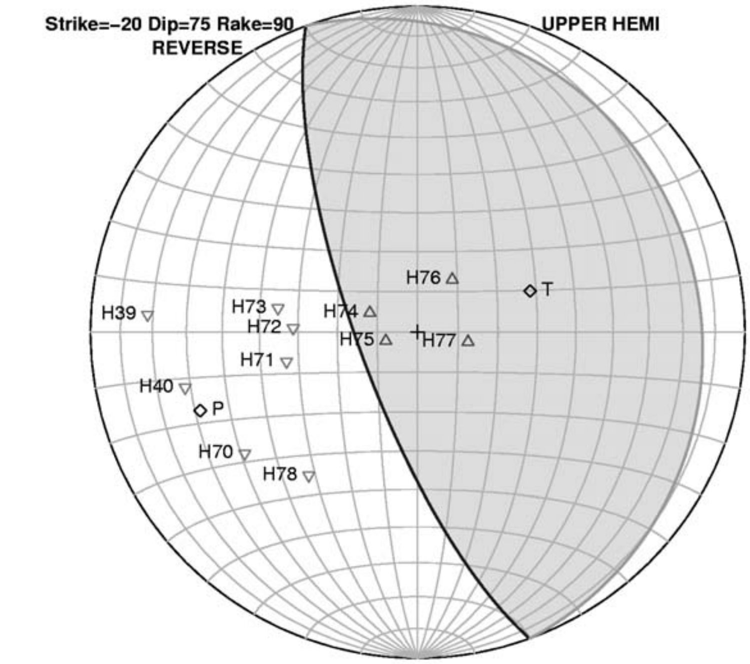

Lat: 64.0580, Lon: -21.2128; Projected: 392.2551, 397.0261

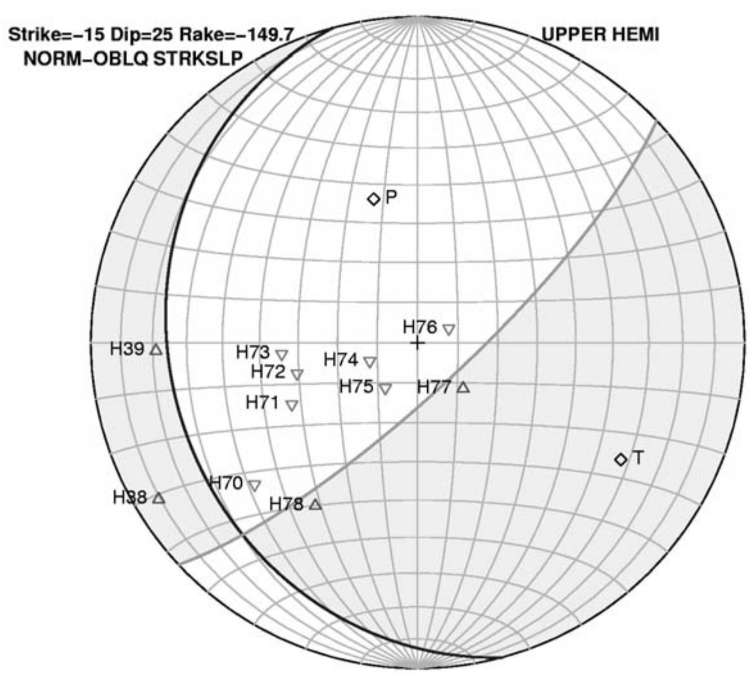

Lat: 64.0628, Lon: -21.2122; Projected: 392.3064, 397.5627

Figure 4.10(7)(8).

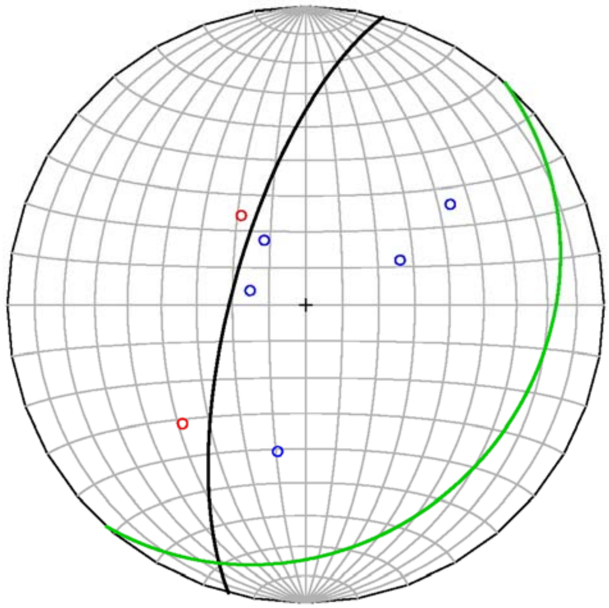

2005072004592: Strike=15 Dip=65 Rake=-100.2
Lat: 64.0527, Lon: -21.2422; Projected: 390.8064, 396.4830

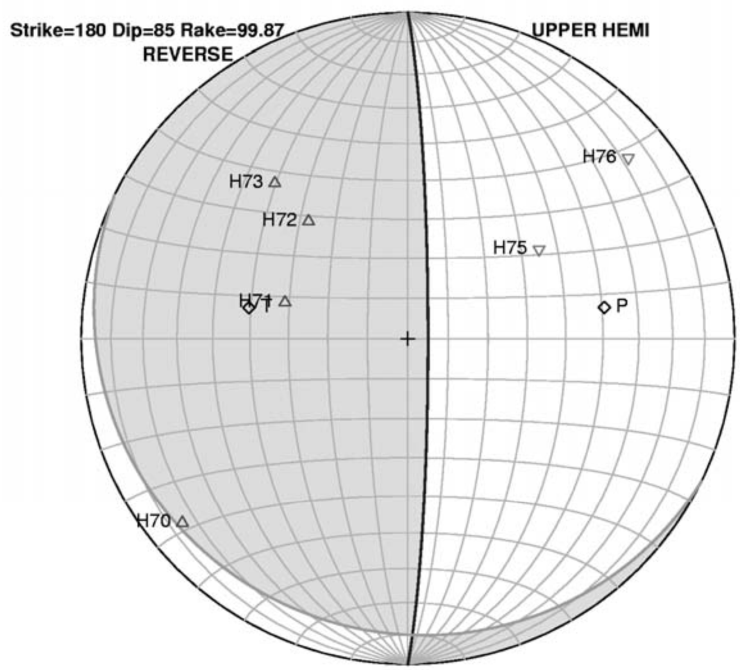

Lat: 64.0520, Lon: -21.2382; Projected: 390.9985, 396.4020

Figure 4.10(9)(10).

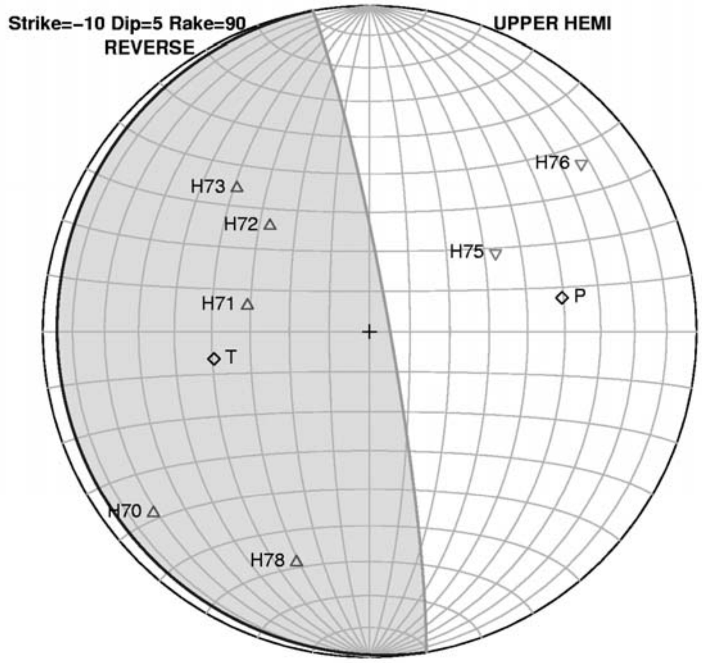

Lat: 64.0525, Lon: -21.2378; Projected: 391.0167, 396.4570

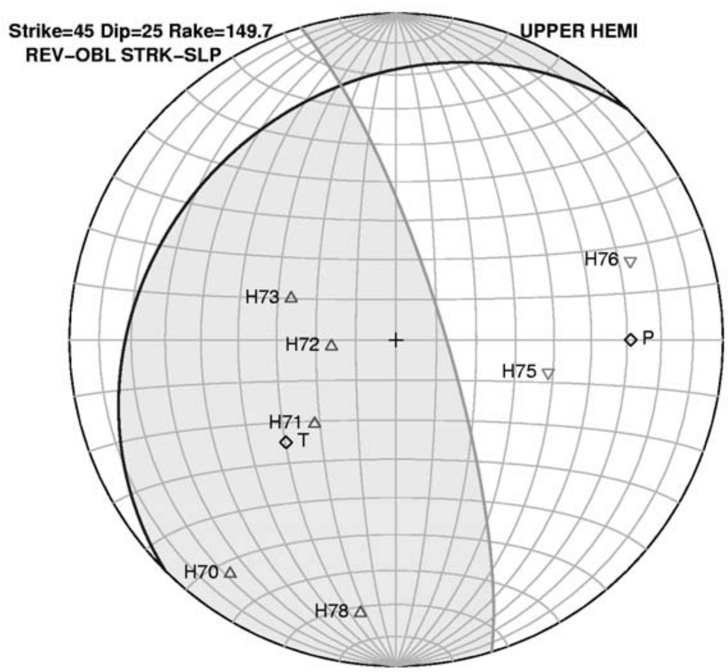

Lat: 64.0588, Lon: -21.2425; Projected: 390.8145, 397.1697

Figure 4.10(11)(12).

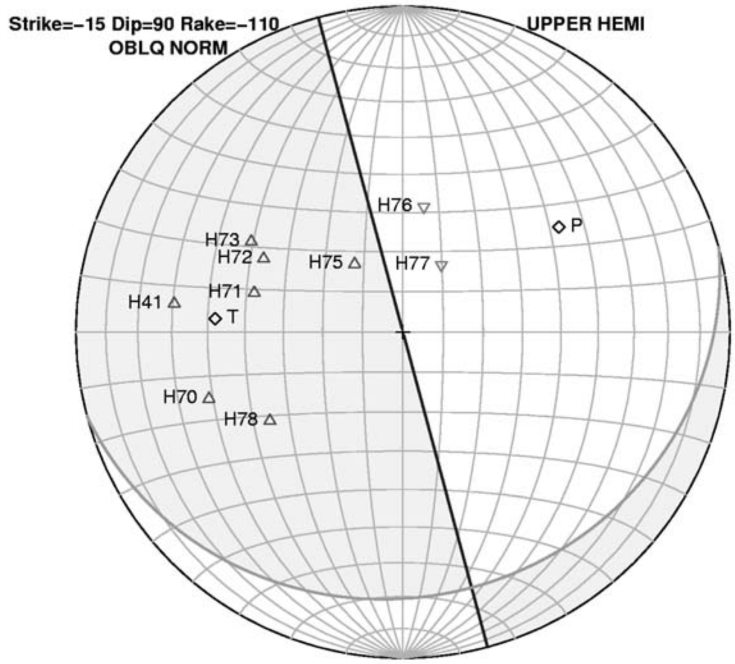

Lat: 64.0488, Lon: -21.2088; Projected: 392.4142, 395.9994

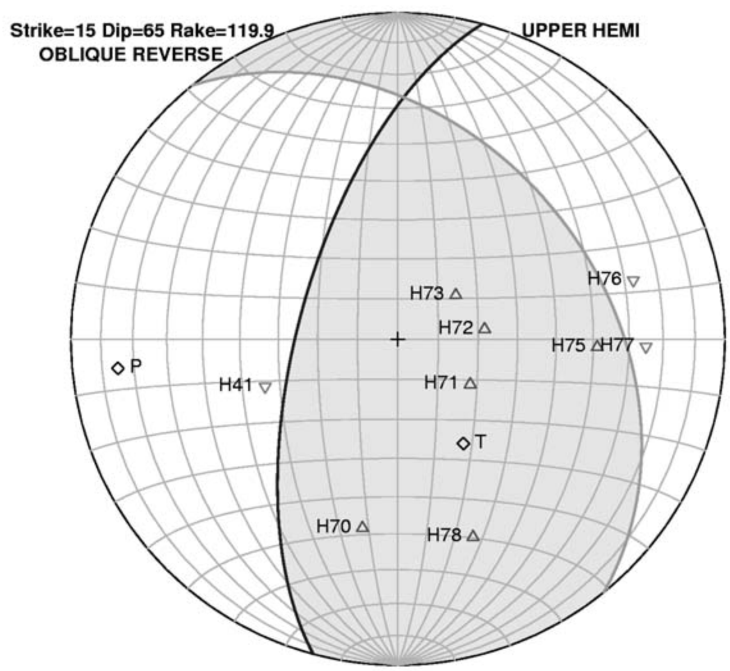

Lat: 64.0577, Lon: -21.2668; Projected: 389.6256, 397.0821

Figure 4.10(13)(14).

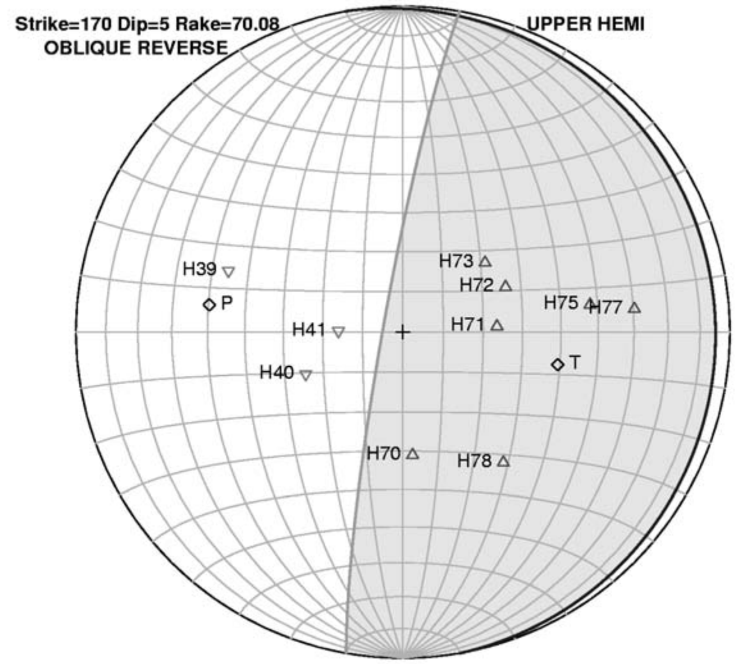

Lat: 64.0533, Lon: -21.2775; Projected: 389.0891, 396.6187

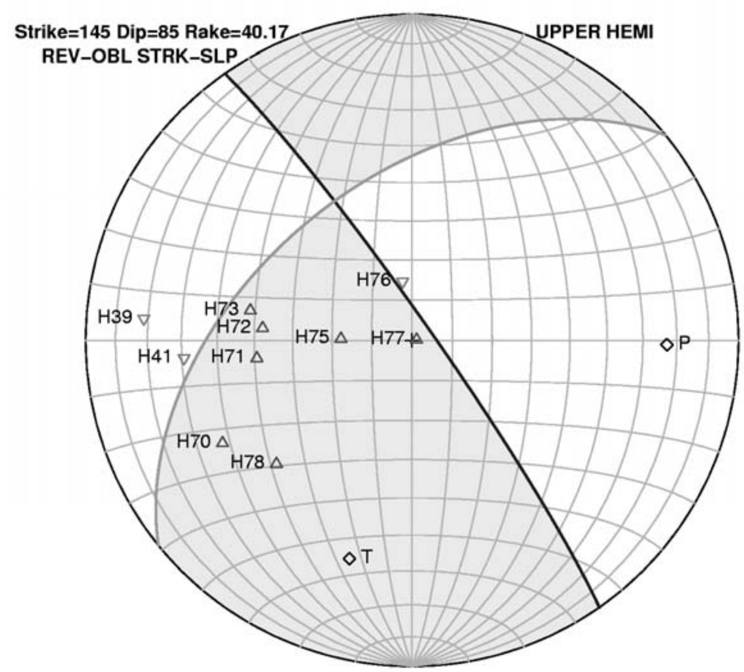

Lat: 64.0567, Lon: -21.1998; Projected: 392.8827, 396.8556

Figure 4.10(15)(16).

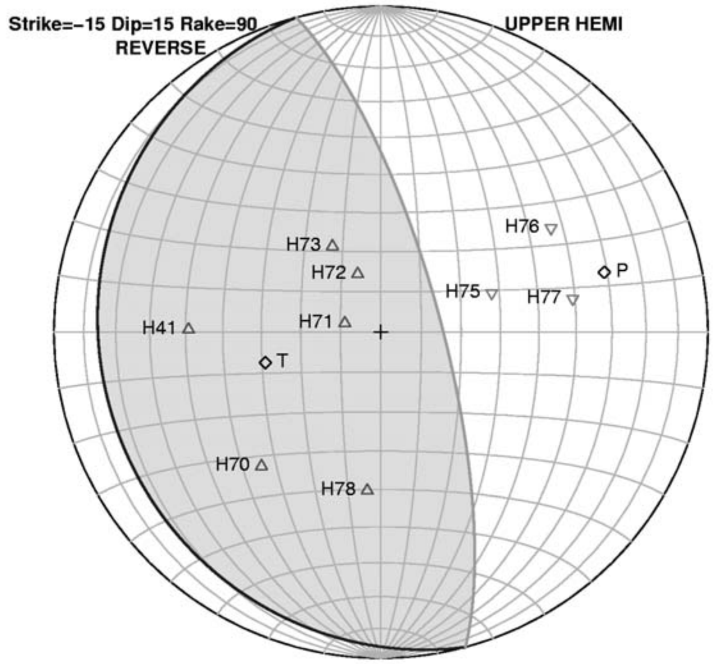

Lat: 64.0532, Lon: -21.2458; Projected: 390.6299, 396.5450

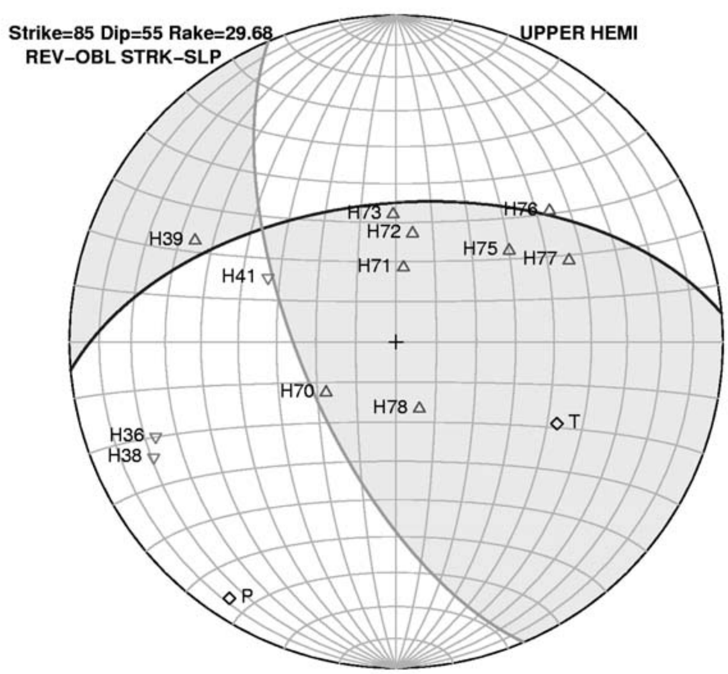

Lat: 64.0450, Lon: -21.2553; Projected: 390.1350, 395.6529

Figure 4.10(17)(18).

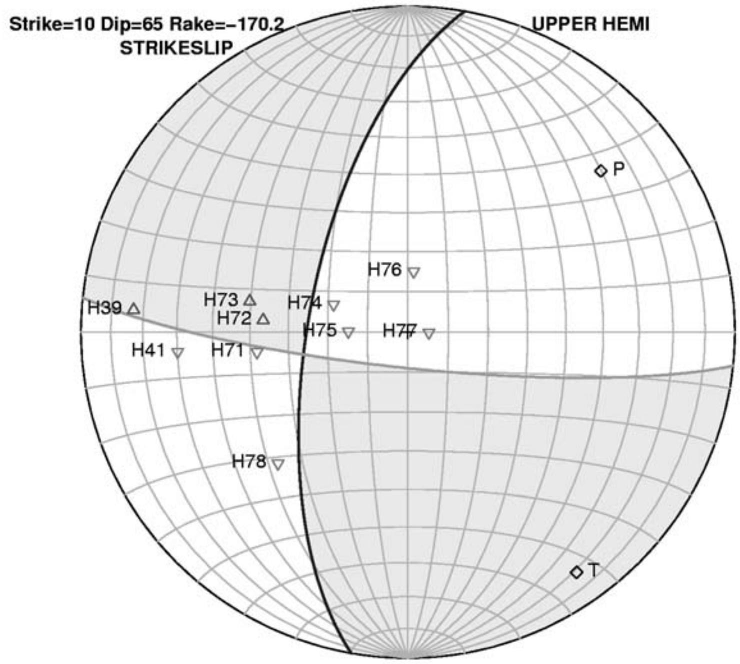

Lat: 64.0568, Lon: -21.2045; Projected: 392.6562, 396.8821

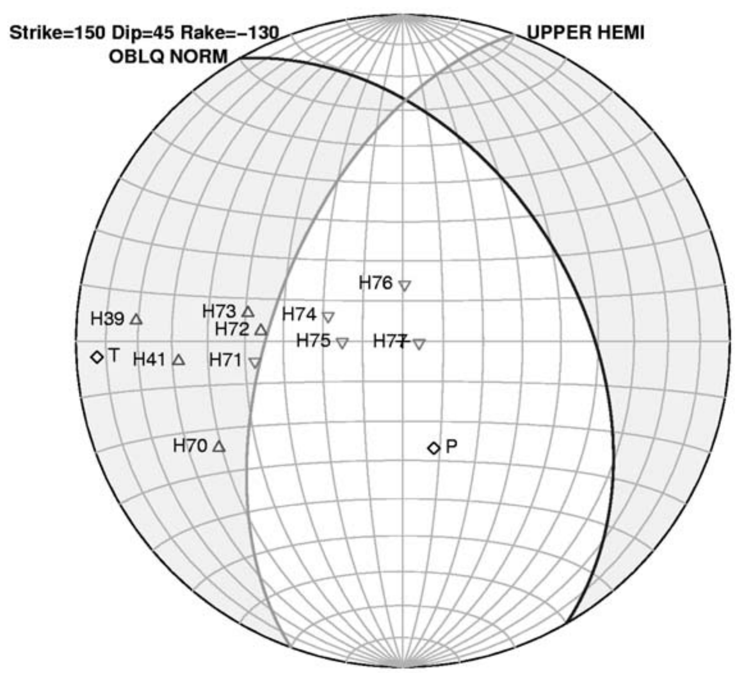

Lat: 64.0570, Lon: -21.2033; Projected: 392.7136, 396.8987

Figure 4.10(19)(20).

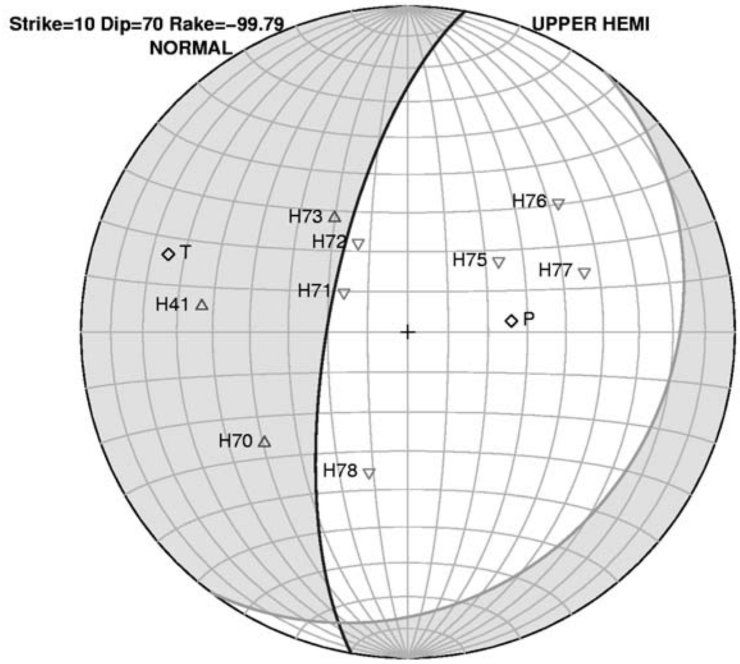

Lat: 64.0505, Lon: -21.2405; Projected: 390.8790, 396.2391

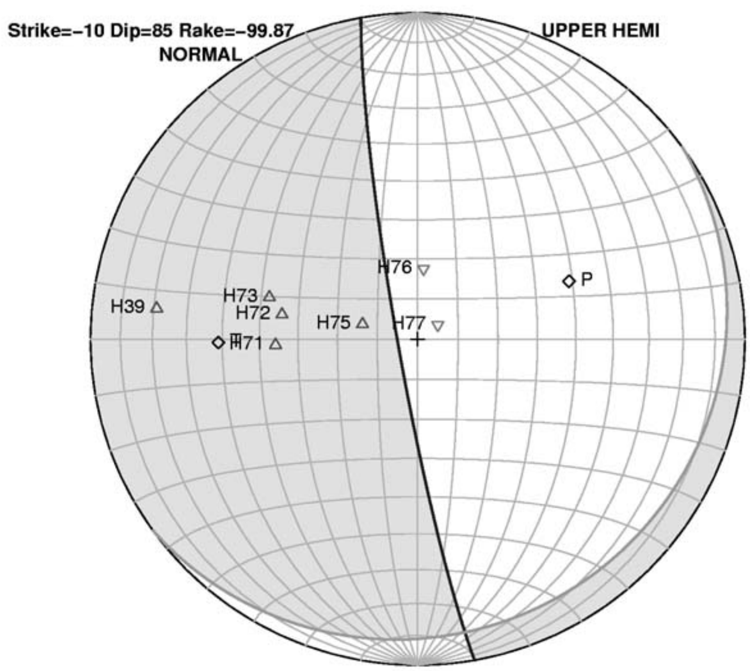

Lat: 64.0548, Lon: -21.2047; Projected: 392.6403, 396.6599

Figure 4.10(21)(22).

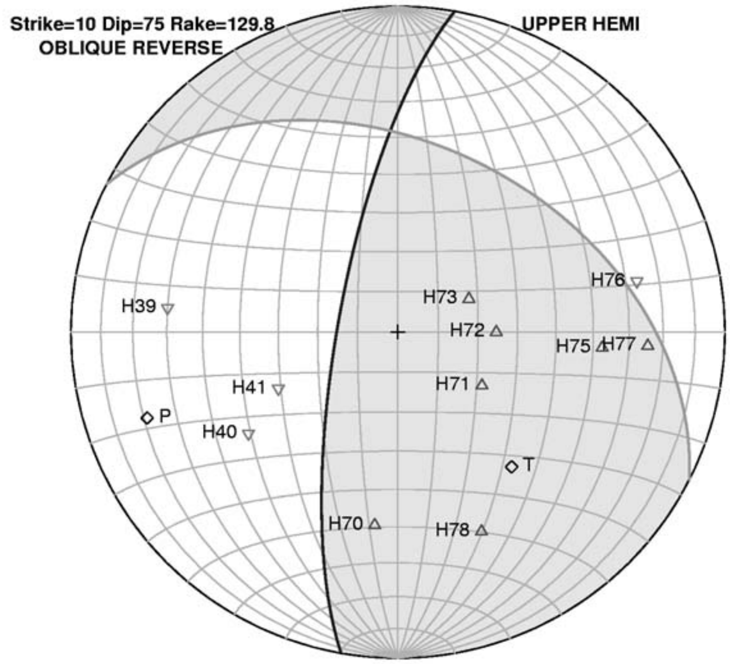

Lat: 64.0585, Lon: -21.2695; Projected: 389.4991, 397.1795

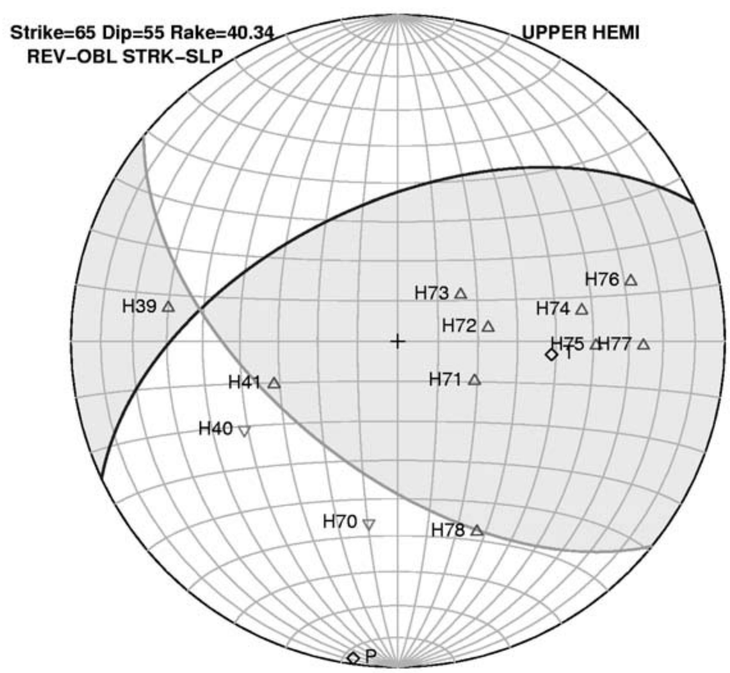

Lat: 64.0573, Lon: -21.2682; Projected: 389.5594, 397.0474

Figure 4.10(23)(24).

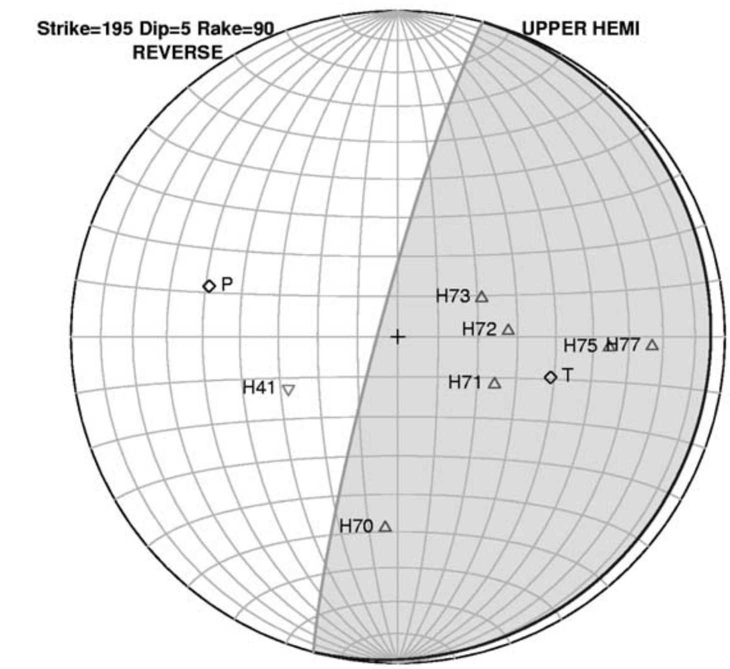

Lat: 64.0580, Lon: -21.2720; Projected: 389.3755, 397.1283

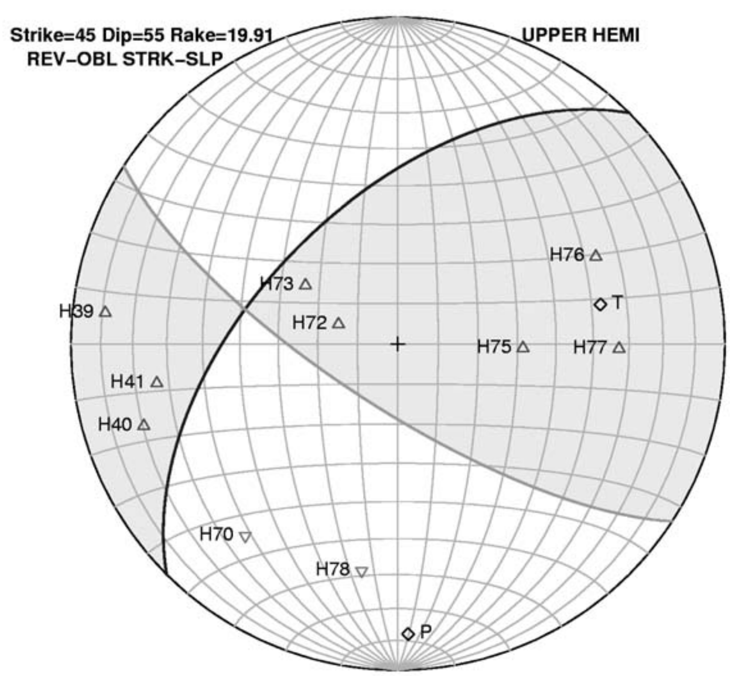

Lat: 64.0572, Lon: -21.2417; Projected: 390.8485, 396.9828

Figure 4.10(25)(26).

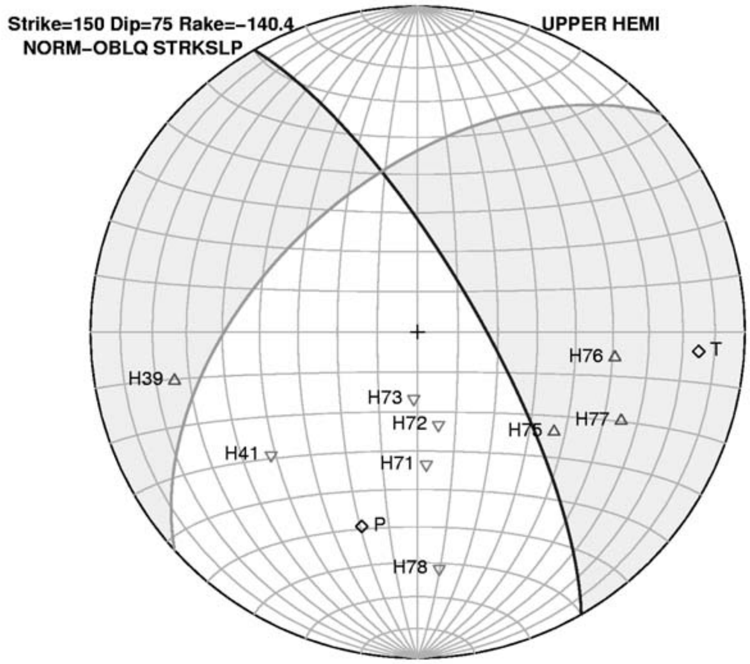

Lat: 64.0677, Lon: -21.2553; Projected: 390.2250, 398.1747

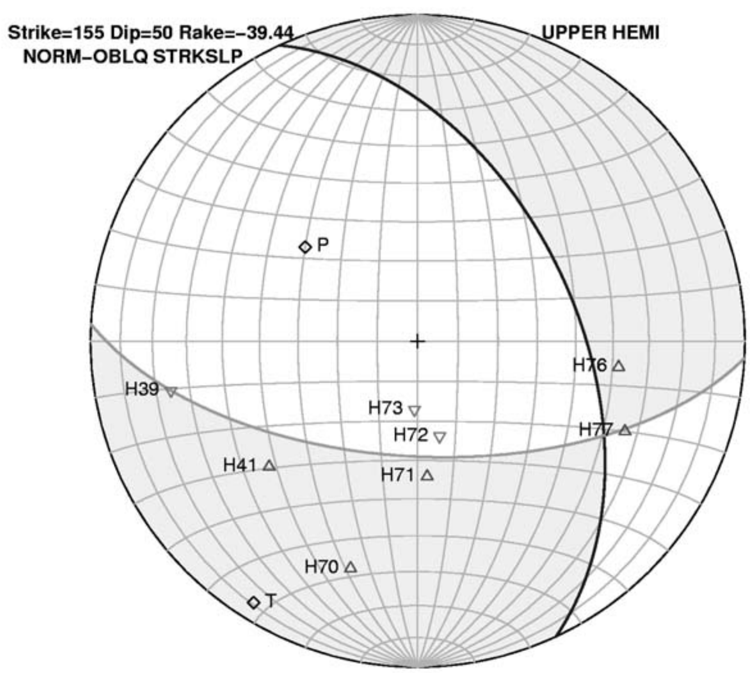

Lat: 64.0677, Lon: -21.2555; Projected: 390.2169, 398.1750

Figure 4.10(27)(28).

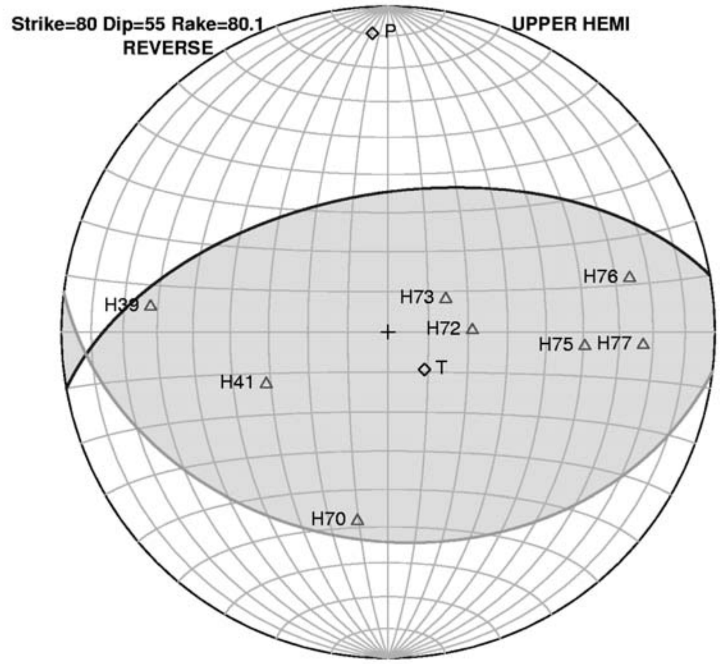

Lat: 64.0583, Lon: -21.2677; Projected: 389.5877, 397.1578

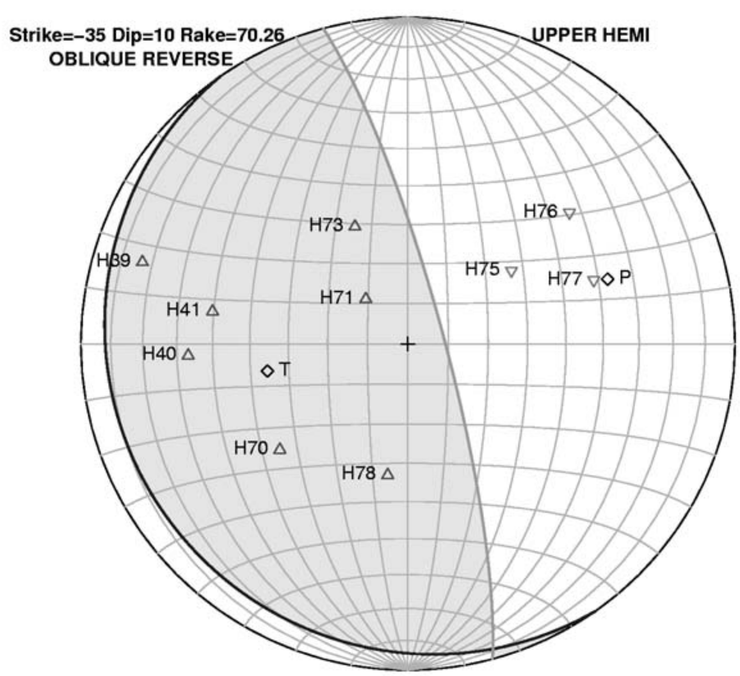

Lat: 64.0498, Lon: -21.2445; Projected: 390.6816, 396.1718

Figure 4.10(29)(30).

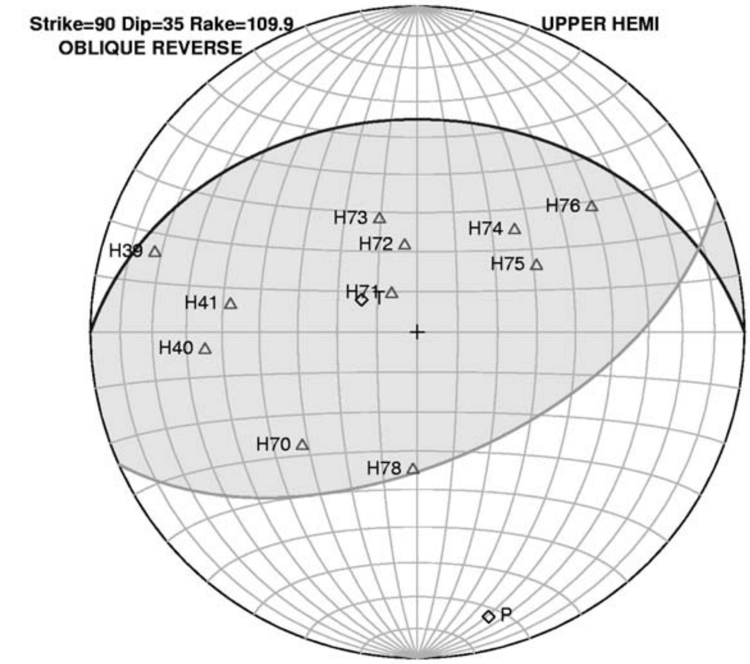

Lat: 64.0505, Lon: -21.2480; Projected: 390.5139, 396.2521

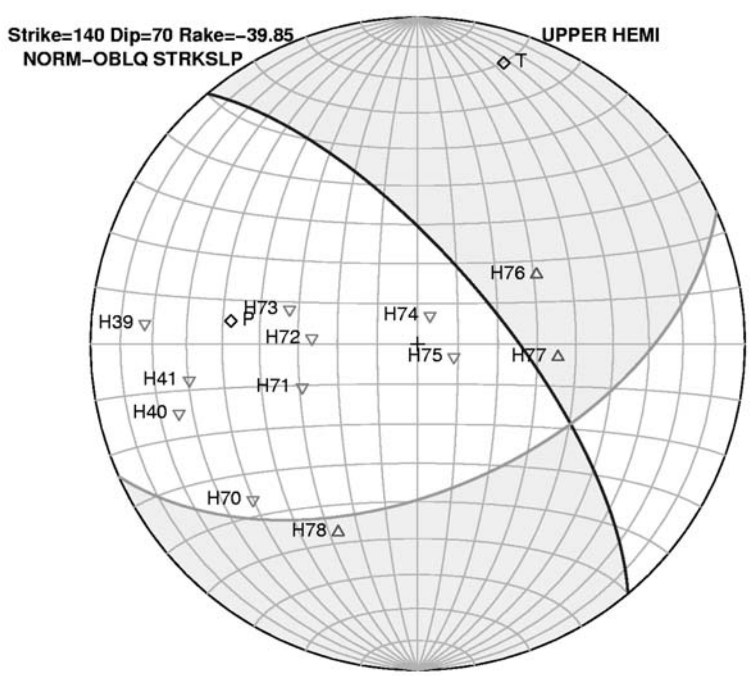

Lat: 64.0580, Lon: -21.2288; Projected: 391.4764, 397.0534

Figure 4.10(31)(32).

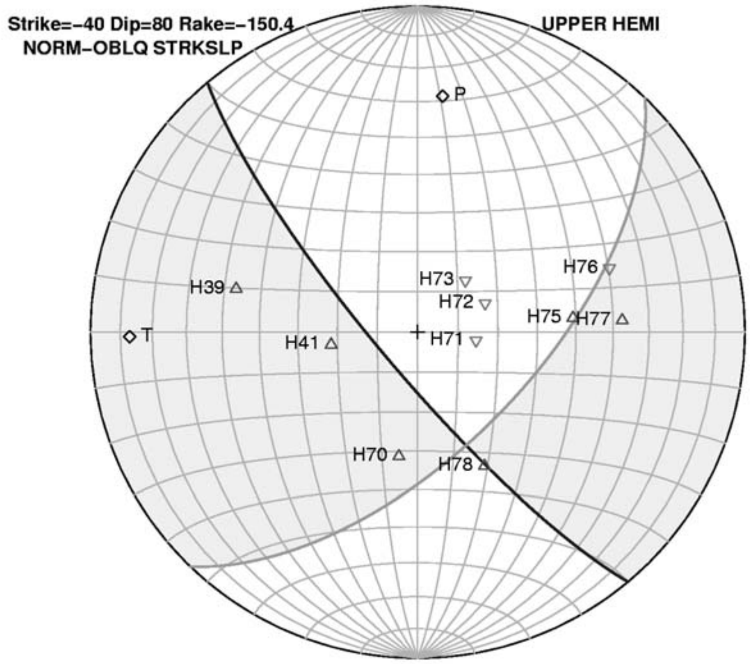

Lat: 64.0550, Lon: -21.2693; Projected: 389.4933, 396.7898

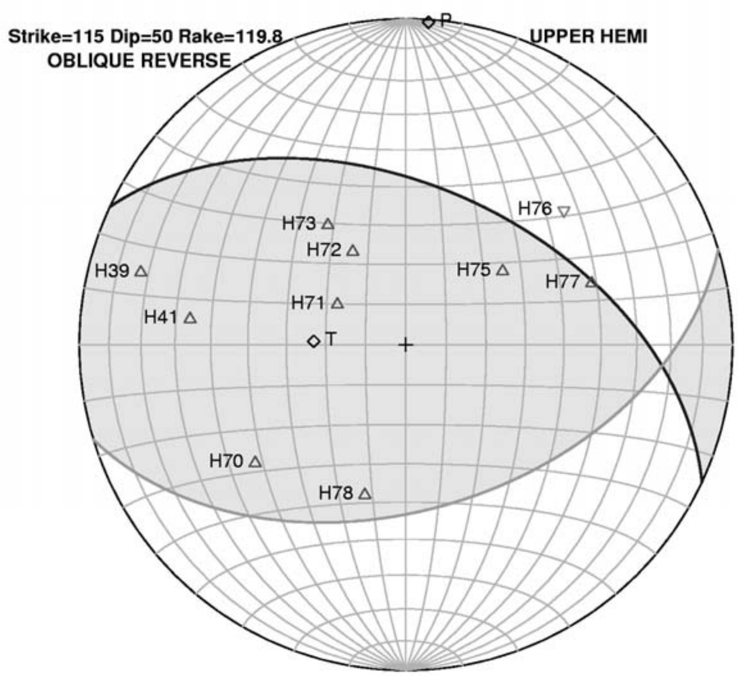

Lat: 64.0507, Lon: -21.2405; Projected: 390.8796, 396.2576

Figure 4.10(33)(34).

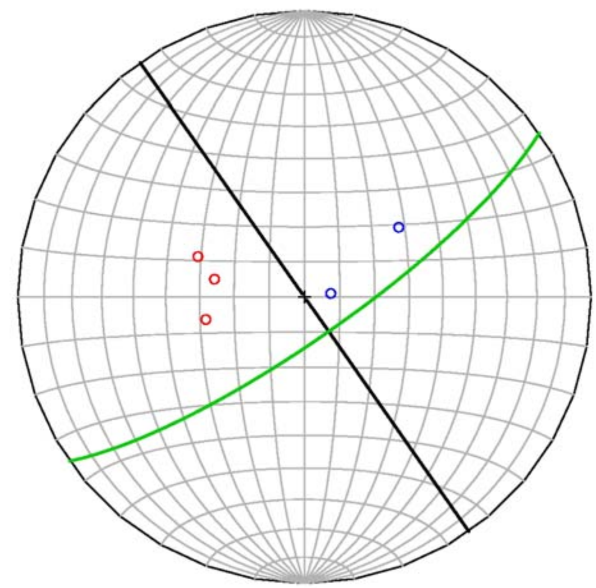

2005080405095: Strike=145 Dip=90 Rake=168.0
Lat: 64.0565, Lon: -21.2280; Projected: 391.5111, 396.8851

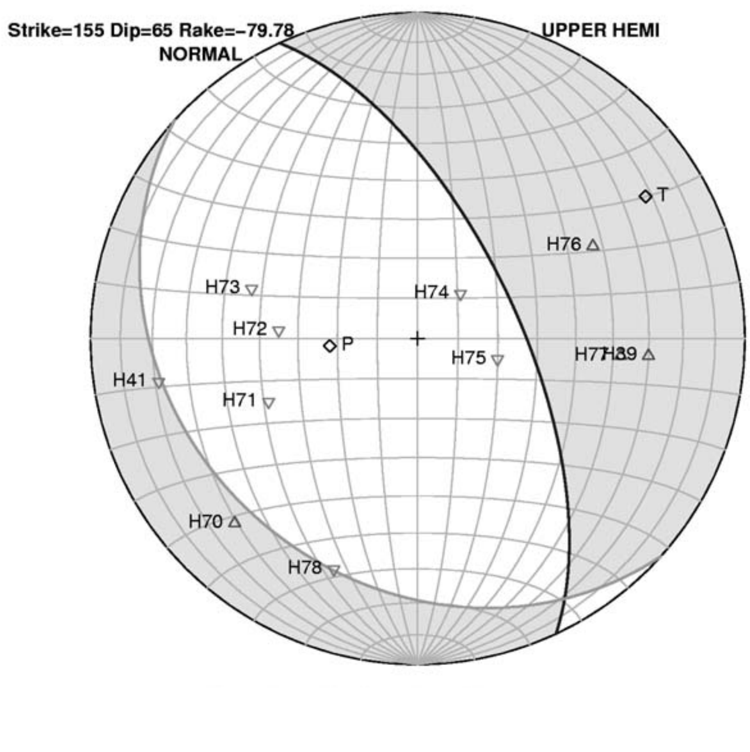

Lat: , 64.0580, Lon: -21.2317; Projected: 391.3385, 397.0583

Figure 4.10(35)(36).

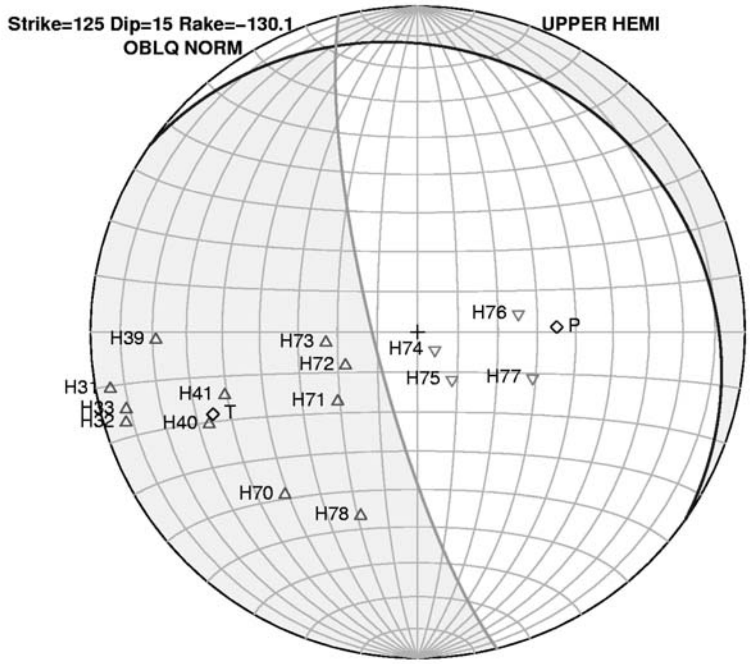

Lat: 64.0625, Lon: -21.2310; Projected: 391.3886, 397.5578

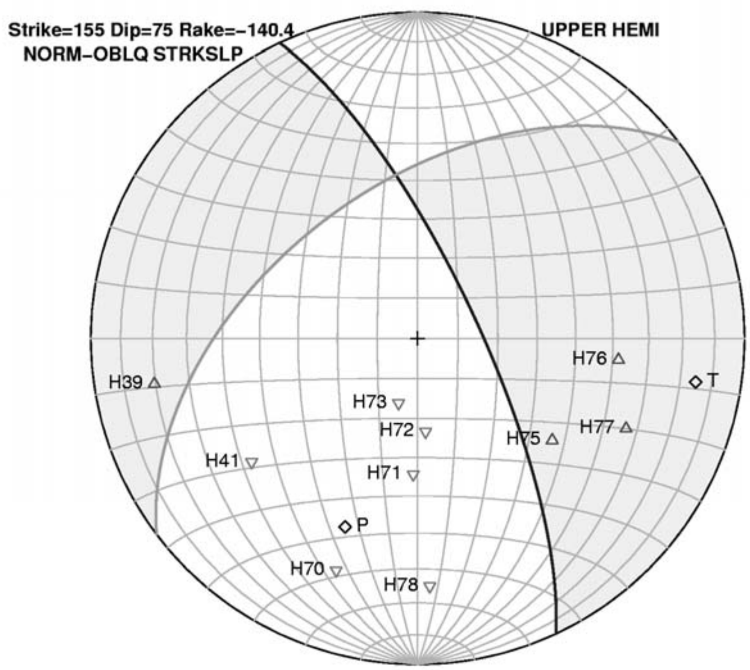

Lat: 64.0670, Lon: -21.2523; Projected: 390.3683, 398.0953

Figure 4.10(37)(38).

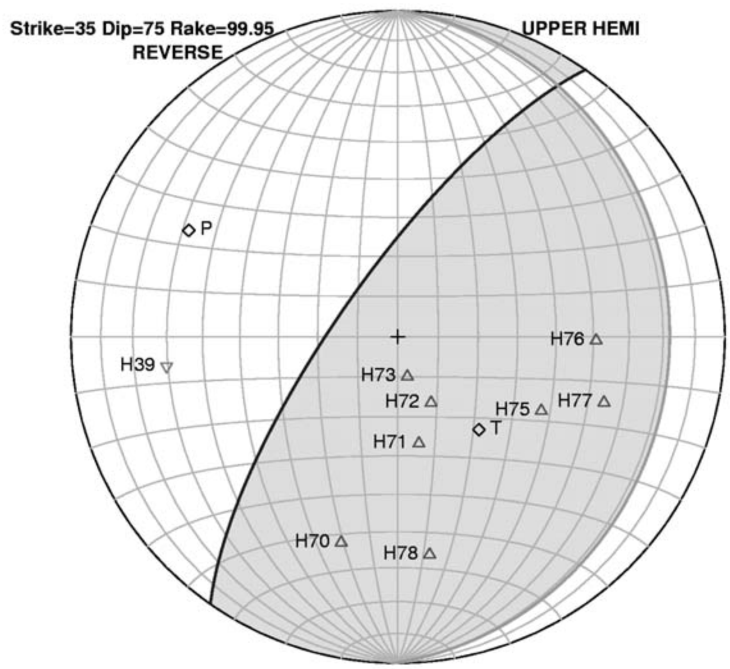

Lat: 64.0652, Lon: -21.2583; Projected: 390.0691, 397.9017

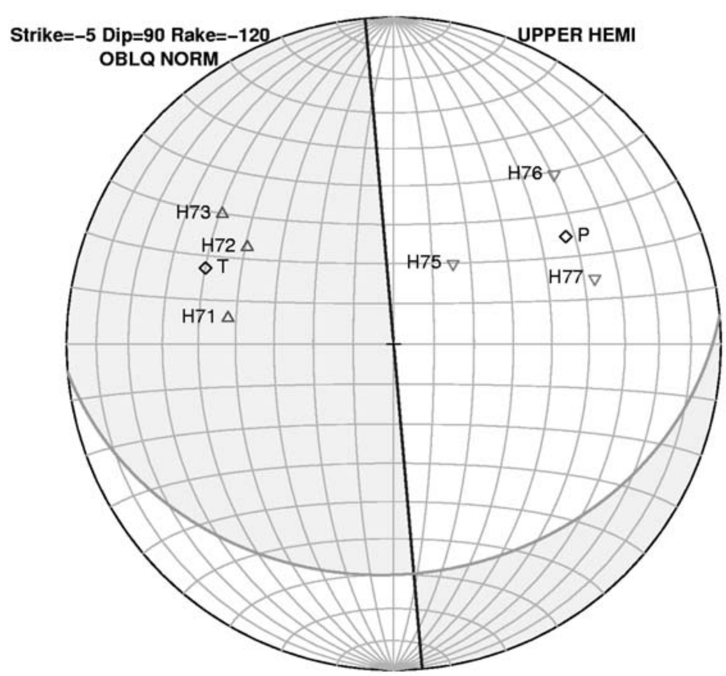

Lat: 64.0523, -21.2295, Lon: ; Projected: 391.4217, 396.4241

Figure 4.10(39)(40).

CHAPTER V

AUTOMATIC DETECTION OF SUBSURFACE FRACTURES IN GEOTHERMAL FIELDS USING SHEAR-WAVE SPLITTING

Introduction

Since the discovery of seismic anisotropy in the oceanic mantle in 1964, seismologists have been attempting to characterize it in crust and mantle. One typical type of anisotropy is produced by fractures or cracks, among several other types. Many researchers have well described the elastic effects of waves propagating through such media and several numerical methods have been introduced to predict in particular the behavior of shear waves, because when a seismic wave travels through stress-aligned, usually also fluid-filled cracks in the upper crust, the incident shear wave will split into two waves traveling at different speeds. This phenomenon is well known as shear-wave splitting (SWS).

The objective of this chapter is to build up a general modeling process to study the behavior of split shear waves as described in the chart below:

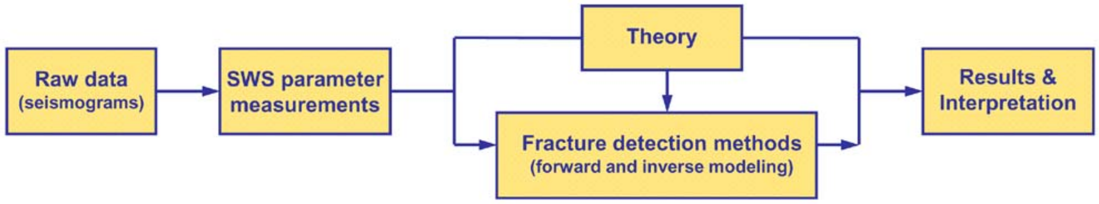

From the raw data of seismograms we need to extract the information we need, more specifically in this case, the measurement of two parameters as the input. From the theory of split shear waves, we develop a forward modeling method to evaluate these two parameters, and an inversion algorithm to estimate the properties of the fractured media. And finally interpretation and any possible implications are made according to the inversion results as well as other information.

Our research group's efforts have shown that shear-wave splitting is an especially useful seismic modeling tool and an ideal method to detect and characterize critically stressed and optimally oriented fractures in the upper crust. Shear-wave splitting parameters (i.e. polarization angle and delay time) are reliable and robust in imaging the subsurface crack geometry and intensity in any fracture-controlled geothermal reservoir (e.g. Lou and Rial, 1997; Vlahovic et al., 2002a,b; Elkibbi and Rial, 2003, 2005; Elkibbi et al., 2004, 2005; Yang et al.,2003, 2005; Rial et al., 2005; Tang et al., 2005, 2006, 2008). Taking into vision all our research group's previous efforts, we aim to develop a processing procedure towards the automatic detection of subsurface fractures in geothermal fields using shear-wave splitting. The approach rests on the integration of techniques recently developed by our research group to process and interpret shear-wave splitting measurements from natural (and injection-induced if available) micro-earthquakes. The final vision is expected to include displaying in real time the seismicity induced by the EGS (engineered geothermal systems) operation, and detecting crack orientation and crack density as the seismic data stream into the seismometers to guide the development and exploitation of geothermal reservoirs. For the time being the software will include the following four major modules to realize the proposed functions respectively as shown in the main flowchart in Figure 5.1.

PICK module: The PICK module is used to pick the P-arrival automatically when a seismic event is detected in the seismogram. The algorithm of P-arrival picking is based on finding the maximum of the ratio of averages in two adjacent windows ("curvature ratio") moving along the seismogram.

LQUAKE module: The LQUAKE module uses all available P-picks detected by the PICK module to calculate the hypocenter and onset time of a seismic event. It uses a standard non-linear inverting algorithm based on Geiger's method with 1-D velocity model. When a 3-D velocity model is available it can still work as well. The above two modules will basically be extracted from Dr. Jonathan Lees' previous work.

Auto_SWS module: This module applies a novel splitting algorithm based on AIC function to measure the two SWS parameters (fast polarization φ and delay time δt) automatically. For a specific seismic event recorded by a specific station, an approximate S-arrival is estimated from the P-arrival picked by PICK module plus the estimated S-P calculated from the length of ray path divided by the virtual velocity. With this estimated S-arrival the new method will measure the two parameters automatically (using the Revised AIC algorithm) over a range of different window lengths encompassing the S-arrival and perform a cluster analysis algorithm to determine the best cluster and take the mean values of the two parameter measurements in this best cluster as the final results.

INVERSION module: This module uses the measurements of the two SWS parameters inside the shear-wave window of each station as input to invert for the crack geometries and density in the vicinity of the station. The basic algorithm is least-squares regression beginning with an initial value of crack density. Given the inverted density a contour of RMS of residue functions constructed on a 2-D plane spanning all possible crack strikes (-90° to 90° by 1°) and dips (-90° to 90° by 1°) will be plotted for polarizations and delay times respectively. Theoretically the pair of strike and dip corresponding to the global minimum in this contour will be taken as the inverted results of crack geometry parameters (i.e. strike and dip).

Picking P-arrivals and Locating an Earthquake

P-arrival Picking

As indicated by the main flow chart in Figure 5.1, we begin the analysis with picking P-wave arrival times and also S-wave arrival times of each seismogram whenever a clear S arrival is available at each station. The automatic P-arrival picking is completed by the PICK module the detailed flow charts of which are depicted in Figures 5.2 and 5.3.

The P-picking should be very fast with good resistance to noise spikes and bad data. Basically one should use the event onset as determined by the envelope detector to provide a preliminary P pick. For a P arrival with clear onset, the pick will be good enough so that it can stay as a final pick after the event location is computed if the residual is sufficiently small. If the detailed picker fails to meet threshold criteria, then this pick would be used as a P pick with a large error to ensure that an entry is made in the pick file (with a relatively large error). This makes it likely that after computing the location, the repicking program can still go back and recover a valid pick for that station.

We had attempted to correct the problem of early picking for signals with high signal/noise ratio but some low frequency noise preceding the P onset. The detection window was shortened in the detection phase and as compensation, the detection threshold was reduced. In addition, a provision was made to capture the earliest peak above the threshold as opposed to the maximum peak in the detection window. At the same time, we had extended the number of sample points included past the detection point for the peak localization so that there is now somewhat more likelihood of making a late pick but some complete misses are improved.

Earthquake Location Program

After P- (and S-) arrivals are picked seismic events are located and the onset time is computed by using a standard iterative non-linear inverting algorithm based on Geiger's method. This is completed in the LQUAKE module with detailed steps shown in the flow charts in Figures 5.4 and 5.5.

LQUAKE does hypocenter location using the basic Geiger's method (e.g. Lee and Stewart, 1981), modified with Levenburg-Marquardt damping as an option. The partial derivatives of travel time with respect to location $\partial t / \partial \bar{x}$ form a matrix and the unknown vector contains the latitude, longitude, depth, and onset time of the earthquake. Before the iteration begins, the initial values of latitude and longitude are set as those of the nearest station (i.e. the one with shortest travel time) and the depth is preset as 6.0 km. In most cases as the iteration proceeds the solution vector will converge until the error is within some preset tolerance. In some cases where the solution doesn't converge (mostly due to the inconsistence of the pick data), however, the program will stop the iteration at a preset number of iterations and output the current results. If S arrivals are also picked and taken into account in addition to P arrivals, this will put more constraint on the inversion problem and usually return with a relatively better location in terms of the location error.

Standard UW style pick files are used for input of phase data that can be generated by the PICK module in previous steps. Results are written back to the hypocenter file in the same pick file format. Each pick file must begin with an "A" line, followed by phase and other data. All control parameters are set in a "setup" file. This file may be specified several ways: (1) by giving a command line argument - in this case, the setup file may have any name; (2) by having a file named "setup.lquake" in the current directory; or (3) by using currently established default.

There are two modes that the program operates in: file mode and stream mode. In file mode, successive command line pick files are processed in succession, and the results are written back to the respective pick files. In this mode, each pick file must contain data for one, and only one, event. In stream mode, LQUAKE reads the standard input for a stream of pick file data, and the results are output to the standard output. In this case, pick files may be concatenated together and the resultant output will be a concatenation of successive event files in the same order as the input. The stream is parceled by strict adherence to the "A" line as being the head of the next event. Thus in stream mode, the input is read until the next "A" lines is encountered, the event processed and written to the standard output, and then the next event in succession is similarly read. This is a very efficient processing method when a large number of events are to be processed repeatedly, and can be stored as a concatenated set of pick files in a single archive file.

LQUAKE needs several tables to run. A station table is needed in the format of the conventional UW style station table. The station table can be specified explicitly in the setup file. In this case, only the stations included in the specified table are available for location calculations. This is one way that a limited subset of stations can be specified for the location. Then a velocity model table is required. The first two lines of this table are set by default as descriptive information that is ignored. The following lines are: depth, P velocity, P error, depth, S velocity, S error in that order for each line where the first "depth" is the layer top for the respective layer, the P velocity of the layer is next, and the error in P velocity for that layer is next. The second "depth" and succeeding values are the same things for the S velocity model. Velocity is in km/sec and depth is in km. A station delay table is optional. If specified, the format should be: station name, followed by P delay, followed by S delay, one line per station. The first two lines are again ignored as descriptive information. Computation errors in location and onset time are evaluated and output too in the resulted pick files.

Automatic Measurement of Shear-wave Splitting Parameters

Introduction

Traditional techniques to extract polarization and delay time information from split seismograms essentially include 1) the visual analysis of two horizontal components and 2) the standard correction method of Silver and Chan (1991), among many other more-or-less similarly disciplined methods (Crampin and Gao, 2006; Gao et al., 2006).

The visual analysis method is usually used to accurately detect the switch in the polarity of the two orthogonally polarized fast and slow shear-waves and to measure the splitting parameters: polarization and delay time. Fast shear-wave polarization angle is measured by interactive rotation of the seismogram until the horizontal particle motion plot shows that fast and slow shear-waves are oriented along the instrument's horizontal components. The angle of rotation from the original polarization direction determines polarization. At the same time, the two shear-wave arrivals, which are often coupled in the original recording, separate out in the time domain and the delay time can then be directly measured.

In the standard correction method, first a shear-wave analysis window is defined, which is usually picked manually. If anisotropy is present, the particle-motion within this window will be elliptical. Second, a grid search of polarization and delay time is performed where both horizontal components are rotated by polarization and one component is lagged by delay time. The result which has the lowest second eigenvalue of the corrected particle-motion covariance matrix indicates linear particle motion after correction and is the solution which best corrects the splitting. An F-test is then used to calculate the 95% confidence interval for the optimal values for polarization and delay time. After the splitting correction has been applied the method requires that the corrected waveforms in the analysis window match. The second eigenvalue of the particle motion covariance matrix provides a measure of this match. The smaller the second eigenvalue, the better the match (Teanby et al., 2004). A good result will have a unique solution. Criteria for reliable results are discussed in Savage et al. (1989) and Silver and Chan (1991).

Both methods require the manual selection of an appropriate time window by the operator which is time consuming, introduces subjectivity, and to some extent influences the results. Automatic detection of shear-wave splitting was attempted by Savage et al. (1989). The disadvantage of their method is that they do not address the effect that different shear-wave analysis time windows can have on the results. Teanby et al. (2004) used cluster analysis to remove the subjectivity of window selection. However, their method needs manual quality control with diagnostic plot, which can still be human biased and laborious.

Current seismic deployments aim at multiple geophone arrays and longer recording times. Correspondingly, data volumes from microseismicity and teleseismicity are growing quickly in recent years. These large datasets can provide insights into lithological properties, making it possible to constrain the evaluation of subsurface fracturing and intrinsic anisotropy. But manual analysis of each event may easily become a tedious job, consequently impaired by operator's subjective errors. These facts are forcing seismologists to invent relatively automated approaches with as little human involvement as possible.

Here we want to propose a novel method of automatic detection of shear wave splitting parameters which actually extends the idea of automated window selection by Teanby et al. (2004) and integrates a different measuring technique and cluster analysis algorithm. This method inherits the advantage of high data processing speed of automated cluster analysis algorithms, while the integrated measuring technique avoids the subjectivity of window selection and manual quality control, consequently improving the accuracy of splitting parameter estimates and as a result providing a convenient approach to process such huge seismic datasets automatically and objectively. In the following sections we will discuss the shear-wave analysis window selection and compare two different measuring techniques with the Auto_SWS (employing Revised AIC) algorithm, and then show the clustering algorithm and an optimized cluster choosing procedure as well as the best estimate selection process. Following these the results of our Auto_SWS algorithm are highlighted using observational data collected from The Geysers and Coso, CA and Hengill geothermal field, Iceland. We will illustrate how the reliability of the automated estimates can be accurately evaluated by comparing with parameters obtained by a skilled operator.

Windows Selection

Finding the optimal shear-wave time window for the detection of SWS parameters depends on critical factors such as adequate S/N ratio in the shear-wave, and enough length to include several periods of the dominant frequency. It is however quite time consuming and subjective to find the optimal window manually by visual inspection. On the other hand, it is well known that the actual shear-wave splitting process is stable with respect to the noise (Teanby et al., 2004). Therefore, it is very important to ensure that the measured splitting parameters are stable over a wide range of different window lengths and intervals. This stability guarantees the robustness of measurement and minimizes the effects of noise. The method introduced here achieves this by considering a large number of analysis windows to look for stable regions in the space of solutions, that is, in polarization and time delay parameter space.

The method proceeds as follows: first, a set of shear-wave analysis time windows are constructed as illustrated in Figure 5.6. The beginning of the window is selected at T_{begin} which will vary from T_{begin_0} to T_{begin_1} with N_{begin} steps of dT_{begin} length. Similarly, the end of the window is selected at T_{end} varying from T_{end_0} to T_{end_1} with N_{end} steps of dT_{end} length. The total number of analysis windows N_{total} is thus

$$N_{total} = N_{begin} \times N_{end} \qquad (1)$$

where T_{begin} and T_{end} are both defined relative to the onset of the shear-wave. Please refer to Table 1 for typical values of the parameters used for window selection when applied on microseimic datasets.

AIC Picker Algorithm

Once the shear-wave analysis windows are selected, the measuring algorithm used to determine polarization and delay time is applied on each window. We estimate the values of polarization and delay time by making use of existing automatic wave arrival picking techniques. The algorithm used is the AIC (Akaike Information Criteria) picker by Maeda (1985) which calculates the AIC function directly from the seismograms. The onset is at the point corresponding to the minimal AIC value. For the seismogram $x[k]$ (with $k = 1, 2, \ldots, N$) of length N, the AIC value at the kth point is defined as

$$AIC(k) = k \times \log\{\mathrm{var}(x[1,k])\} + (N-k-1) \times \log\{\mathrm{var}(x[k+1,N])\} \qquad (2)$$

where k ranges through all of the seismogram samples.

The idea of this algorithm is to use the well known AIC picking algorithm to detect significant shear-wave arrival time difference between the two horizontal components in a rotated coordinate system. Here "significant" means the difference between the arrival times of the fast and slow shear-waves is within 10 to 60 sampling intervals. In order to search the entire coordinate span, the algorithm rotates the two horizontal components of the seismogram simultaneously from 1 to 180 degrees by one-degree increment. During each incremental rotation of the coordinate system, the variance of the interval between fast and slow arrival times on the slow component is calculated. The polarization will be the angle corresponding to the rotated coordinate in which the differential arrival time is significant AND the variance on the slow component reaches its minimum (meaning the slow component within that interval is most quiescent). Figure 5.7 shows the results after applying AIC picker to a seismogram recorded in the original coordinates from The Geysers geothermal field, CA.

Illustrative results of the AIC picker algorithm are shown in Figure 5.8. As indicated by the vertical line, the variance in interval [86,112] reaches the minimum at 122 degrees among all the rotated coordinates. Therefore, for this seismogram we obtain that the polarization is 122 degrees CW from North, and the delay time is 26 sample intervals. When there is more noise than signal or multiple seismic phases in the time window of the seismogram, the S/N ratio in the seismogram will affect the accuracy of the AIC picker to some extent. In this circumstance a global minimum indicating the shear-wave arrival will not be guaranteed (Zhang et al., 2003). In order to further improve the algorithm, we check every AIC function plot for each seismogram to determine specific problems caused by using the simple AIC picker technique. Figure 5.9 shows that the method sometimes yields erroneous answers to the arrival times for seismograms with low S/N ratio.

The problem in Figure 5.9 is that before the slow wave arrives, the north component is disturbed, probably by the arrival of a scattered wave, and the AIC picker regards this disturbance as a real wave according to the position of its global minimum value. Nevertheless, the AIC picker does give us a clue about the onset of the real wave, that is, the arrival time is associated with the relative local minima of the AIC function, as indicated by the vertical dashed lines in Figure 5.9. In order to avoid that scattered wave or noise disturbance being regarded as a signal, we take the global minimum value as well as other local minima into account simultaneously while rotating the components of the seismogram.

Cluster Analysis

Once the automatic measuring algorithm is applied on each shear-wave analysis window, it results in a set of N_{total} pairs of estimates of polarization and delay time. With the purpose of varying the analysis windows and looking for robust values in polarization and delay time, we plot the N_{total} pairs of polarization and delay times in a 2D plane. These estimates are supposed to condense into point groups or tight clusters as shown in Figure 5.10.

Since the polarization and delay time are in different scale units (degree and sampling interval), we need to normalize the data in order to eliminate different weight effects on the polarization and delay time caused by the clustering analysis algorithm. Based on our microearthquake datasets, we define the standardized range for polarization and delay time as 180 degrees and 60 sampling intervals respectively. Scaling by this variable range has performed very well in many clustering applications (Teanby et al., 2004; Everitt et al., 2001; Milligan and Cooper, 1985, 1988).

Robust results should be grouped into a tight cluster of close points and then a technique is required to identify these clusters for the reason of automation. Here we adopt the so-called Density-Based Scan Algorithm with Noise (DBSCAN) (Ester et al., 1996) to identify clusters. DBSCAN typically regards clusters as dense regions of objects in the data space that are separated by low density regions. DBSCAN is a density-based clustering technique which starts the search from an arbitrary object, and if the neighborhood around it within a given radius (*Eps*) contains at least the preset minimal number of objects (*MinPts*), this object is marked as a core object, and the search recursively continues with its neighborhood objects and stops at the border objects whereas all the points within the cluster must be in the neighborhood of at least one of its core objects. Another arbitrary ungrouped object is then selected and the process is repeated until all data points in the dataset have been placed in one of the clusters identified. All the non-core objects (outliers) which are not in the neighborhood of any of the core objects are labeled as noise. DBSCAN doesn't need the number of final clusters to be given in advance and it automatically detects dense regions and its output is the natural number of clusters (Daszykowski et al., 2001). Four clusters are shown in Figure 5.10 represented by different colors.

Once the clusters are successfully identified by the DBSCAN algorithm, we need to determine the optimal cluster, and then the best estimate from the optimal cluster. The criterion to determine the optimal cluster depends on the number of data points and the variance within each cluster. To implement the criteria, we define $N_{cluster\_\min}$ such that any cluster containing less than $N_{cluster\_\min}$ data points is regarded as noise. $N_{cluster\_\min}$ corresponds to approximately a cycle's worth of points, which is usually less than the total number of windows N_{total} divided by the number of clusters $N_{cluster}$.

The within cluster variance σ_j^2 is calculated according to

$$\sigma_j^2 = \frac{\sum_{i=1}^{N_j} (\delta t_i^{(j)} - \bar{t}_{(j)})^2 + \sum_{i=1}^{N_j} (\phi_i^{(j)} - \bar{\Phi}_{(j)})^2}{N_j} \qquad (3)$$

where $\delta t_i^{(j)}$ and $\phi_i^{(j)}$ are the *i*th results of delay time and polarization respectively which belong to cluster *j* and N_j is the total number of data points in cluster *j*. The average position of data points within each cluster is simply defined as

$$\bar{t}_{(j)} = \frac{\sum_{i=1}^{N_j} \delta t_i^{(j)}}{N_j}$$
$$\bar{\Phi}_{(j)} = \frac{\sum_{i=1}^{N_j} \phi_i^{(j)}}{N_j} \quad (4)$$

Therefore, the optimal cluster is found to be the cluster with the smallest variance (σ_j^2). The best estimates are taken as the mean values of δt and ϕ in the optimal cluster. The best estimates from the optimal cluster are illustrated with crosses in Figure 5.10. And the results from an example of real seismic event are shown in Figure 5.11.

Two flow charts depicted in Figures 5.12 and 5.13 have been designed to describe in detail every step of the Auto_SWS program introduced in this section. The Revised AIC Picker serving as the measuring algorithm is performed for each specific analysis window as shown in the red rectangle (with details in Figure 5.13) in Figure 5.12.

Other Related Issues

As we have mentioned before, slight changes in the position of analysis window may cause very different results due to the cycle skipping effect, accordingly the selection of shear-wave analysis window turns out to be a step requiring special attention (Teanby et al,. 2004). Important parameters include N_{begin}, N_{end}, dT, T_{begin_1} and T_{end_0}. Large N_{begin} and N_{end}, small dT should provide abundant space for the grid search by the automatic measuring algorithm, however it also requires more computational time. Since the SWS parameter estimates are much more sensitive to the window start than to the window end, we have typically chosen N_{end} as 20-30 times larger than N_{begin} in order to maintain an appropriate balance between accuracy and speed.

The distance between the fast shear-wave arrival and the closest window start/end is controlled by T_{begin_1} and T_{end_0} which defines the minimal analysis window length. The measuring algorithm (Revised AIC Picker) requires a relatively clear shear-wave arrival and separates S phases from any other possible phases. To satisfy these requirements, we have defined 50 sample intervals to be the minimal window length. dT is relatively not a critical parameter in this approach, as long as there are large enough ranges of analysis windows that include the duration of shear-wave energy envelope, which guarantees the reliability of the final results.

Although this new method is much less sensitive to the influence of cycle skipping than most other automated methods, the cycle skipping and/or window dependence effects still remain a severe problem for band limited data. It may also affect the comparison results of the first and the second best clusters, where the first two best clusters usually provide 95% of correct estimates during our application to the selected geothermal datasets. If the first is obviously better (in terms of both the point number and the variance within the cluster) than the second then the result is reliable, otherwise the result might be affected by cycle skipping.

Similar to other automated methods, the Auto_SWS method still can not discern perfectly between null and valid measurements. However, several features of our program can help us overcome this problem. The first one is setting the upper and lower limits for the intervals of delay time ranging from 10 to 60 sampling intervals. Another feature is the system of cluster identification. Null measurements tend to form poorly condensed or incompact cluster, leading to totally unconstrained polarization and a large spread in delay time, in other words, showing a large scattering of clusters in the 2D plan. It will consequently be rejected by the cluster identification and the interval length control.

Justification of the Method

Availability of previous reliable manual shear-wave splitting measurements, diverse subsurface structural settings and seismic data of different levels of quality have made it possible and worthwhile to test and justify this new Auto_SWS algorithm using various seismic datasets. We have used totally eighty SWS events selected from three different locations (Coso and The Geysers in CA, Hengill in Iceland) to apply the new algorithm on.

Figure 5.14 summarizes the comparison between the manual results and the results from three different measuring algorithms. Figure 5.14(A) is obtained from the traditional cross-correlation method. However, the results do not satisfy the requirements for reliable parameter estimates. The proportion of unreliable estimate results after implementing the AIC picker is somewhat reduced as shown in Figure 5.14(B), although still about one third of these estimates are lying outside of error tolerance. To achieve better reliability, the AIC picker is revised to serve as the key part of our Auto_SWS algorithm, which turns out to work best as indicated by the comparison between the manual measuring results and the automated estimates shown in Figure 5.14(C). In this last test 76/80 of polarization estimates and 70/80 of delay time estimates are inside the tolerance limits now.

One more way of justification of the new method is to compare the results of manual measurements with the results obtained by the new method when it is applied on the seismic data recorded at a single station where usually data of different quality levels are available. For this purpose two stations deployed in Hengill in 2005 (H71 and H75) are selected and we have used the Auto_SWS method to measure the parameters of all shear-wave splitting events recorded at these two stations respectively. The comparisons are plotted in Figure 5.15 for H71 and in Figure 5.16 for H75. Basically for both parameters the automatic method yields satisfying measuring results in terms of the percentage of data points lying inside the acceptable error tolerance and the similarity between the two rose diagrams in the lower panel of the figures. We also invert both sets of parameter measurements for fracture attributes associated with these two stations, and the results are summarized in Table 2. The two sets of inversion results can be basically regarded as almost identical to each other in terms of strike and dip. The relatively larger difference in crack density can be explained by the fact that the automatically measured delay times are generally larger than the manual results as clearly depicted in Figures 5.15 and 5.16.

Considering the fact that all seismometers deployed in Hengill were placed on or near the surface of the ground, we are fairly confident in saying that this new automatic method will be more powerful if applied on shear-wave splitting events well recorded by downhole instruments (like in Coso and The Geysers, CA), and we can anticipate an overall percentage of satisfactory measurements to be approximately 10% higher (expectedly ~ 85%).

Inverting for Crack Geometry and Intensity

Shear-wave splitting parameters (polarization and delay time) observed and measured in all previous steps can now be used simultaneously to invert for fracture orientation and intensity of subsurface fracturing systems. The inverse modeling method used here is adopted from Yang (2003) and Yang et al. (2005). The flow chart of the numerical procedure is depicted in Figure 5.17, and Figures 5.18 to 5.20 are showing all of the detailed steps involved in each contributing subroutine.

References

Crampin, S., and Gao, Y., 2006. A review of techniques for measuring shear-wave splitting above small earthquakes. *Phys. Earth Planet. Interiors*, **159**, 1-14.

Elkibbi, M. and Rial, J.A., 2003. Shear-wave splitting: an efficient tool to detect 3D fracture patterns at The Geysers, California. *Proc. Geothermal Reservoir Engineering*, Stanford, **28**, 143-149.

Elkibbi, M., Yang, M., and Rial, J.A., 2004. Imaging crack systems in The Geysers with shear-wave splitting. *Geothermal Resources Council (GRC) Transactions*, **28**, 789-800.

Elkibbi, M., Yang, M., and Rial, J.A., 2005. Crack-induced anisotropy models in The Geysers geothermal field. *Geophys. J. Int.*, **162**, 1036-1048.

Elkibbi, M. and Rial, J.A., 2005. The Geysers geothermal field: Results from shear-wave splitting analysis in a fractured reservoir. *Geophys. J. Int.*, **162**, 1024-1035.

Ester, M., Kriegel, H.-P., Sander, J., and Xu, X., 1996. A density-based algorithm for discovering clusters in large spatial databases with noise. *Proc. 2nd Int. Conf. on Knowledge Discovery and Data Mining* (KDD ’96), Portland, Oregon, AAAI Press.

Everitt, B., Landau, S., and Leese, M., 2001. *Cluster Analysis*, 4th ed., Edward Arnold, London.

Gao, Y., Hao, P., and Crampin, S., 2006. SWAS: A shear-wave analysis system for semi-automatic measurement of shear-wave splitting above small earthquakes. *Phys. Earth Planet. Interiors*, **159**, 71-89.

Lee, W. H. K. and Stewart, S.W., 1981. *Principles and applications of microearthquake networks*, Advances in Geophysics supplement 2. Academic Press, New York.

Lou, M. and Rial, J.A., 1997. Characterization of geothermal reservoir crack patterns using shear-wave splitting. *Geophysics*, **62**, 487-495.

Maeda, N., 1985. A method for reading and checking phase times in auto-processing system of seismic wave data. *Zisin=Jishin,* **38,** 3, 365-379.

Milligan, G. W., and Cooper, M. C., 1985. An examination of procedures for determining the number of clusters in a data set. *Psychometrika*, **50**, 159-179.

Milligan, G. W., and Cooper, M. C., 1988. A study of variable standardization. *Journal of Classification*, **5**, 181-204.

Rial, J.A., Elkibbi, M., and Yang, M., 2005. Shear-wave splitting as a tool for the characterization of geothermal fractured reservoirs: Lessons learned. *Geothermics*, **34**, 365-385.

Savage, M., Shih, X., Meyer, R., and Aster, R., 1989. Shear-wave anisotropy of active tectonic regions via automated S-wave particle motion. *Bull. Seismol. Soc. Am.*, **165**, 279-292.

Silver, P. G., and Chan, W. W., 1991. Shear-wave splitting and subcontinental mantle deformation. *J. Geophys. Res*., **96,** 16429-16454.

Tang, C., Rial, J. A., and Lees, J. M., 2005. Shear-wave splitting: A diagnostic tool to monitor fluid pressure in geothermal fields. *Geophys. Res. Lett.*, **32**, L21317, doi:10.1029/2005GL023551.

Tang, C., Rial, J. A., Lees, J. M., and Elkibbi, M., 2006. Shear-wave splitting observations and measurements at the Geothermal Field at Hengill, Iceland. *Proc. Geothermal Reservoir Engineering,* Stanford, **31**, 512-517.

Tang, C., Rial, J. A., and Lees, J. M., 2008. Seismic Imaging of the Geothermal Field at Krafla, Iceland Using Shear-wave Splitting. *J. Volcanol. Geothermal Res.,* **176(2)**, 315-324, doi:10.1016/j.jvolgeores.2008.04.017.

Teanby, N. A., Kendall, J-M., and van der Baan, M., 2004. Automation of shear-wave splitting measurements using cluster analysis. *Bull. Seismol. Soc. Am.*, **94**, 453-463.

Vlahovic, G., Elkibbi, M., and Rial, J.A., 2002a. Shear-wave splitting and reservoir crack characterization: the Coso geothermal field. *J. Volcanol. Geothermal Res.*, **120**, 123-140.

Vlahovic, G., Elkibbi, M., and Rial, J.A., 2002b. Temporal variations of fracture directions and fracture densities in the Coso geothermal field from analyses of shear-wave splitting. *Proc. Geothermal Reservoir Engineering*, Stanford, **27**, 415-421.

Yang, M., 2003. *Inversion of shear-wave splitting data in geothermal reservoirs*, Master's thesis. University of North Carolina, Chapel Hill, NC.

Yang, M., Elkibbi, M., and Rial, J.A., 2005. An inversion scheme to model subsurface fracture systems using shear wave splitting polarization and delay time observations simultaneously. *Geophys. J. Int.*, **160**, 939-947.

Zhang, H., Thurber, C., and Rowe, C., 2003. Automatic p-wave arrival detection and picking with multiscale wavelet analysis for single-component recordings. *Bull. Seismol. Soc. Am.*, **93**, no. 5, 1904-1912.

Table 5.1. Suggested values of parameters used for the automatic detection code in this study.

Parameter	Value
T_{begin_1}	50 samples before shear wave pick
T_{end_0}	50 samples after shear wave pick
dT_{begin}	25 samples
dT_{end}	10 samples
N_{begin}	3
N_{end}	20
Eps	0.8
MinPts	10
$N_{cluster\_\min}$	25

Table 5.2. Comparison of inversion results from SWS measurements obtained by manual and automatic methods for two selected stations in Hengill.

Station ID	Crack Strike (Degree)	Crack Dip (Degree)	Crack Density	Goodness of Fit (%)
H71 (man.)	27	89	0.048	93.79
H71 (auto.)	26	88	0.066	90.64
H75 (man.)	31	-87	0.043	81.34
H75 (auto.)	7	-82	0.051	73.86

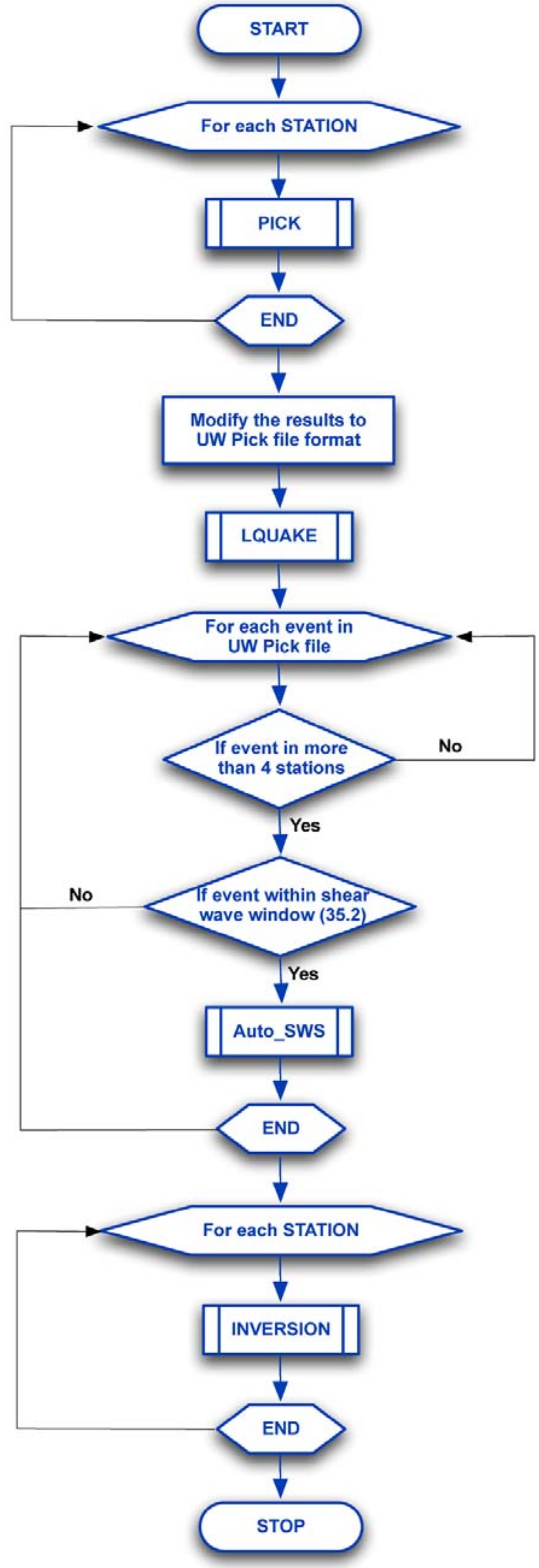

Figure 5.1. Main flowchart of the processing procedure.

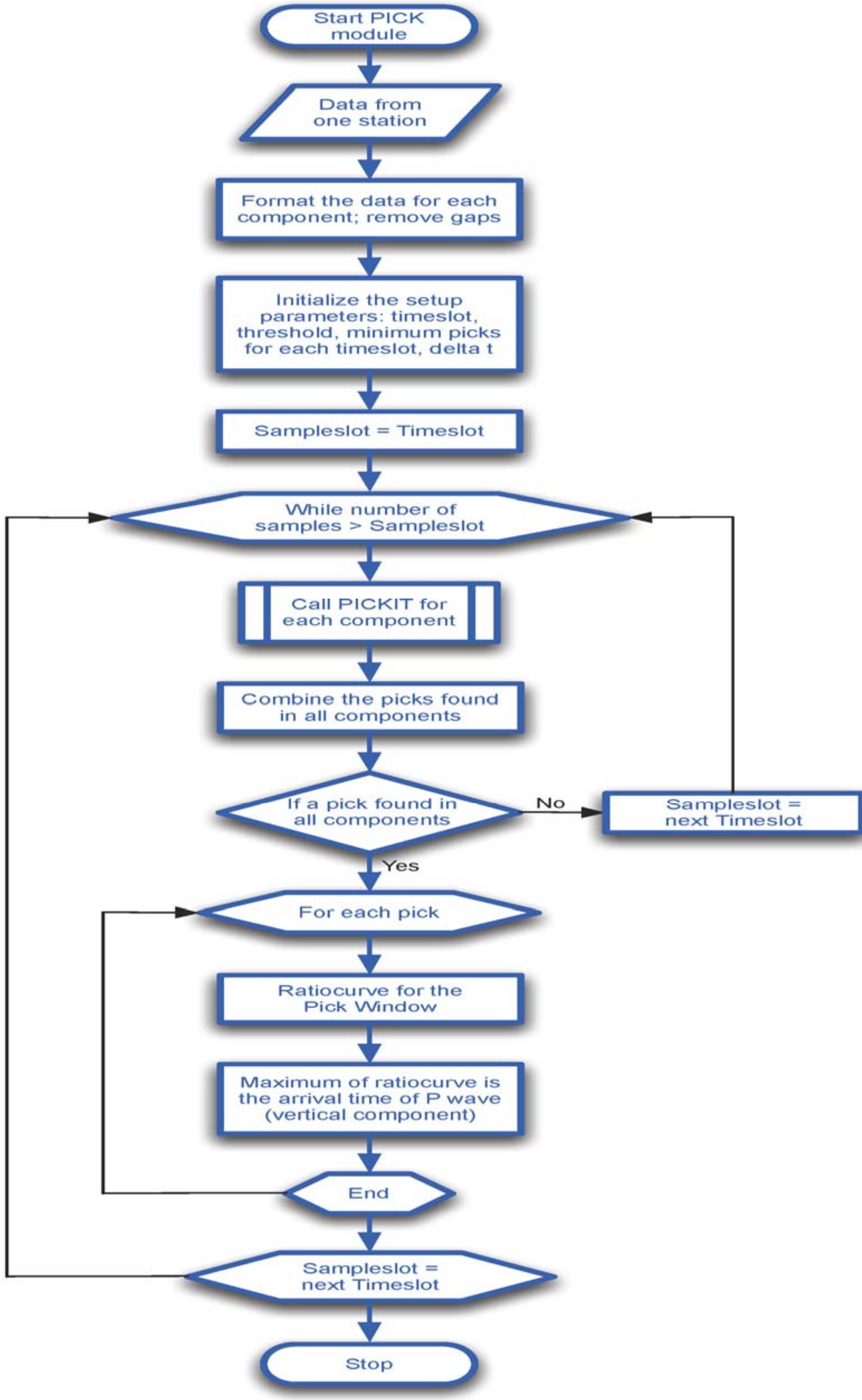

Figure 5.2. Flowchart of the PICK module.

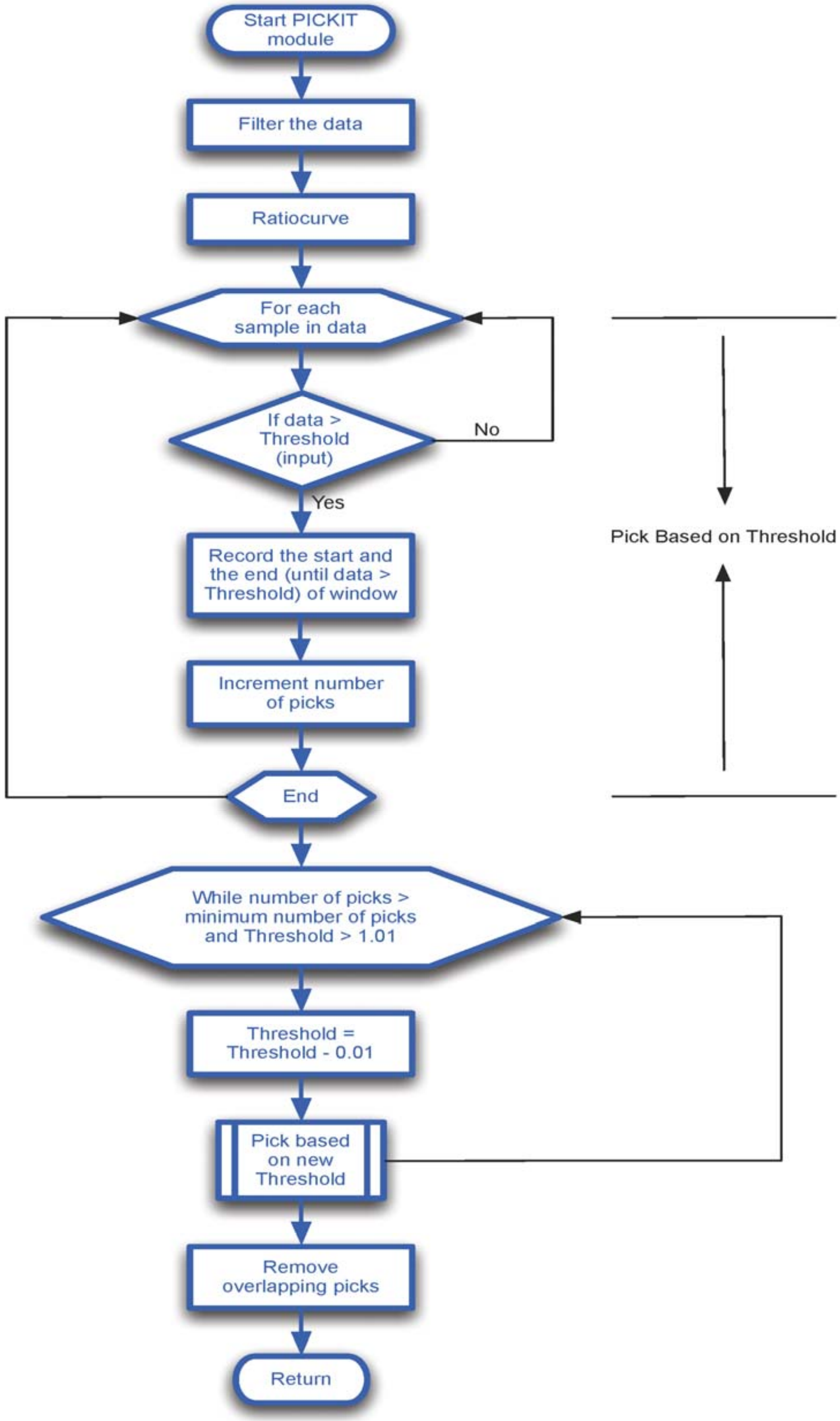

Figure 5.3. Flowchart of the PICKIT subroutine.

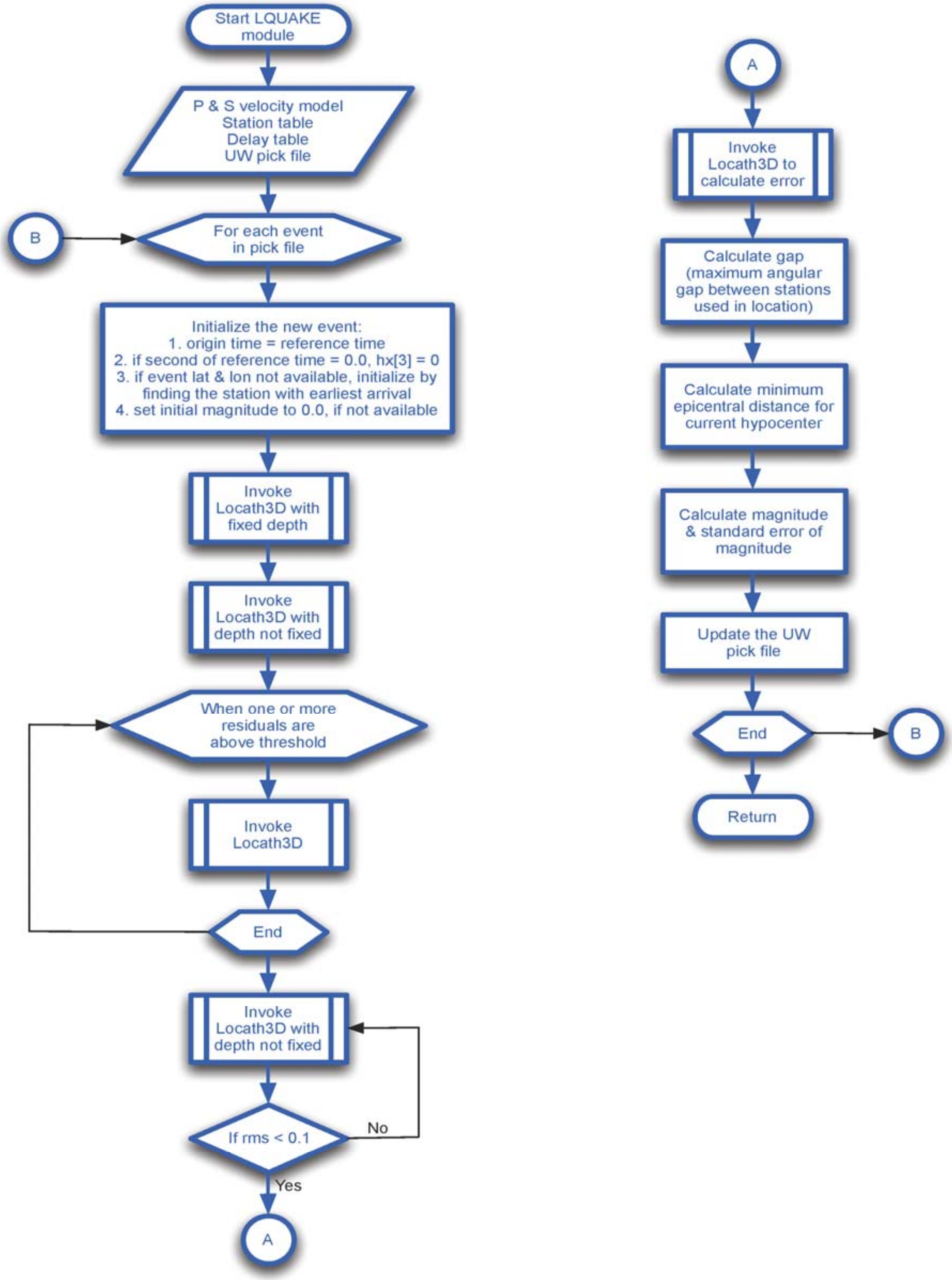

Figure 5.4. Flowchart of the LQUAKE module.

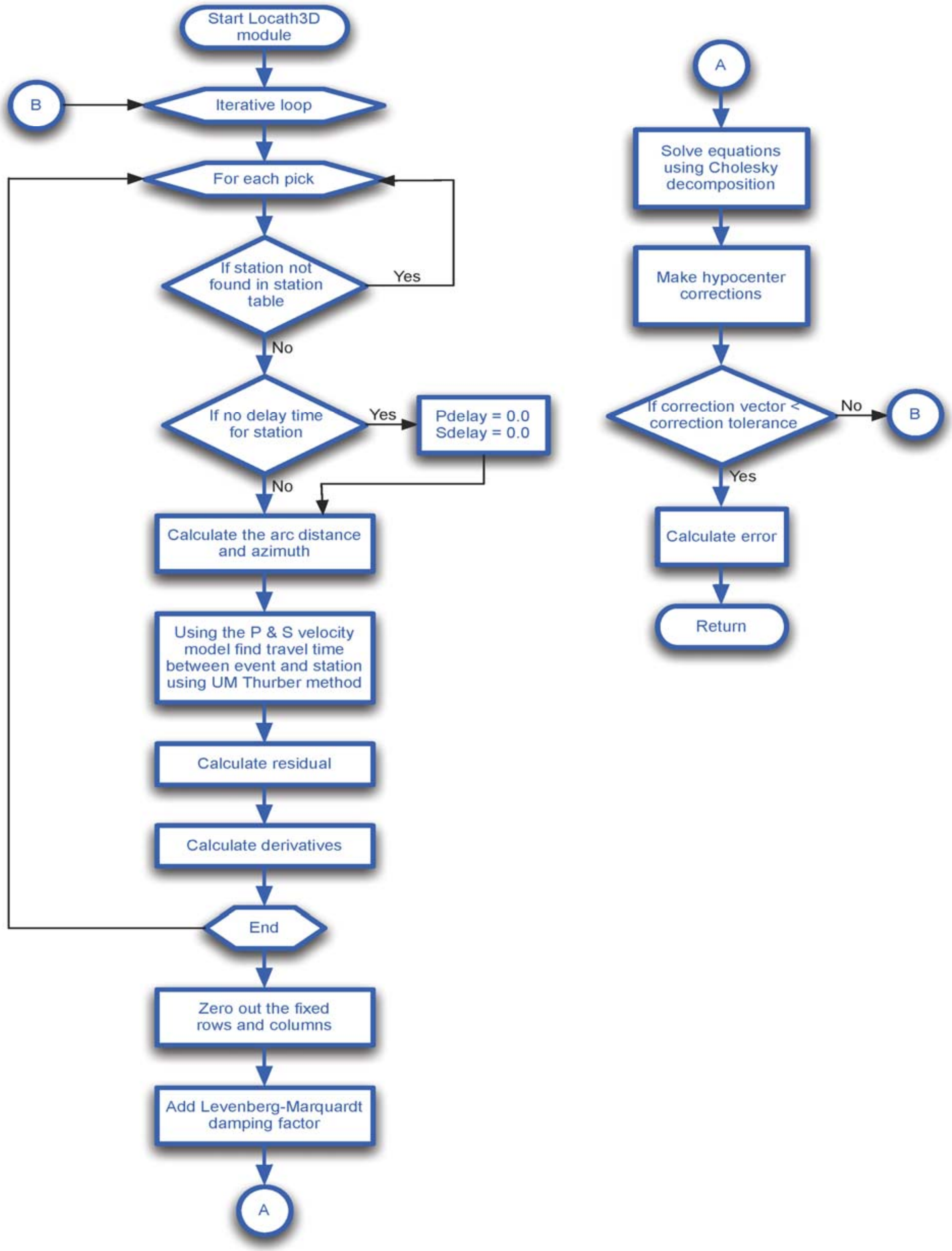

Figure 5.5. Flowchart of the Locath3D subroutine.

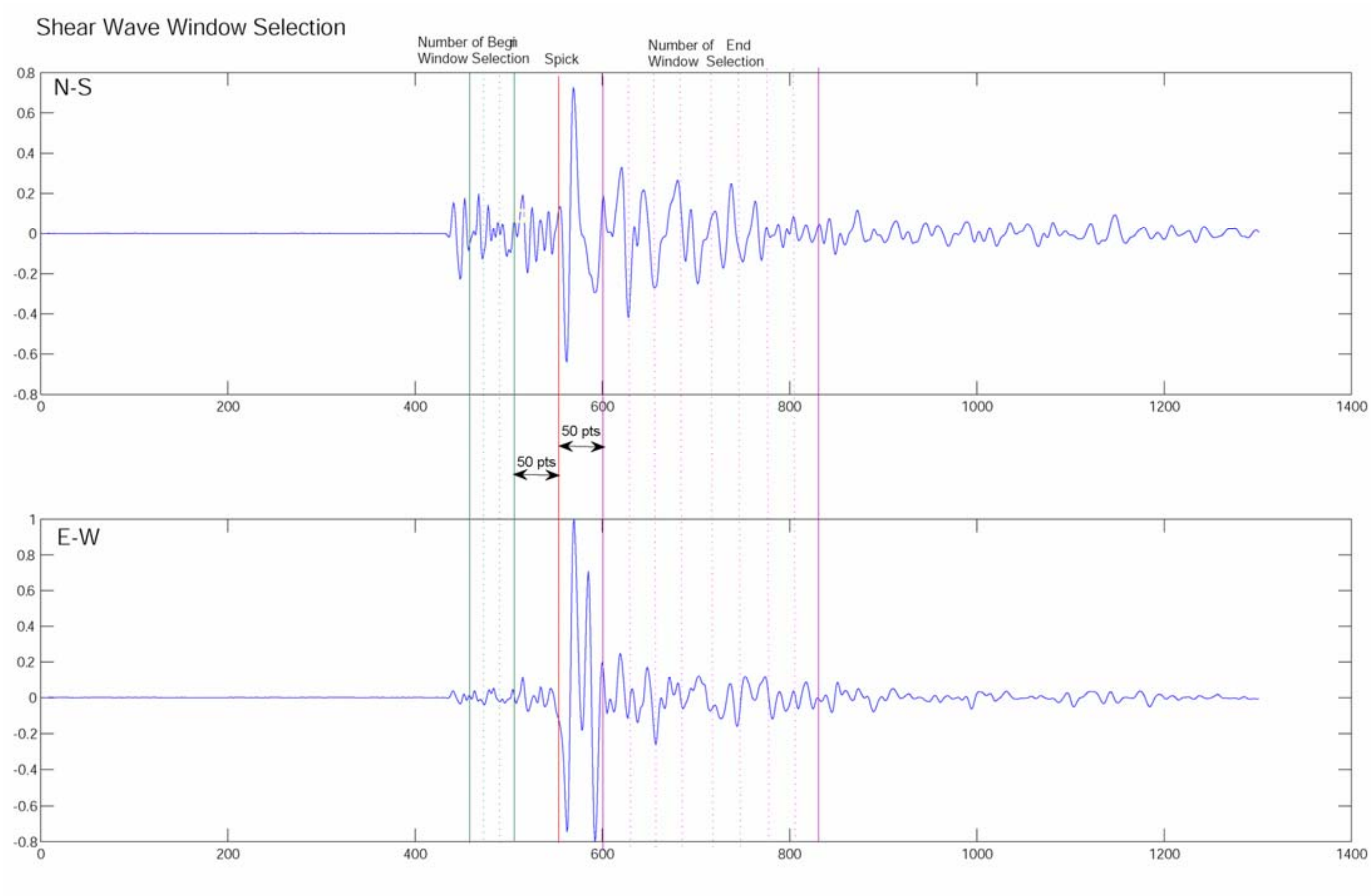

Figure 5.6. An example from The Geysers, CA showing the process of analysis windows selection. The horizontal axis is in number of sample intervals. The red line indicates the shear wave onset. The solid green line indicates the start of shear wave analysis window, while dashed green lines indicate a number of possible window starts. Similarly, the purple lines indicate the window ends. The distance between the closest window start/end and shear wave arrival is 50 sample intervals.

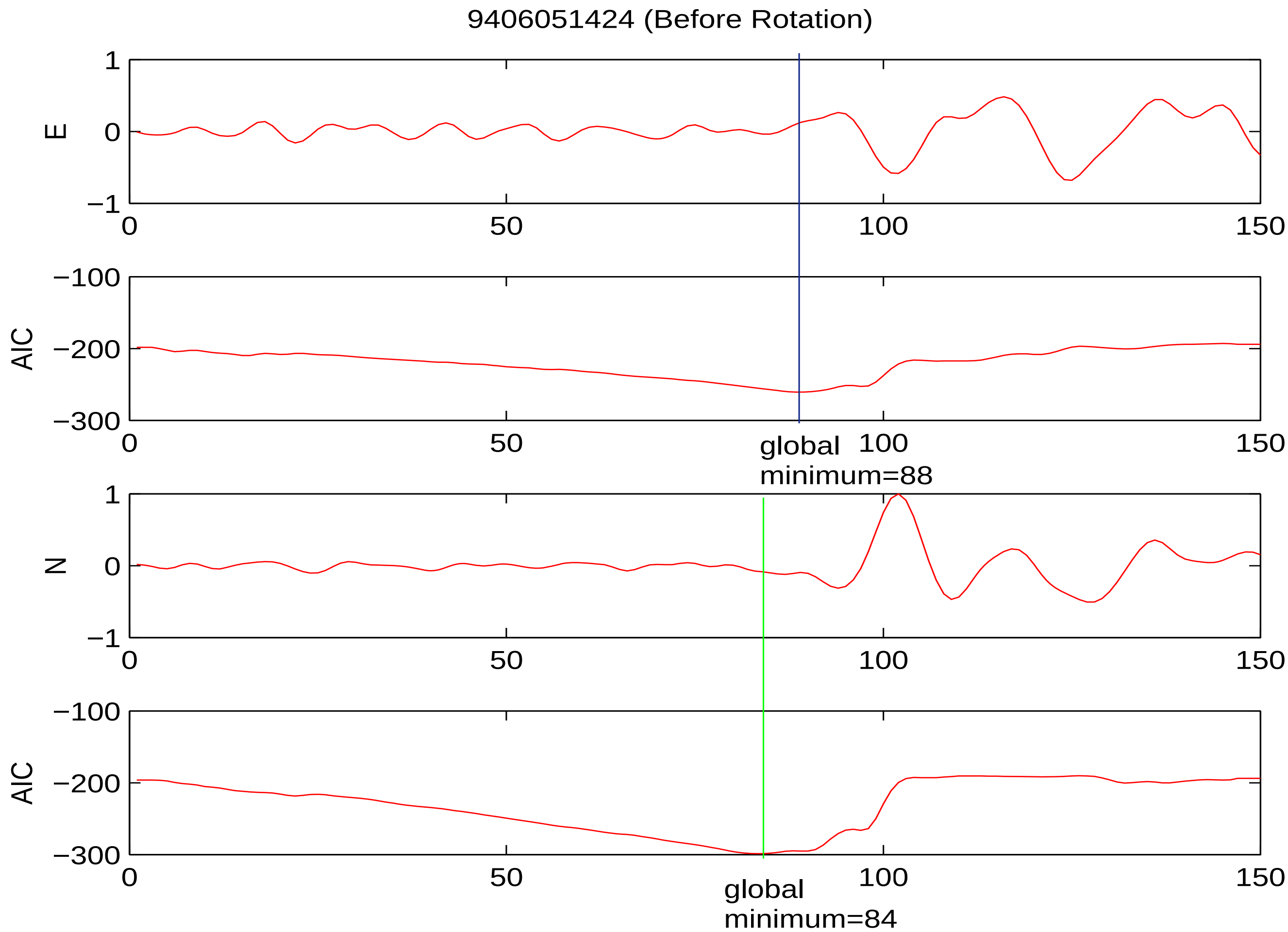

Figure 5.7. The AIC function is calculated for both horizontal components from a real seismogram in the original coordinate. The vertical lines indicate the onset times of the waves. The differential arrival time is not significant (<10 samples) in this coordinate.

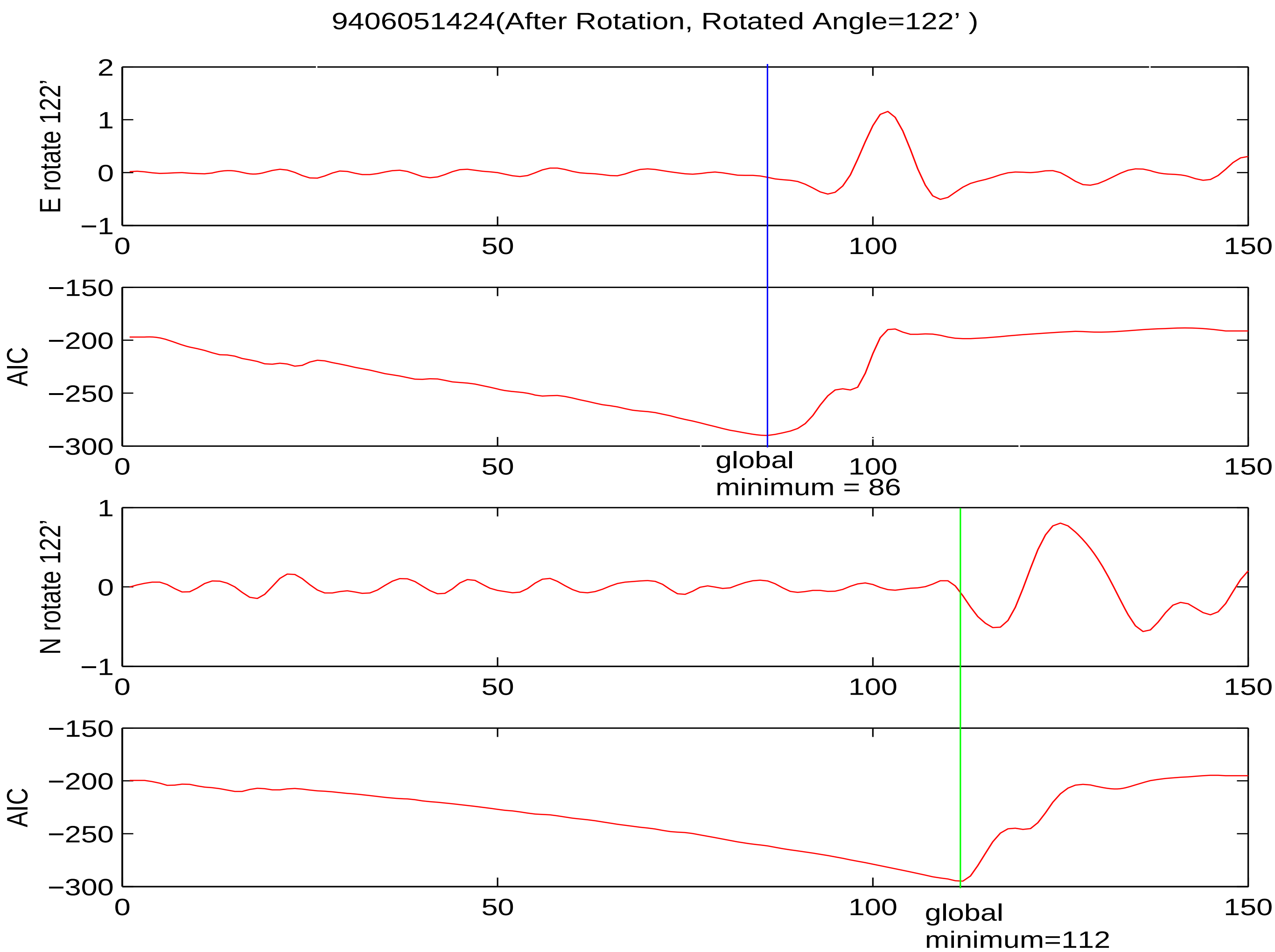

Figure 5.8. Seismograms from Figure 5.7 in a rotated coordinate system. The difference between two arrival times of the two components is 26 sampling intervals, and the angle rotated is 122 degrees.

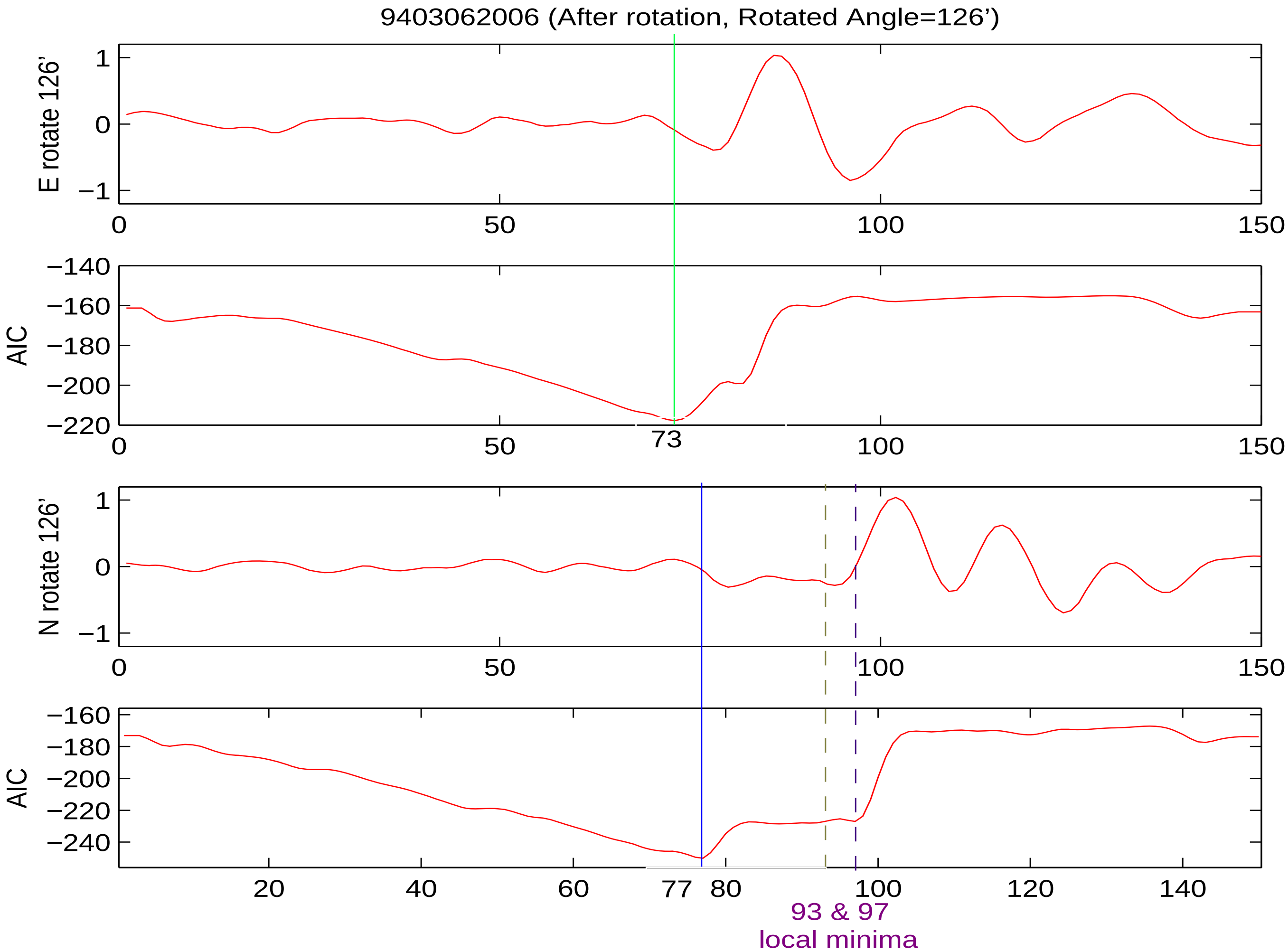

Figure 5.9. The calculated AIC function for both horizontal components from another real seismogram. The green and blue vertical lines indicate the onset times of the waves defined by the global minima of the AIC function, while the purple and yellow dash lines represent the possible onset times suggested by some other local minima.

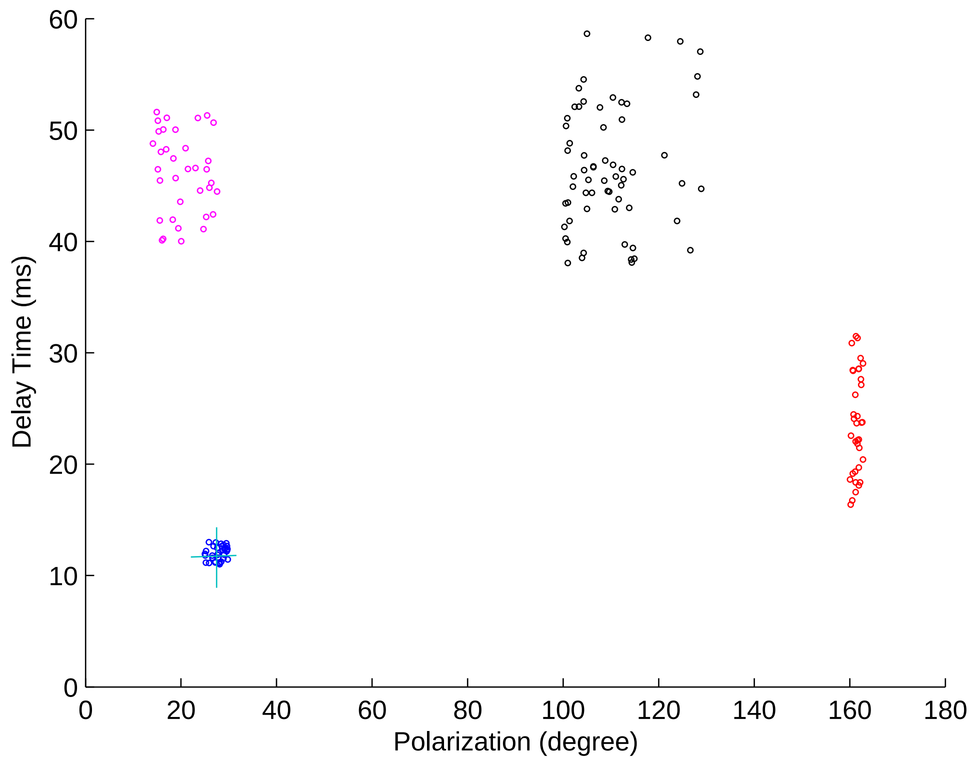

Figure 5.10. Measurements of delay time and polarization from three hundred different analysis windows of synthetic data. The measurements condense into tight clusters of points. Many points in the clusters lie on top of each other because the delay time and polarization are found to be identical. Different colors represent different clusters.

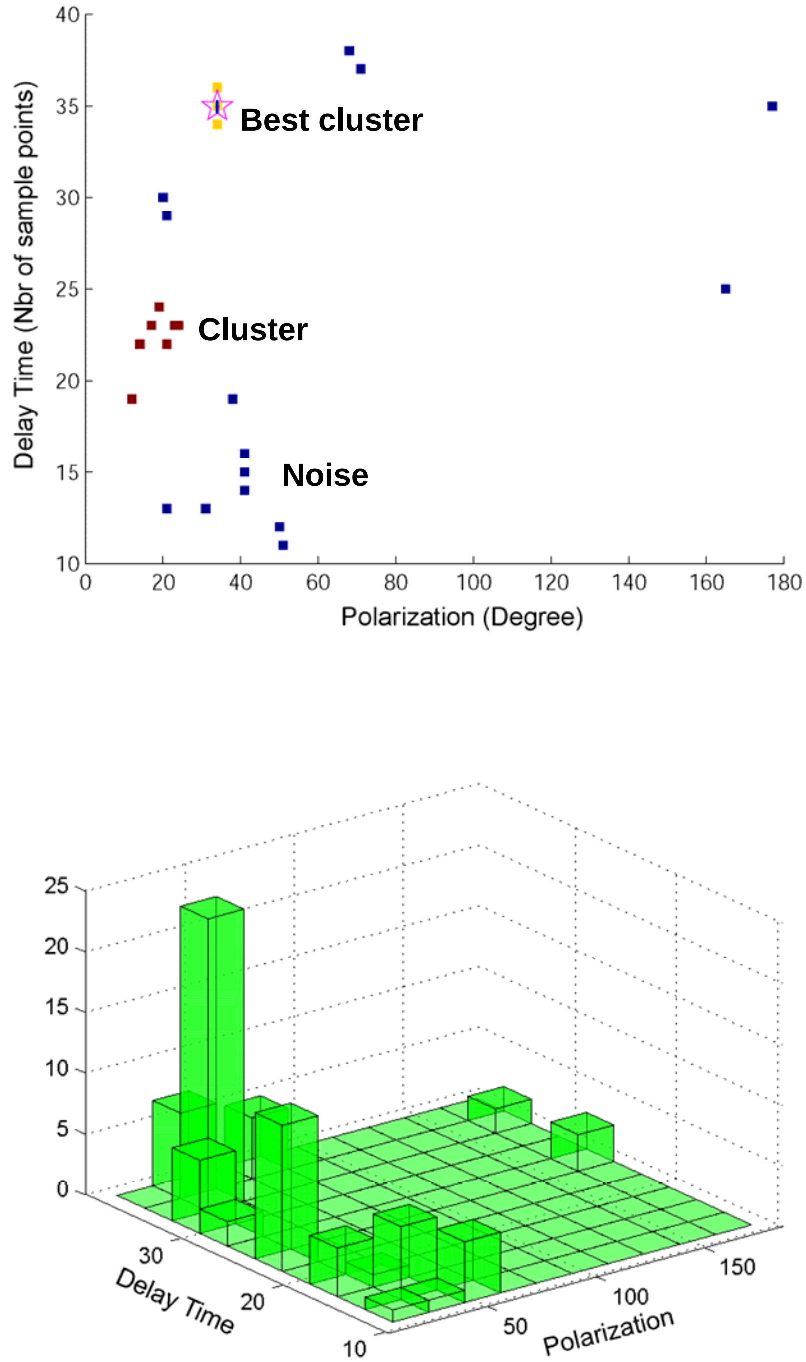

Figure 5.11. Results from an example of Hengill event. The upper panel shows that two different clusters represented by two colors (yellow and brown) are identified by the DBSCAN algorithm, with the outliers indicated by blue color being regarded as noise. In this example, the final automatic estimate from the best cluster (the star inside the yellow cluster) agrees very well with the manual measurements (33 degrees, 35 sample intervals vs. 34 degrees, 37 sample intervals). The lower panel shows the histogram of all possible pairs of SWS measurements. The final best estimate corresponds with no surprise to the highest cube indicating the biggest number of repetitions (i.e. highest redundancy).

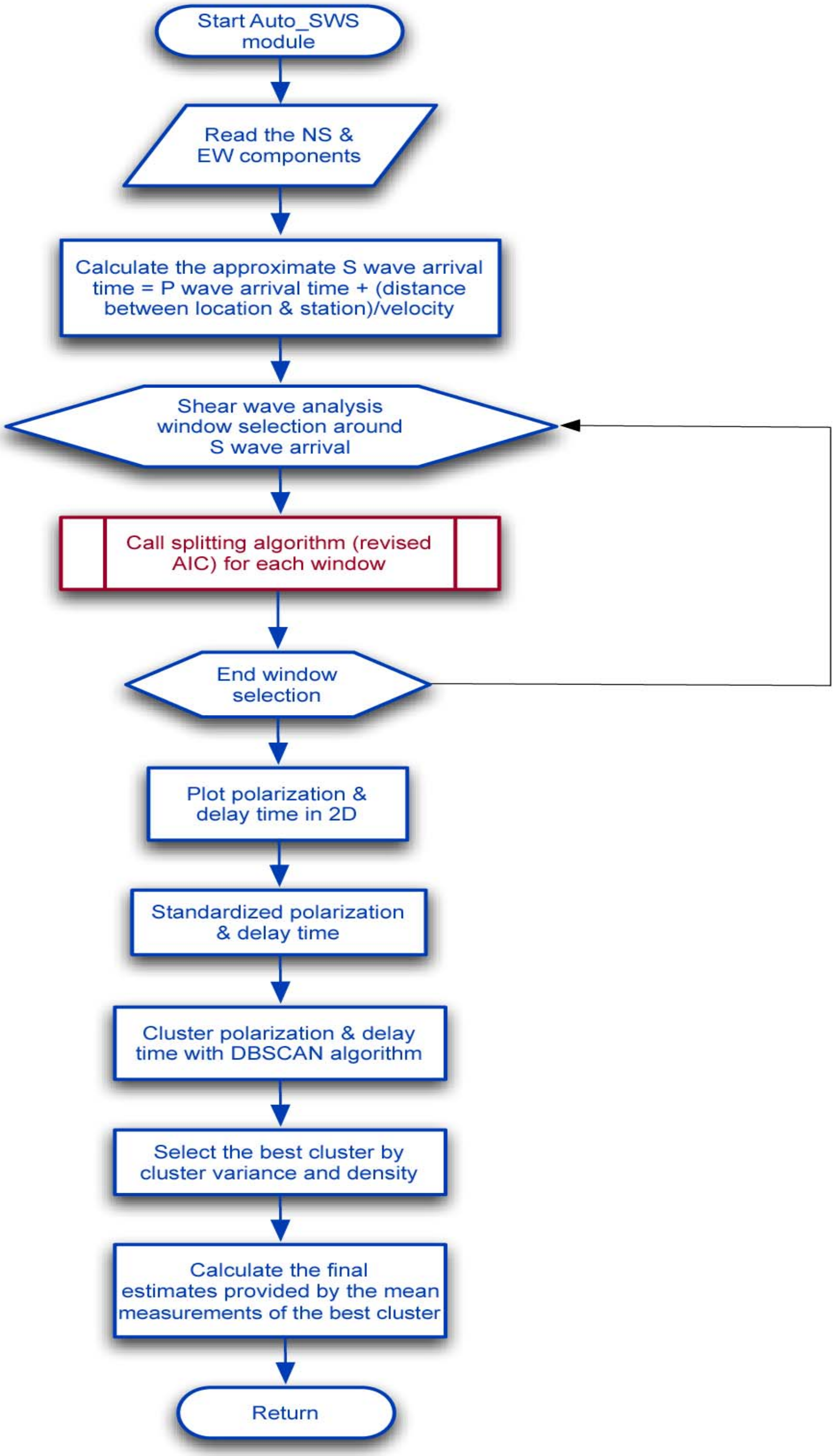

Figure 5.12. Flow chart of the Auto_SWS module.

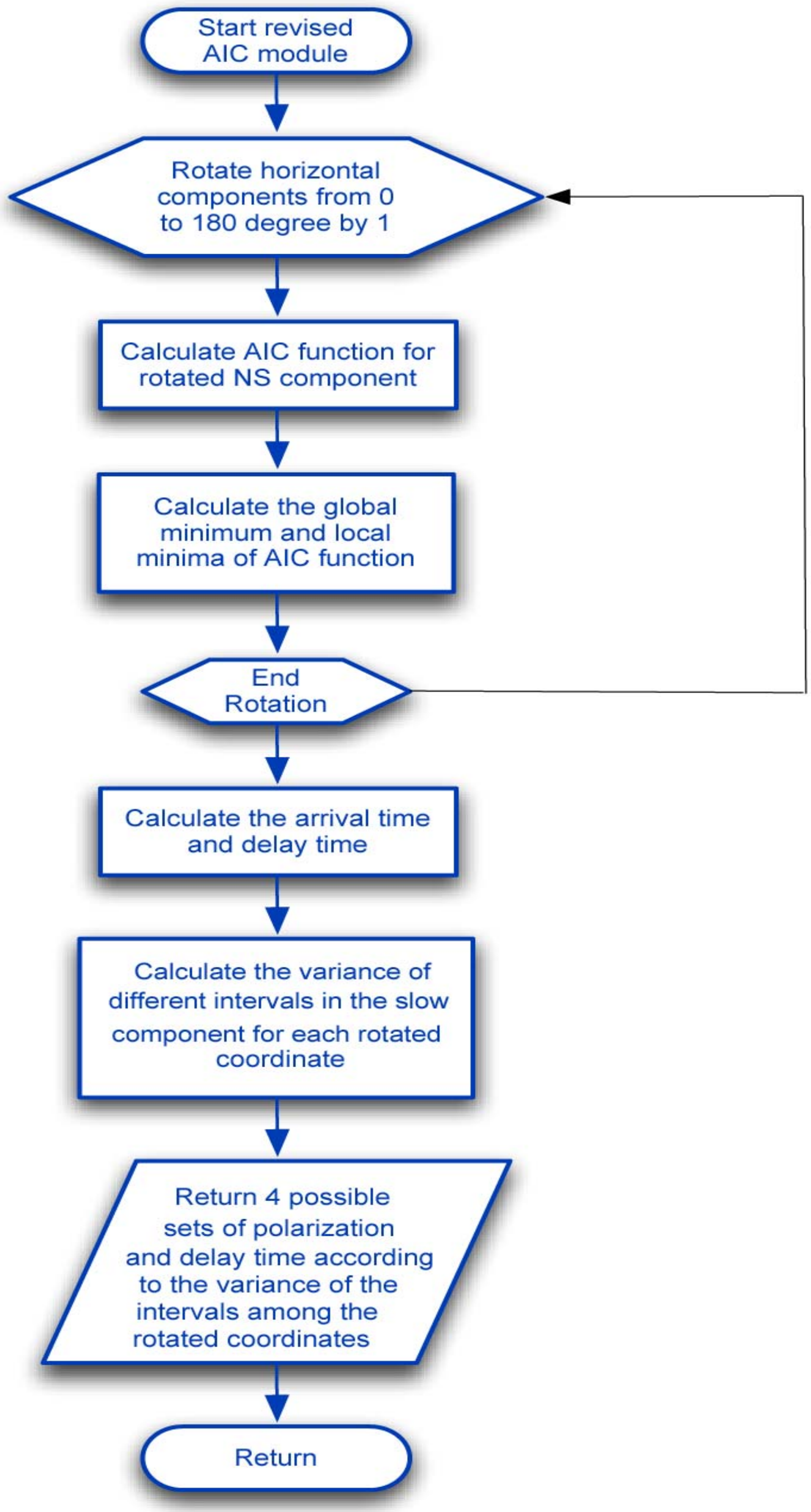

Figure 5.13. Flow chart of the revised AIC subroutine.

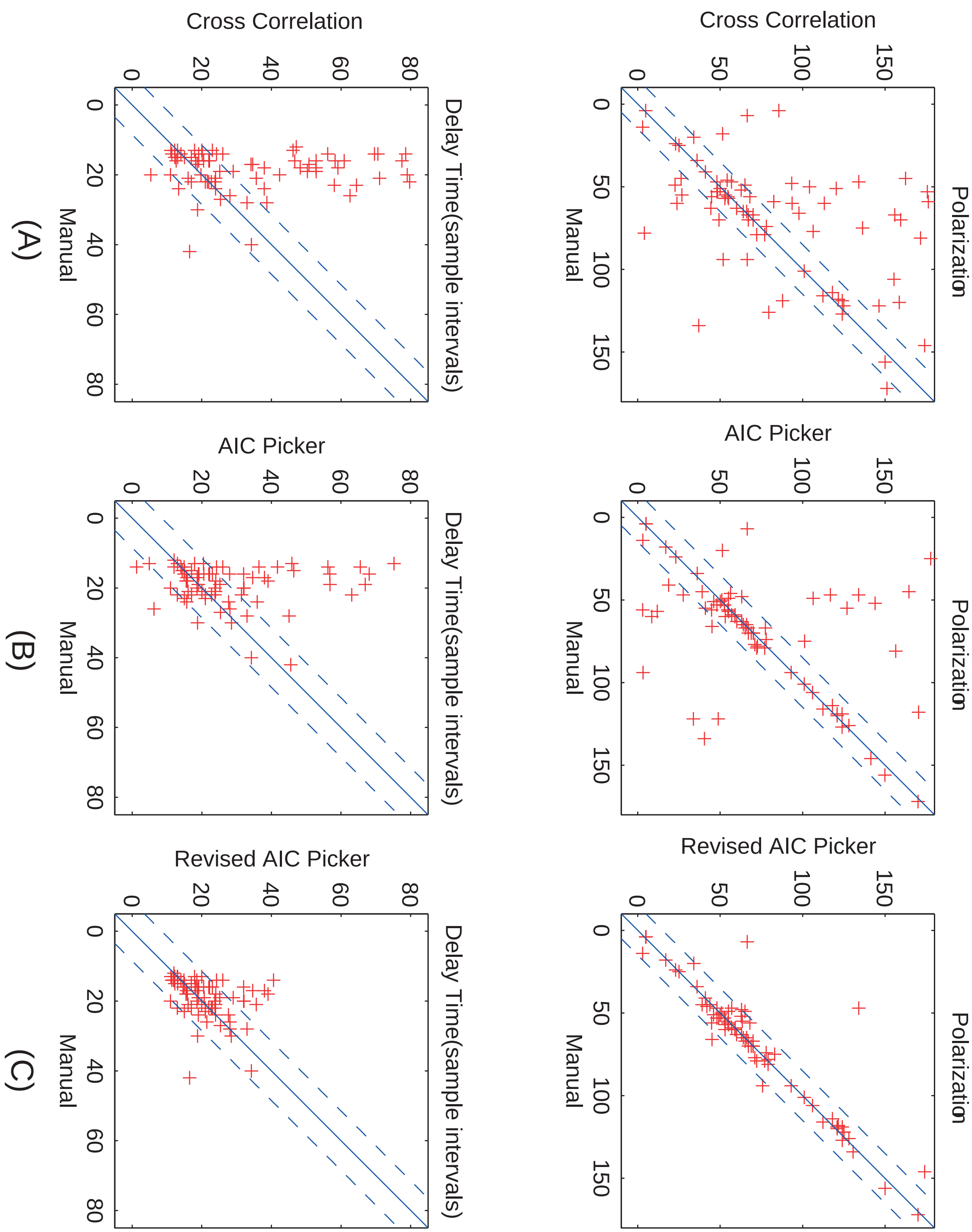

Cross Correlation
AIC Picker
Revised AIC Picker
Polarization
Delay Time(sample intervals)
Manual
(A)
(B)
(C)

Figure 5.14.

Figure 5.14. Comparison of the results between the manual measurements and the results calculated by different automated methods. (A) Cross-correlation method for 80 examples of SWS seismograms. The horizontal axis represents the manual measurements and the vertical axis the CC results. If the manual result equals the CC result, the plus symbol should be located right on the diagonal solid line. The dashed lines denote the acceptable error tolerance which is set as 15 degrees and 8 sample intervals for polarization and delay time, respectively. (B) is the same as in (A), except that the vertical axis represents the values obtained from the AIC Picker. And in (C) the vertical axis represents the estimates obtained from the Revised AIC Picker, in which 76/80 of polarizations and 70/80 of delay times are located inside the error tolerance.

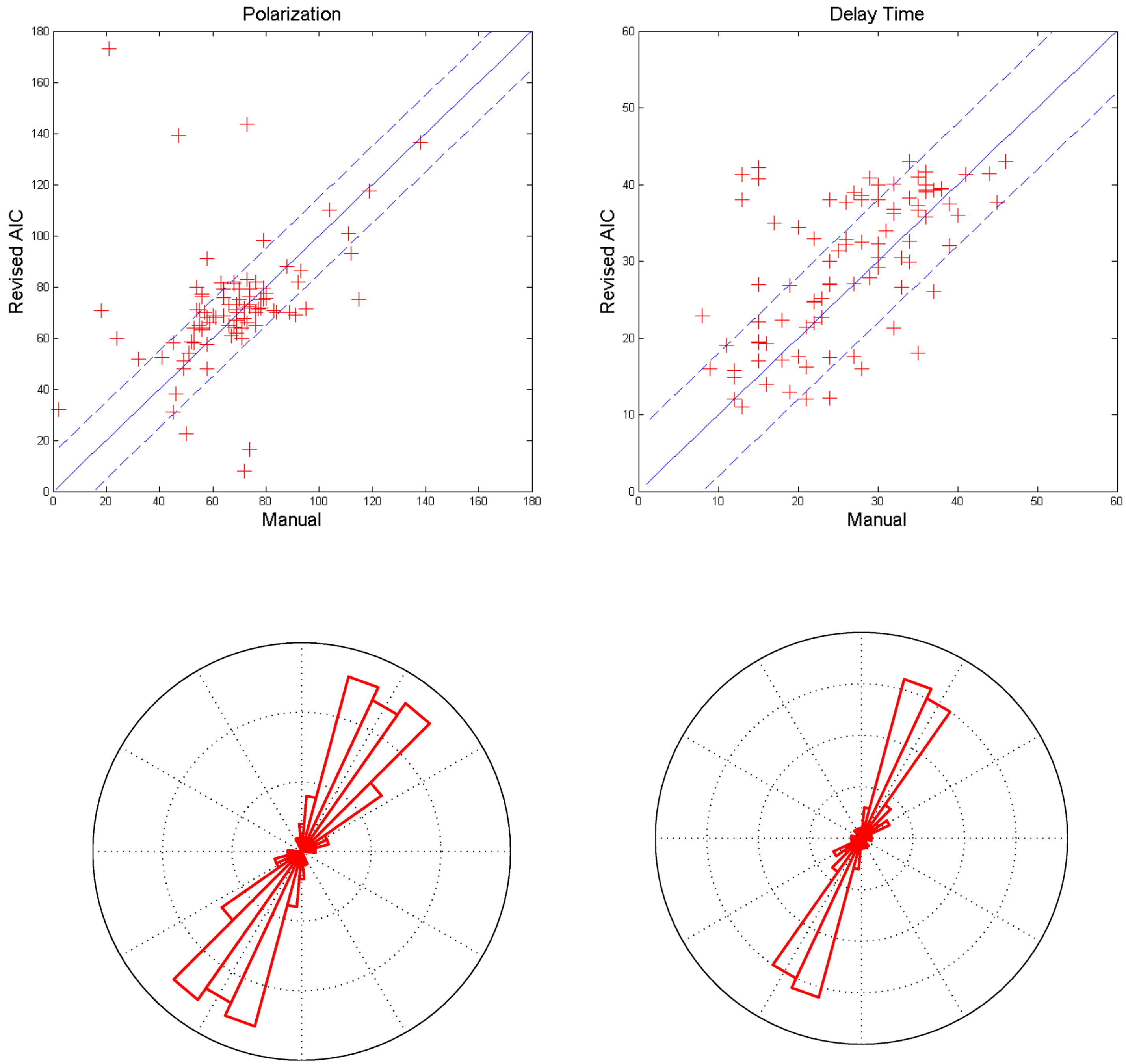
Polarization
Revised AIC
Manual
Delay Time
Revised AIC
Manual

Figure 5.15.

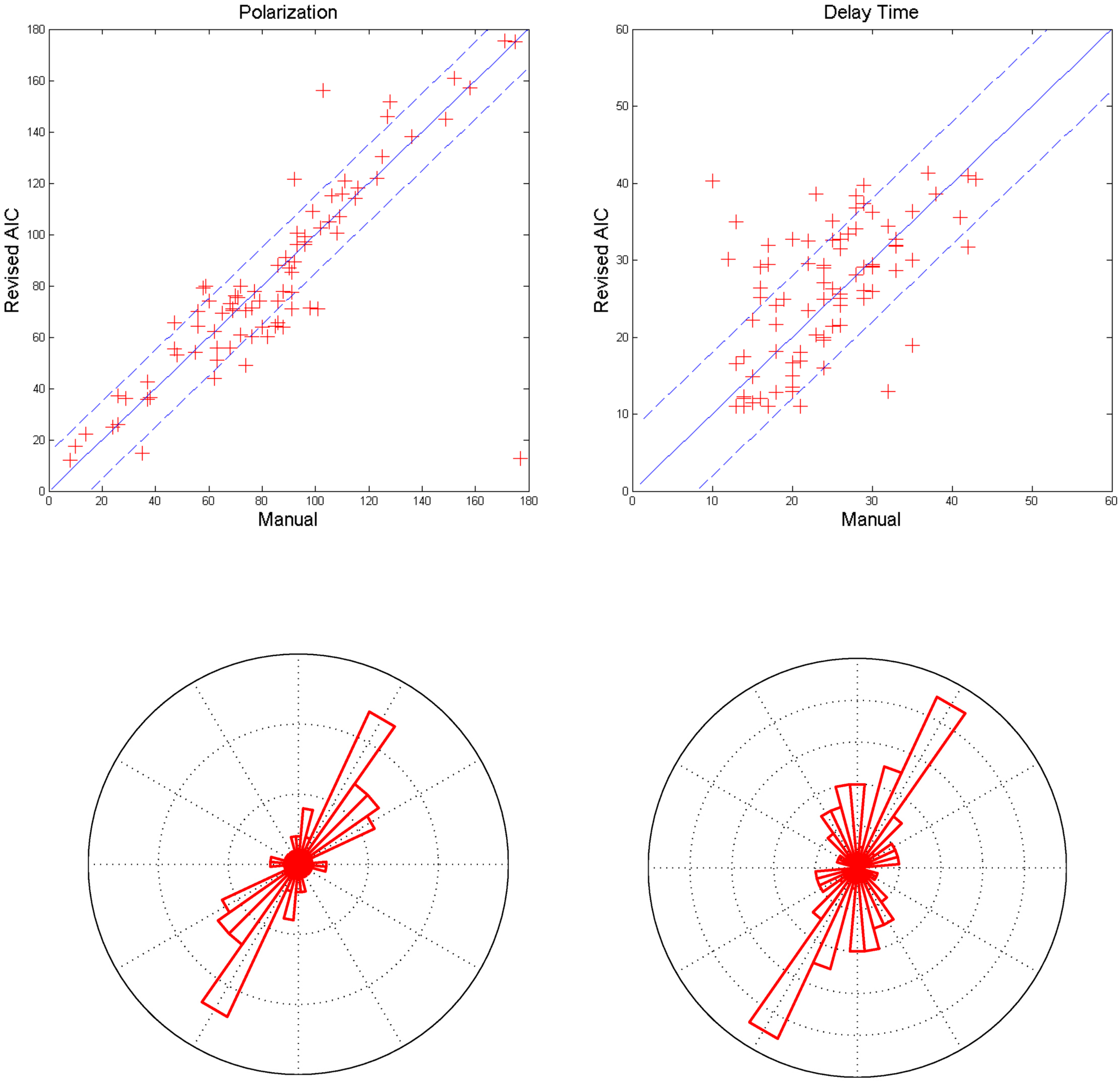
Polarization
Revised AIC
Manual
0
20
40
60
80
100
120
140
160
180
Delay Time
Revised AIC
Manual
0
10
20
30
40
50
60

Figure 5.16.

Figure 5.15. Comparison between shear-wave splitting parameters measured by manual and automatic methods respectively. Shown in this figure are comparisons for station H71 where a total of 89 shear wave splitting events are well detected and measured. For polarization there are 23 data points lying outside of the tolerance (indicated by dashed line) which is ±15 degrees, and for delay time there are 24 outliers away from the ±8 sample point tolerance. Thus the percentage of data points inside the acceptable error tolerance is 74% and 73% for polarization and delay time respectively. Shown in the lower panel is the comparison between rose diagrams of manually measured polarizations (left) and of automatically computed results (right).

Figure 5.16. The same comparison plots as in Figure 15 for station H75. 19 out of totally 84 data points are located outside of tolerance for polarization measurements, therefore the percentage of satisfying results is 77%. For delay time, with 20 data points lying outside of the tolerance this percentage is 76%. Note that the red cross far in the right lower corner of polarization plot is also within the ±15 degree tolerance.

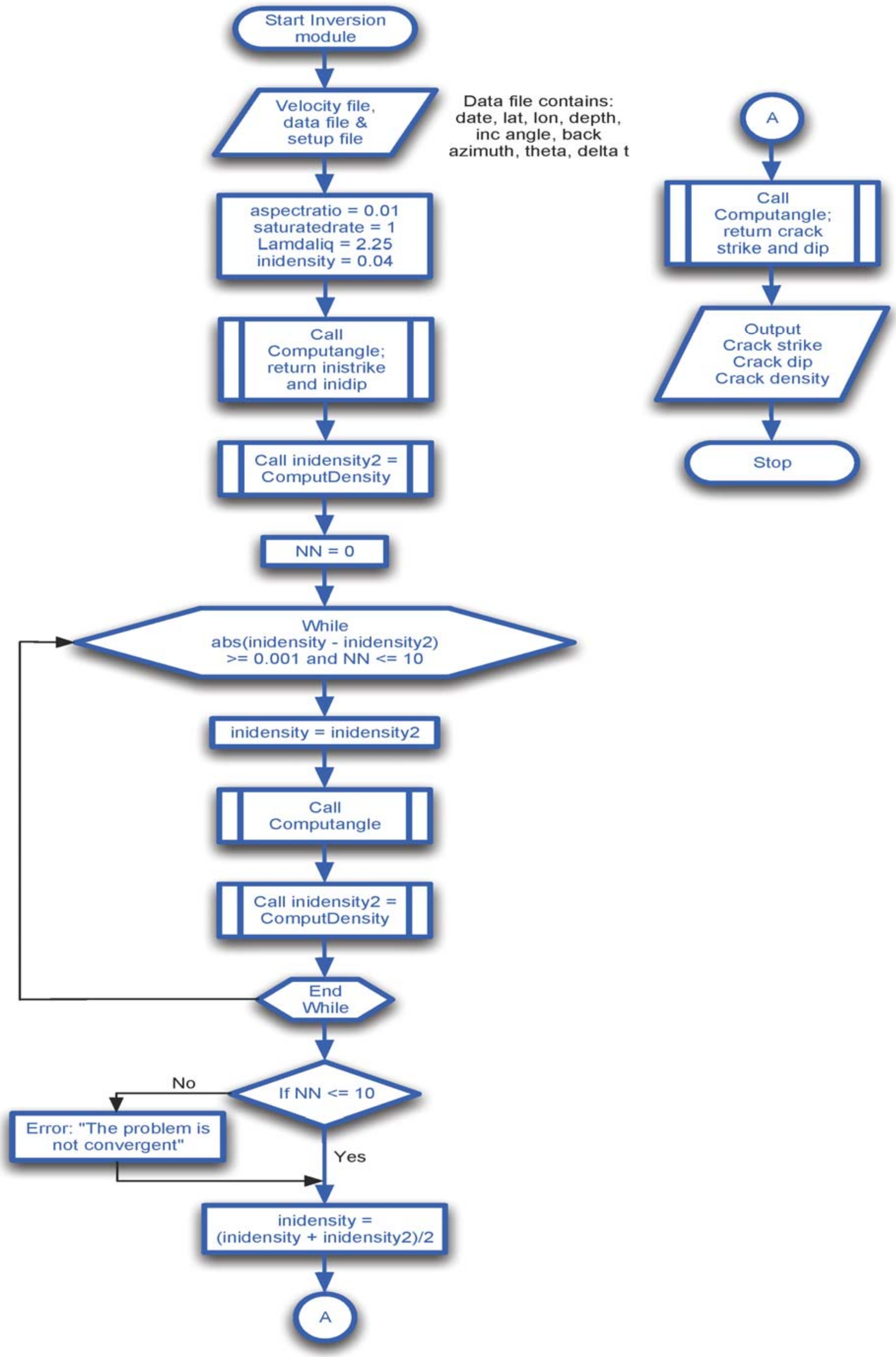

Figure 5.17. Flowchart of the INVERSION module.

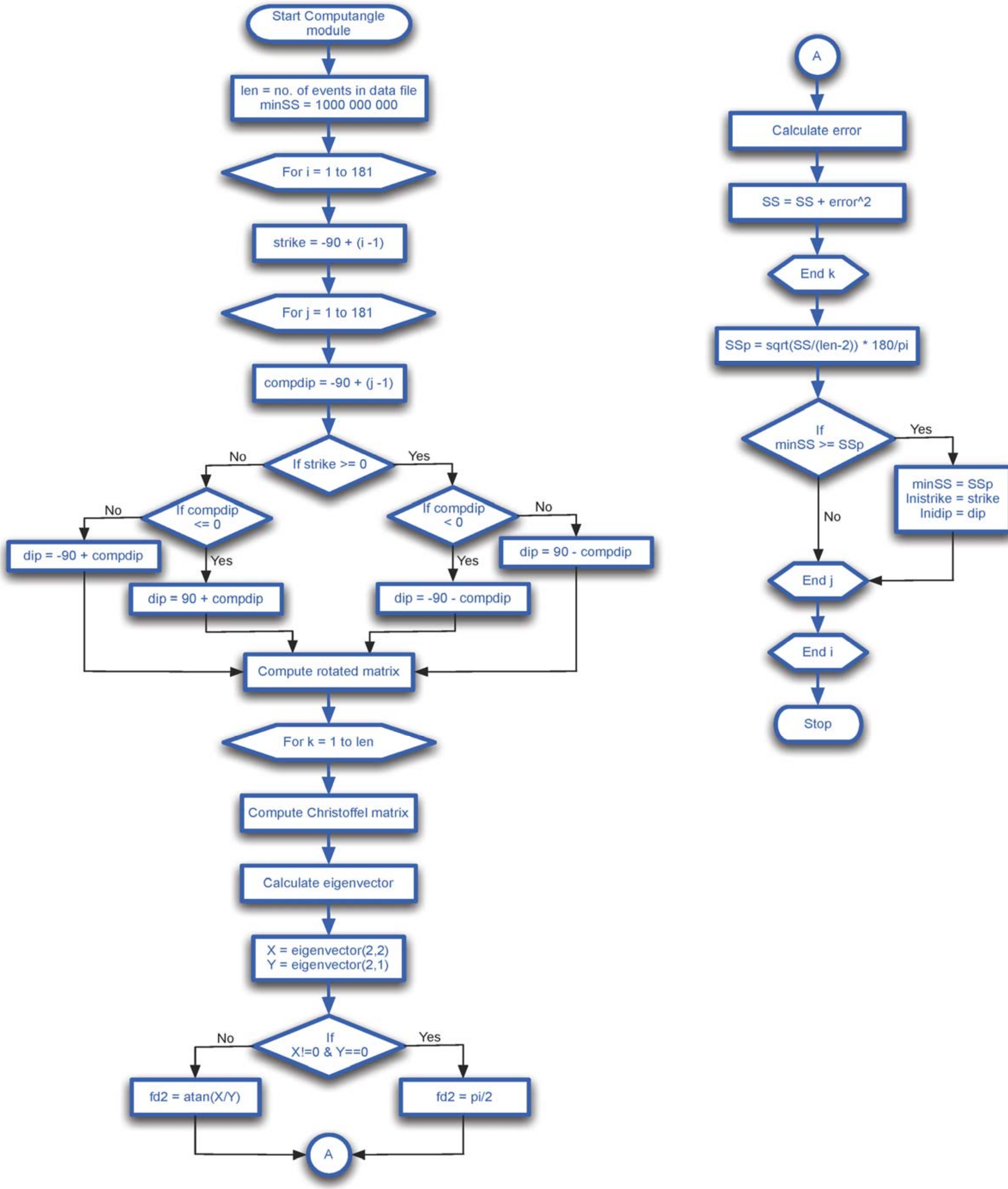

Figure 5.18. Flowchart of the Computangle subroutine.

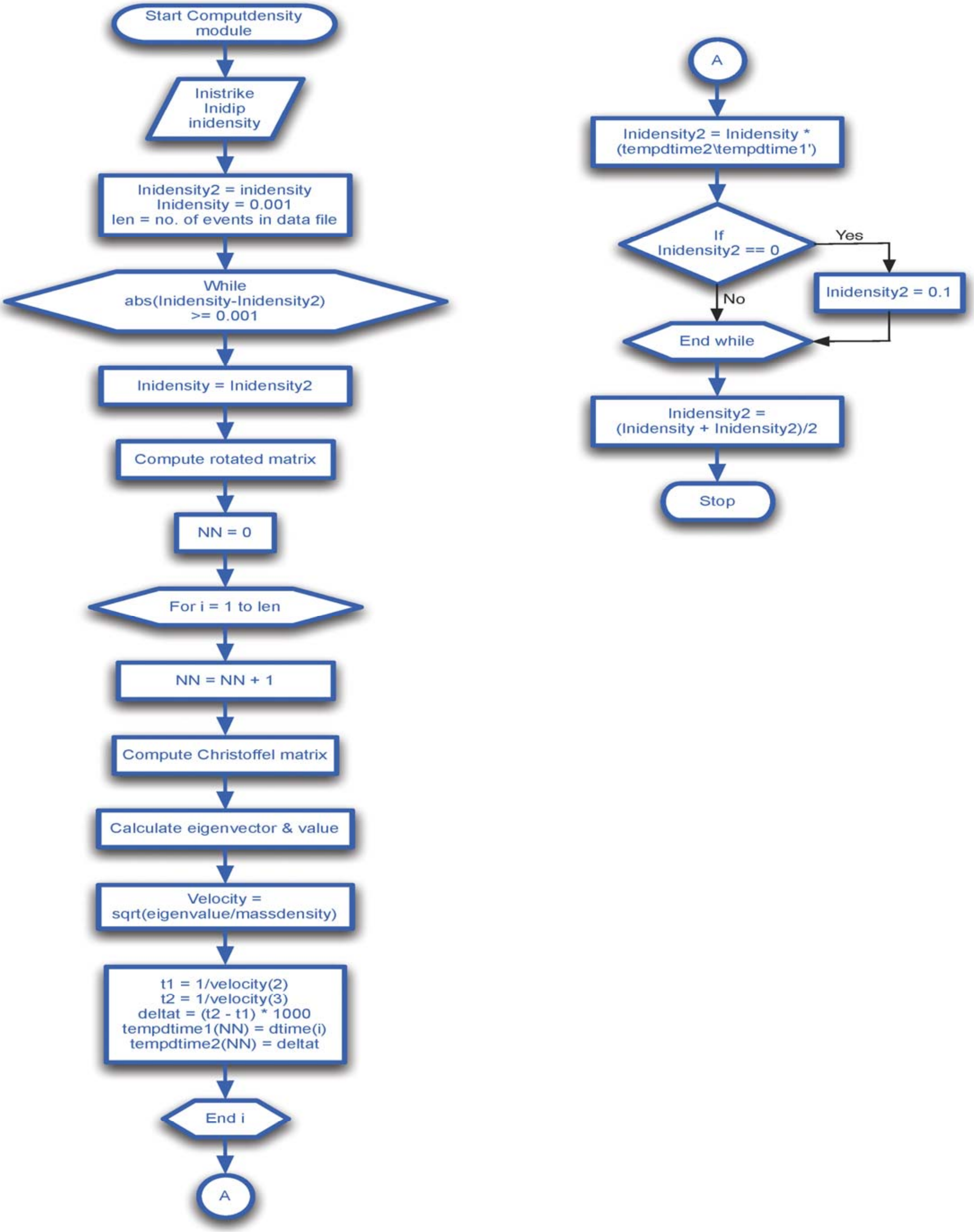

Figure 5.19. Flowchart of the Computdensity subroutine.

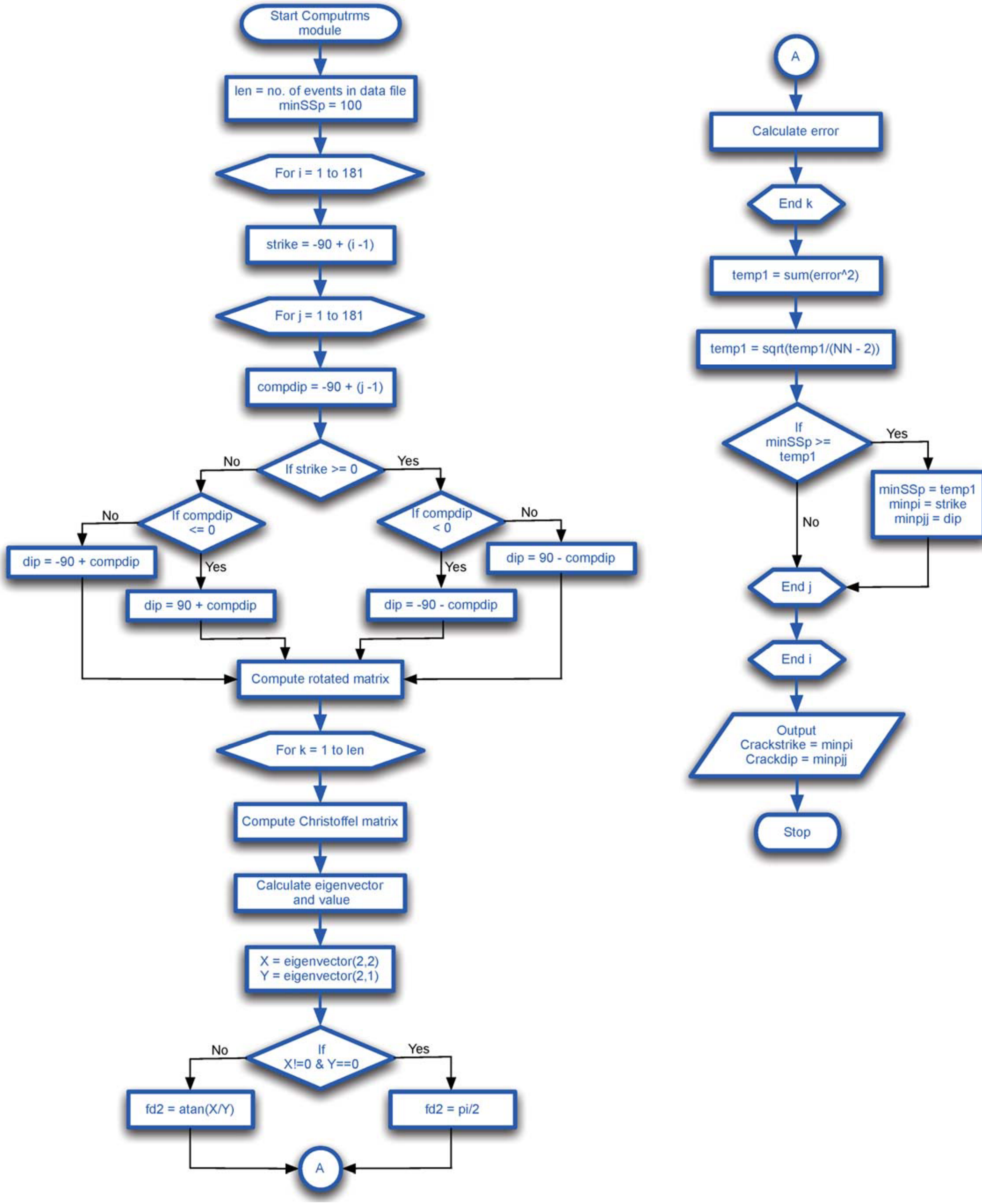

Figure 5.20. Flowchart of the Computrms subroutine.